Spring 5-7-2022

Macromolecular Fluorescent Conjugates for Bioimaging Applications

Paul Lovell
University of Nebraska Medical Center

MACROMOLECULAR FLUORESCENT CONJUGATES FOR BIOIMAGING APPLICATIONS

by

Paul Lovell

A DISSERTATION

Presented to the Faculty of
the University of Nebraska Graduate College
in Partial Fulfillment of the Requirements
for the Degree of Doctor of Philosophy

Pharmaceutical Sciences Graduate Program

Under the Supervision of Professor Aaron M. Mohs

University of Nebraska Medical Center
Omaha, Nebraska

May 2022

Supervisory Committee

Heather Jensen-Smith, PhD. Martin Conda-Sheridan, PhD.

Corey Hopkins, PhD.

Acknowledgements

Firstly, I would like to thank Dr. Aaron Mohs for the opportunity to discover and learn on two different projects, expanding my research abilities over the last five years. The techniques and skills I have been able to add to my arsenal has benefited me in the scientist I have become. His leadership to push me out of my comfort zone has enabled me to think more critically.

I would like to thank all of my committee members, Dr. Heather Jensen-Smith, Dr. Corey Hopkins, and Dr. Conda-Sheridan for all of their support and advice over the last five years. Their questions have enabled me to think critically on my research.

All of the animal training could not have been done without the guidance of Dr. Joshua Souchek, Dr. Bowen Qi, Dr. Nick Wojtynek, and Dr. Madeline Olson. All of their expertise enabled me to learn the various animal techniques.

I am also grateful to Constance McKee, Dr. Stephen Kahl, and Dr. Michael Olive for of all their expertise, advice, and providing the nerve imaging contrast agent for the nerve imaging project. It was an honor to work alongside a company and learn how a company operates in the healthcare industry. Thanks also to Dr. Jieyu Zhou of Abzena Pharmaceuticals (Bristol, PA) for conjugation of the Nervelight™ agent, Dr. Pamela Lein and lab at the University of California at Davis (Davis, CA) for neuronal survival bioassays, and Kristen Leland of the University of Nebraska Medical Center Office of Comparative Medicine for assistance and expertise with animal training, surgeries, and protocol questions.

I would also like to sincerely thank Dr. Denis Svechkarev for his expertise and help in many various realms. His expertise and advice were beneficial on the many chemistry questions and reviewing the data for both of my projects, especially in the fluorescent nanoparticle project. Denis has become a friend that I have had the pleasure to getting to know over the last 5 years and someone I have been able to look up to.

I am also grateful to Lucas Houser for all of his help with animal experiments, data collection, data interpretation, and advice on the nerve imaging project. His help enabled me to have a second pair of hands during animal surgeries. Thank you also to Dr. Aishwarya Bapat for her help in data collection and interpretation in both projects. She also became a close friend over the past five years. Thanks to Dr. Svetlana Romanova for all of her help in synthesizing the silica nanoparticles and her expertise and advice in silica chemistry. I also wish to thank Dr. Jensen-Smith for her expertise and advice regarding cell studies.

I would like to thank all of the current and past Mohs lab members for creating an awesome and close-knit working environment. It has been a pleasure to get to know everyone over the past 5 years. Everyone has provided a large amount of support, encouragement, and friendship.

Lastly, I am grateful to my family, who, has been through it all with me. They have been there encouraging me, supporting me, and providing me with so much helpful advice during the roller coaster ride of graduate school.

MACROMOLECULAR FLUORESCENT CONJUGATES FOR BIOIMAGING APPLICATIONS

Paul Lovell, Ph.D.

University of Nebraska, 2022

Supervisor: Aaron M. Mohs, Ph.D.

Bioimaging tools enable the visualization of small anatomical features as well as structures that may be obscured by other tissue. One such group of tools are fluorescent probes, molecules that emit detectable signals when stimulated by an excitation source. Incorporating fluorescent conjugates for clinical purposes would enable direct usage for the diagnosis, detection, or treatment of diseases. The development of specific targeting agents is feasible due to the number of nanomaterials and biological products that contain fluorophores. Specific targeting agents can target a particular region of interest, such as a cancerous tumor for removal or vital nerve structure for avoidance during image-guided surgery.

As a result, fluorescent guided surgery (FGS) allows a surgeon to remove or avoid specific areas during surgical interventions without damaging surrounding tissue or structures. Many different biomaterials, each with unique and useful properties, can be utilized as a platform for fluorescent contrast agent design, such as avoiding vital anatomical structures. During surgical intervention, the location of nerves is of high concern for surgeons, as damaging those structures can result in severe consequences for the patient. Herein, the fluorescent contrast agent Nervelight™, consisting of a near-infrared (NIR) fluorescent dye attached to the naturally occurring protein, nerve growth factor, can be utilized for nerve targeting and visualization. Nerves are at high risk for damage during surgery; avoidance of these areas is critical to preserving nerve function.

Nanomaterials can also be used as platforms for NIR dyes to target ligands bound at the cell surface providing tissue specificity. In this study, carbon or silica-based nanomaterials were used as a scaffold for imaging a CD44+ cancer cell line. A targeted fluorescent nanomaterial design may provide specific targeting to CD44+ cancerous tumors for surgical removal via hyaluronic acid, a known CD44 targeting ligand, and the NIR fluorophore sulfo-Cy5 dye. Fluorescent contrast agents can be useful in labeling an area for avoidance or surgical removal in bioimaging applications.

TABLE OF CONTENTS

LIST OF FIGURES

LIST OF TABLES

LIST OF ABBREVIATIONS

5-ALA	5-aminominolevulinin acid
ACQ	aggregation-caused quenching
AIE	aggregation induced emission
AFM	atomic force microscopy
APTES	3-aminopropyltriethoxysilane
BBB	blood brain barrier
BDNF	brain derived neurotrophin factor
CNS	central nervous system
CTCF	corrected total cell fluorescence
sCy5	sulfo-Cy5 amine dye
Cy5-SiNP	Cy5 dye incorporated non-coated silica nanoparticle
Cy5-SiNP-HA	Cy5 dye incorporated hyaluronic acid coated silica nanoparticle
DMSO	dimethyl sulfoxide
FGS	fluorescent guided surgery
HA	hyaluronic acid
HEPES buffer	(N-(2-Hydroxyethyl) piperazine-N′-(2-ethane sulfonic acid), 4-(2-Hydroxyethyl) piperazine-1-ethane sulfonic acid)
IACUC	institutional animal care and use committee
ICG	indocyanine green

IHC	immunohistochemistry
LYVE-1:	lymphatic vessel endothelial hyaluronan receptor 1
MWCO	molecular weight cutoff
MRI	magnetic resonance imaging
NGF	nerve growth factor
NHS	*N*-hydroxysuccinimide
NIR	near-infrared
NT-3	neurotrophin-3
PBS	phosphate buffered saline
PNS	peripheral nervous system
SBR	signal to background (muscle) ratio
SiNP	unlabeled silica nanoparticle
SiNP-Cy5-L	surface-grafted Cy5 dye (low) silica nanoparticle
SiNP-Cy5-M	surface-grafted Cy5 dye (medium) silica nanoparticle
SiNP-Cy5-H	surface-grafted Cy5 dye (high) silica nanoparticle
SiNP-HA	unlabeled, hyaluronic acid coated silica nanoparticle
SNR	signal to noise ratio
TEOS	tetraethyl orthosilicate
TBS	tri buffered saline
TBST	tri buffered saline with tween

TrkA	tropomyosin-receptor kinase A
TrkB	tropomyosin-receptor kinase B
TrkC	tropomyosin-receptor kinase C
TSPA	3-triethoxysiylpropyl succinic anhydride
XPS	x-ray photoelectron spectroscopy

CHAPTER 1: OVERALL INTRODUCTION

The field of theranostics and bioimaging techniques have emerged as vital tools for a variety of applications in the clinic. Bioimaging can be defined as a method used to non-invasively visualize biological processes[1]. The ability to detect changes in anatomical structures, disease detection, and tracking fluorescent probes are a few of the many achievements bioimaging can provide. Bioimaging is important in the clinic for detecting disease or changes within cells or organs[2]. These various bioimaging applications can enhance and improve the monitoring of diseases and patients in the clinic. Visualizing cellular structures provides a significant benefit to medical personnel by helping them to distinguish between healthy and cancerous tissue in a patient. During surgery, it becomes essential to identify vital anatomical structures, such as nerves and blood vessels, to avoid potential damage. Evaluating cellular structures or organ systems, bioimaging has the potential to show injury or damage to these different structures[3, 4]. Bioimaging can monitor the cell-surface interactions in regenerative medicine and track cellular responses to damage. Tracking of damage caused by neurodegenerative diseases, bioimaging has the potential to visualize the damaged cells and the response that occurs[5]. These are only a few areas in which bioimaging has emerged as a potential tool for use in the clinic.

Fluorescent probes play a significant role in bioimaging applications and have emerged to advance the field of theranostics within the clinic. Currently, magnetic resonance imaging (MRI), ultrasound, and radioisotope labeling are used in the clinic to visualize physiological changes in the body. Fluorescent bioimaging is highly sensitive, less invasive than traditional visualization methods, and enables safe detection[6]. These advantages of fluorescent bioimaging would provide enhanced visualization of the pathological and pathophysiological changes within the body or cells in real-time. These benefits are most apparent during surgical procedures. The use of near-infrared (NIR) dyes and associated instrumentation allows integration of the visible surgical field

with the NIR image, allowing a surgeon to visualize the fluorescent location overlayed with the visible natural anatomy. Combining the surgical and NIR fields enables the non-targeted anatomical regions to as references for the targeted and labeled regions. Imaging in real-time allows for intraoperative guidance that can be used for various applications, such as the delineation of tumors. Bioimaging techniques with fluorescent probes have shown to be promising modalities for monitoring various biological processes[7-9]. The utilization of NIR probes enable improvements to provide targeting to a region of interest. Ultimately, bioimaging applications can visualize these specific regions of interest, especially in the surgical field, to avoid vital anatomical structures or remove a tumor.

Fluorescent Guided Surgery (FGS) offers great potential in theranostics and optical imaging to improve surgical outcomes by enabling enhanced visualization of tissue and effects of disease real-time. NIR fluorescence imaging in the emission spectrum of 700-900 nm can provide surgeons with advantages of low scattering, low tissue autofluorescence, and high signal to background ratios[10-12]. These advantages are beneficial for oncological surgeries to delineate cancerous tissue to be surgically removed while highlighting vital structures in the surgical area to be avoided. Current imaging modalities such as ultrasound and MRI can be helpful in imaging where a cancerous tumor is located around other major tissue, but fluorescent probes during surgery can allow surgeons to visualize tumors or vital structures in real-time, reducing the potential of post-surgical consequences. NIR fluorescent probes can be designed and developed to target specific diseases and further enhance these current imaging modalities.

Each bioimaging application includes a fluorescent probe modified to target a specific region of interest. In this project, two main directions were evaluated, each with a different fluorescent probe and a different region of interest. The first project was an evaluation of a nerve-specific contrast agent to label at-risk nerve sites intraoperatively to preserve nerve function. Avoiding vital anatomical structures during surgery is crucial to prevent damage to those nerve,

therefore avoiding any negative effects on a patient's quality of life. Proteins found predominately on nerves were utilized as a platform for a nerve-specific fluorescent probe. In the second project, a silica-based fluorescent nanoparticle was synthesized to target CD44+ cancer cells for use in tumor removal. Silica nanoparticles are largely considered non-toxic, biocompatible, and have surfaces that can be easily modified with various biomolecules, ligands, or proteins. Common biomolecules, such as hyaluronic acid or folic acid, can be attached to the nanoparticle's surface for specific targeting to cell surface receptors. Many cancer types have an upregulation of various cell receptors that can be exploited for specific targeting.

Both projects are dependent on the intended application for incorporation in the clinic. The intended application determines the best route of administration, of which there are two: local and systemic. The local route of administration is administering the contrast agent at the target site during the surgery. Visualizing nerve structures in a specific region would be best through the local administration route, ensuring the contrast agent reaches the target site. Since nerves are present throughout the body, the agent may not reach the intended surgical location site through the systemic administration. An additional advantage of the local administration route is that a surgeon can reapply the contrast agent to an area during the surgery. The systemic route of administration is administrating the contrast agent at a location away from the target site, usually through circulation in the bloodstream which will eventually bring the contrast agent to the intended target location. Systemic administration would allow a tumor to be visualized and result in accumulation of the contrast agent at the tumor site. Intravenous administration can potentially enable the fluorescent probe to be more efficiently delivered to the target site since tumors proliferate near vasculature allowing for binding to the cancerous tissue. For implementation in the clinic, systemically injecting a fluorescent probe with specific targeting capabilities would allow for visualization of the tumor during the surgery. As the goal of cancer surgery is the removal of the tumor, systemic administration may be the better choice of

administration as the fluorescent probes could accumulate on the entire tumor, thereby identifying the extent of the cancerous tissue. Ultimately, bioimaging with fluorescent probes is characterized by numerous exciting applications for use in the clinic including nerve imaging and tumor delineation, which can both benefit from advancements in visualization of biological processes.

Bibliography

1. Pavlovic, M., Fundamentals of Bioimaging. In *Bioengineering*, Springer: **2015**; pp 217-228.

2. European Institute for Biomedical Imaging, R., Strategic Research Agenda for Biomedical Imaging. *Insights Imaging.* **2019**, *10* (1), 7.

3. González-Béjar, M.; Francés-Soriano, L.; Pérez-Prieto, J., Upconversion Nanoparticles for Bioimaging and Regenerative Medicine. *Front. Bioeng. Biotechnol.* **2016**, *4*, 47.

4. Mitragotri, S.; Anderson, D. G.; Chen, X., et al., Accelerating the Translation of Nanomaterials in Biomedicine. *ACS nano.* **2015**, *9* (7), 6644-6654.

5. Zhou, J.; Jangili, P.; Son, S., et al., Fluorescent Diagnostic Probes in Neurodegenerative Diseases. *Adv. Mater.* **2020**, *32* (51), 2001945.

6. Nagano, T., Development of Fluorescent Probes for Bioimaging Applications. *Proc. Jpn Acd. Ser. B Phys. Biol. Sci.* **2010**, *86* (8), 837-847.

7. Guo, Z.; Park, S.; Yoon, J., et al., Recent Progress in the Development of Near-Infrared Fluorescent Probes for Bioimaging Applications. *Chem. Soc. Rev.* **2014**, *43* (1), 16-29.

8. Kiyose, K.; Kojima, H.; Nagano, T., Functional Near-Infrared Fluorescent Probes. *Chem. Asian J.* **2008**, *3* (3), 506-515.

9. Qian, G.; Wang, Z. Y., Near-Infrared Organic Compounds and Emerging Applications. *Chem. Asian J.* **2010**, *5* (5), 1006-1029.

10. Gioux, S.; Choi, H. S.; Frangioni, J. V., Image-Guided Surgery Using Invisible Near-Infrared Light: Fundamentals of Clinical Translation. *Mol. Imaging.* **2010**, *9* (5), 7290.2010. 00034.

11. Chance, B., Near-Infrared Images Using Continuous, Phase-Modulated, and Pulsed Light with Quantitation of Blood and Blood Oxygenation A. *Ann. N. Y. Acad. Sci.* **1998**, *838* (1), 29-45.

12. Gibbs, S. L., Near Infrared Fluorescence for Image-Guided Surgery. *Quant. Imaging Med.. Surg.* **2012**, *2* (3), 177.

CHAPTER 2: NERVE IMAGING INTRODUCTION

The nervous system is a complex part of the human body that coordinates communication, movement, control, and regulatory actions within the body. The system encodes cues from the surrounding environment to produce signals sent throughout the body, allowing organisms to interact with their surroundings[13]. Cues from the surrounding environment induce a fast response to many different signals and stresses. These controls enable the sensory components to detect and receive environmental cues, leading to the processing and transmission of the signals to the motor components, which are necessary to provide a proper body response. Organisms can distinguish between hot or cold and pain or non-pain to specific signals or stimuli based upon the complexity of the environmental cue. This system is an informational processing system encompassing both internal and external sources, with transmission through signal patterns along specific pathways[14]. The ability for signals to be continuously transported through the body is provided by highly specialized types of cells.

The function of the nervous system includes retrieval of surrounding information, processing or transmitting a cue, and response production, which are all completed by the vast networks of nerves throughout the body. Nerve cells found throughout the nervous system share three components: the soma, the axon, and dendrites[14]. Since these cells transmit information between one another, the vast network of nerve cells is formed throughout the entire body, allowing for the communication and control to be governed by these specific cells. One example of how nerves transmit information is through the axon of one nerve cell to the dendrite of a neighboring nerve cell via the synapse between the two cells[14]. These synapses and affiliated exchanging of information between neurons are crucial for everyday tasks to occur and allow for the coordination of movement, control, and regulatory responses. Damage or injury to nerves can significantly impact how the neurons behave and potentially halt or alter the transmission of information between nerve cells, leading to the loss of motor or sensory function[15]. Injury or

damage to a nerve site can inhibit the proper function of the nerve, resulting in the loss of signal transmission can lead to lasting consequences to an individual. Nerve detection as an aid for surgeons during surgical intervention is critical to help reduce accidental nerve damage.

Many surgeries commonly use electrophysiologic monitoring or neuromonitoring to assess the functional integrity of nerves at a specific surgical site[16-25]. This neuromonitoring system is beneficial during surgery for locating nerve presence in specific areas by triggering a nerve impulse. There are different methods and techniques for neuromonitoring that are commonly used in surgeries, such as electroencephalography[18, 26], electromyography[18, 24-31], and evoked potentials[18, 22, 25, 26, 28]. Typically, these monitoring techniques are selected by the surgeon with specialized monitoring staff to provide an alert when a nerve is present in the area[16]. The instrumentation and techniques available for surgeons through neuromonitoring can be beneficial for detecting changes in the electrophysiological signal of nerves (Figure 1). While the detection of changes in nerve signal is crucial, visualization details and location are not displayed with these techniques. There is a limited ability of visualization, but the electrode location can inform a surgeon that there is a nerve is in the area. [32, 33]. Multimodality neuromonitoring enables the combination of individual submodality strengths, including electromyography and evoked potentials, to detect nerve presence in a region of interest[27-30, 34, 35]. With the detection of both sensory and motor nerve impulses, surgeons will be alerted of nerve presence, decreasing the potential risk of nerve damage. Motor nerves function as effectors of information that are carried by neurons from the central nervous system to the peripheral tissues and organ systems, while sensory nerves function by transmitting impulses from sensory receptors in internal organs to the central nervous system and account for around 10 million nerves in the human body[36]. As the number of sensory nerves can be significantly greater than the number of motor nerves, neuromonitoring techniques are useful for nerve detection during surgery. The addition of imaging can provide an added visualization aspect. Nerve imaging during surgery would be a valuable method to detect both motor and sensory nerves present in an area of interest.

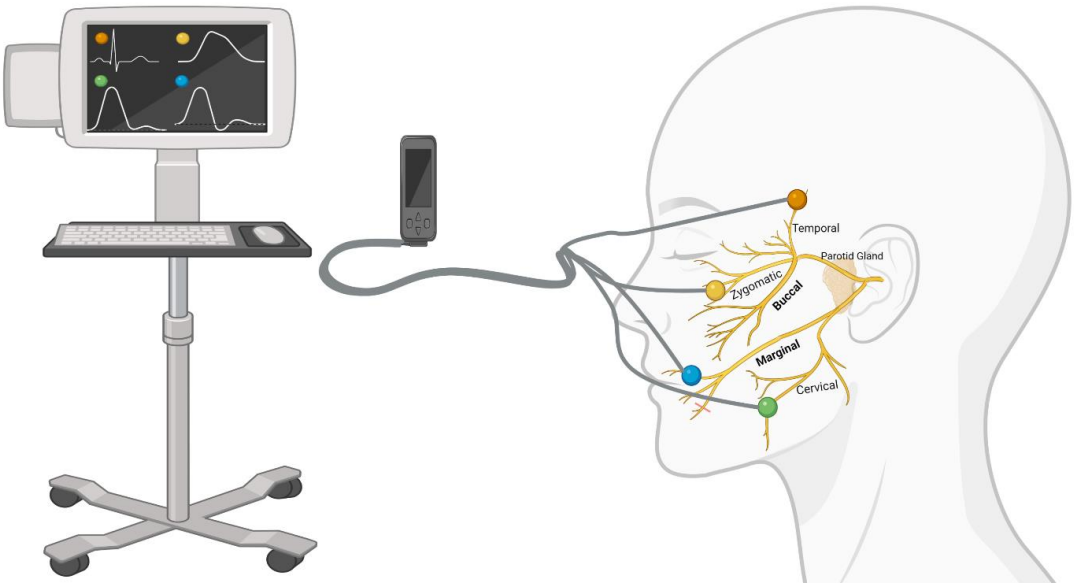

Figure 1. Neuromonitoring technniqe of nerve presence. Electrodes are placed in the region of interest to detect nerve impulses displayed on a monitor. Created using biorender.com.

As neuromonitoring methods and techniques do not provide a direct image of the surgery site, only providing nerve impulse detections in an area, nerve imaging can play a critical part in surgical intervention. Nerves are small structures, buried within different types of tissue, and have many extruding branches that can make surgical interventions difficult without compromising any nerve branches[12]. Imaging by an ultrasound modality in conjunction with electromyography has been used in peripheral nerve surgeries to visualize peripheral nerves prior to making an incision and allowing for preoperative visualization of a target site[37, 38]. Ultrasound and magnetic resonance imaging (MRI) are very common imaging modalities used in many clinical examinations and surgeries. Combining these modalities can help visualize peripheral nerves that can be difficult to locate only with neuromonitoring techniques[39-43]. The high resolution is essential to distinguish the complex architecture and functional profiles of nerves. However, clinical contrast agents targeting nerves specifically are not yet approved[44]. Furthermore, small nerves and branches still may not be completely identified using these different imaging modalities, leading to the risk of nerve damage. Enabling visualization of nerves during a surgical intervention potentially reduces accidental nerve damage.

Nerve damage resulting from surgical intervention is a negative outcome that can and should be prevented[45, 46]. Detrimental effects of nerve damage succumbed during surgery can have lasting effects for patients and could result in the loss of function of a specific movement or sensation. Many nerve sites are susceptible to surgical damage due to tissue innervation or anatomical nerve variability between patients leading to discrepancies in where a nerve is located[47, 48]. The mechanism of injury to a nerve during a surgical procedure may be attributed to different mechanical forces such as stretching, compression, contusions, or transections of a nerve[49]. Reduction of these mechanical forces on at-risk nerves during surgery would inevitably increase a patient's quality of life following surgery. Nerve damage presents a patient with undesirable impacts on daily life since nerves generate signals that govern both pain and motor function; the loss of function can greatly impair daily life activities[47, 50-58]. Reducing the risk of nerve damage during surgical intervention would allow for a patient's quality of life not to be affected by minimizing the loss of nerve function or associated pain. Pain in areas with high concentrations of nerves following surgery may lead to persistent pain. Persistent pain from a surgically induced neuropathic pain is estimated to be impact between 10-50% of patients, following common surgical operations[47, 59]. Neuropathies following surgeries can be attributed to the consequences of inflammation, stretching, transection, or contusion of a nerve resulting in loss of function or pain[47, 49]. Understanding the potential consequences of surgery and maximizing the surgeon's awareness to nerves in areas with high nerve presence is critical. Across various surgeries, the nerve damage was found in 20,000 to 600,000 patients in the United States, which resulted in post-surgical neuropathies and loss of nerve function[10, 60]. Although neuromonitoring and ultrasound or MRI imaging enable some nerves to be found during surgery, fluorescently labeling nerves during surgery would allow for an improvement of visualization of nerves.

Fluorescent-guided surgery (FGS) has continued to develop and emerge as a promising technology for use in the clinic by enabling enhanced visualization of specific anatomical structures intraoperatively. FGS can assist surgeons to distinguish between nerve presence, primary tumor tissue, and possible metastatic tumor tissue (Figure 2). A wide variety of contrast agents, probes, and targeting moieties are constantly being studied and developed for clinical effectiveness. A few of these dyes are FDA approved and commercially available for use in the clinic. Due to of their availability, these dyes are frequently investigated in FGS and include Methylene Blue[61-67], Indocyanine Green (ICG)[68-73], and 5-aminominolevulinin acid (5-ALA)[74-77], among others. Each of these dyes have their own properties while functioning in the near-infrared (NIR) window that allows for use in FGS. These dyes allow differentiation between tumor and healthy tissue types, enabling surgeons to distinguish between each type during surgery. The use of fluorescent dyes for targeting to specific tissue types can provide another surgical tool to aid surgeons during surgical intervention. The usage of the FGS technology intraoperatively during surgical intervention can be beneficial when used in conjunction with other technologies, such as ultrasound and MRI[39, 78-81]. The combined use of these modalities during a surgical procedure enhances the delineation of the tumor vs. healthy tissue or anatomical location of nerves and blood vessels when compared to the sole use of current modalities. Sensory nerves can be commonly missed by current technologies (ultrasound, MRI, and electromyography techniques), leading to the increased risk of nerve damage. Image-guided surgery can be a helpful technique during surgeries to prevent both nerve damage and removal of healthy tissue.

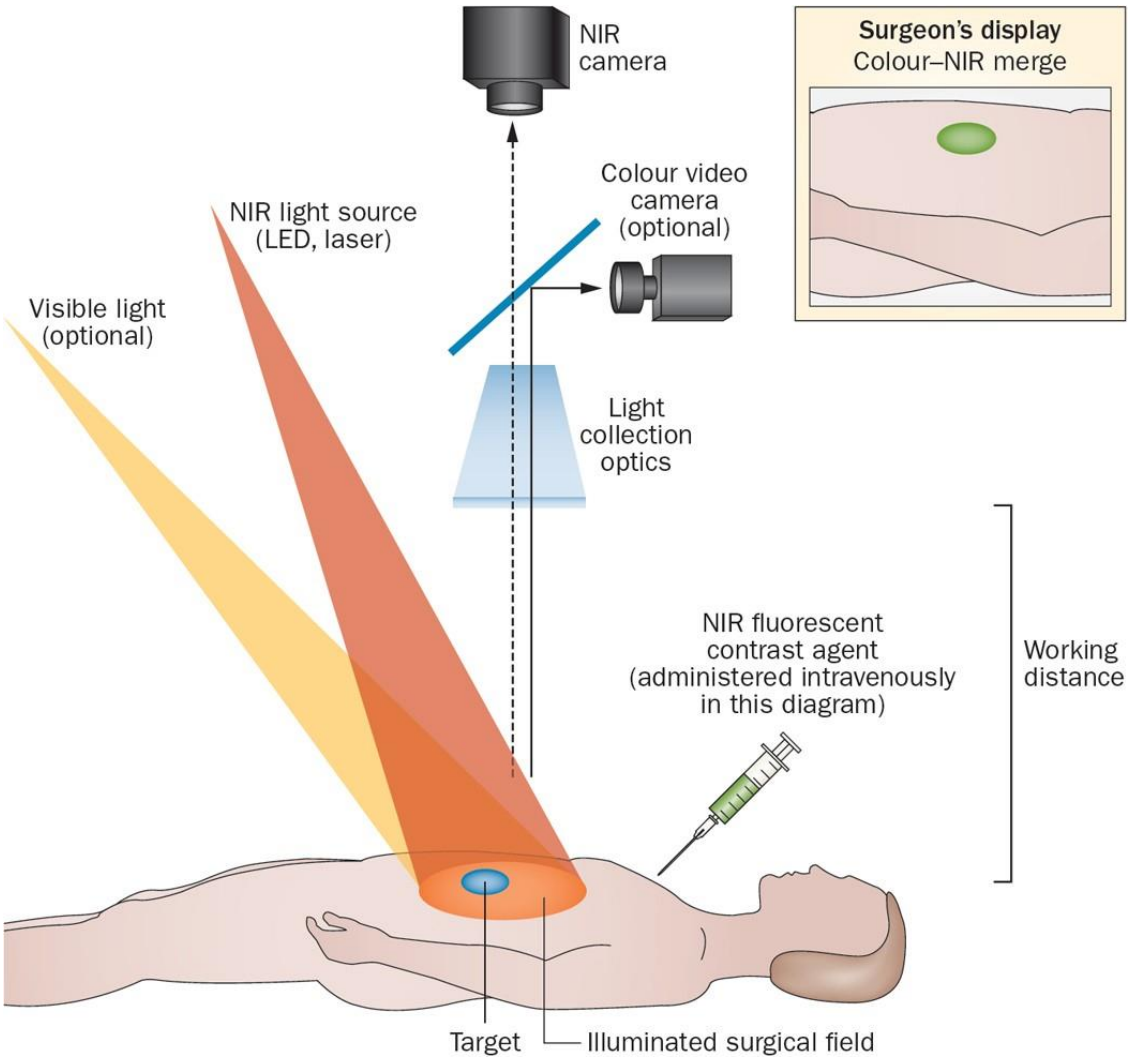

Figure 2. Fluorescent Guided Surgery (FGS) modality as a promising technology in the clinical setting. Reprinted by permission from Springer Nature Customer Service Center GmbH: Springer Nature, Nature Review Clinical Oncology (Image-Guided Cancer Surgery Using Near-Infrared Fluorescence, Alexander L. Vahrmeijer, Merlijn Hutteman, Joost R. van der Vorst, Cornelis J. H. van de Velde & John V. Frangioni), COPYRIGHT (2013).

Use of both image-guided surgery (MRI and ultrasound) and fluorescent guided surgery provides another level of detection of anatomical features for a surgeon. Utilizing NIR fluorescent light, which is invisible to the eye and requires specific lasers to excite and a detector to measure the response, can give surgeons a real time aid during surgery by fluorescing tissue at specific wavelengths between 700-900 nm[10, 11]. There are image-guided surgery instruments that are developed for NIR FGS which are FDA approved and currently being used in the clinic. These

instruments include the Fluoptics Fluobeam™, the Curadel Lab FLARE™, and others[10, 82-85]. Although there are only a small number of clinically approved image guided surgery instruments, research has rapidly grown in this area with new contrast agents being developed for use with these instruments[10, 85]. Fluorescent image-guided instrumentation utilized intraoperatively has advantages over the use of ultrasound or MRI alone. These can include identifying specific differences between healthy and diseased tissue, direct tissue contact, and providing intraoperative imaging guidance that facilitates the avoidance of anatomical structures, such as nerves and blood vessels[10, 12]. The ability for these instruments to be used intraoperatively and provide guidance during surgery is particularly beneficial during surgical interventions in areas where nerve damage is a large risk.

The aid of fluorescence imaging during a surgery benefits the surgeon by indicating a certain area to avoid (nerves) or to remove (tumor). In the case of avoiding a nerve area of interest, surgeons can decrease the number of nerve damage incidences occurred during surgery by the labeling of at-risk nerve sites. Nerve-specific contrast agents have become a promising intraoperative tool to be used in the image-guided surgery realm to prevent damage to nerve structures[86]. Designing nerve-specific fluorescent probes would enable these high-risk sites to be visualized during surgery. Nerves can be buried under muscle or other tissue structures leading to low visualization, but the nerve fluorescent probes utilized in image-guided surgery instruments can detect these hidden nerve sites[12, 32, 87-92]. The ability for visualization of these hidden nerve sites is crucial during a surgery. For example, in the head and neck region, the facial nerve courses through the parotid gland leading to difficulty in surgical operations on the gland[93]. Therefore, the design and development of nerve-specific fluorescent contrast agents would as an additional tool during surgical operations, especially in oncological procedures, that could minimize the risk of nerve damage.

Oncological procedures can present challenges for surgeons. Cancer tumors can hide vital anatomical structures, such as nerves, blood vessels, and other small organs which can pass through or under a tumor mass. Nerve bundles and small nerves can be visually obscured as they extend from an area of healthy tissue to an area of cancerous tissue. Image-guided surgery techniques would allow for the labeling of the hidden nerve sites within a tumor, enabling the tumor to be removed without causing damage to the nerves. The ability for fluorescent nerve contrast agents to function at nerve sites is due to proteins or biomarkers that allow for specific binding and prevent unspecific binding to other tissue.

The design and development of nerve-specific fluorescent contrast agents is essential for targeting high-risk sites for visualization during surgery. As nerve structures are quite small and are typically buried within the tissue layer, targeted fluorescent agents would allow for significantly improving visualization of nerves in the surgical field[12]. Different nerve regions are of significant interest for NIR-nerve specific contrast agents. These include the axon, myelin, and endoneurium regions present on all nerves[32, 86]. Each of these areas could be used for development to specifically target nerves for visualization.

Axonal targeted NIR contrast agents are absorbed through the axon where proteins or other substances are transported from the neurosome to nerve endings through retrograde axonal transport [94]. Specifically targeting nerve endings or the neurosome area on a nerve can allow for the transport of fluorescent contrast agents through a nerve. Retrograde nerve tracers, such as a subunit of the cholera toxin conjugated to the AlexaFluor™ 488, have been seen to label nerve axons following injection for detection of nerve damage, ultimately providing evidence that real-time intraoperative visualization of a nerve can be done through axonal retrograde transport[32, 95]. Additionally, binding to axonal regions may be required at the terminal ends of nerves due to the insulating layer, the myelin sheath, surrounding the axons,[32]. Targeting the myelin region is another area of potential interest for specific binding that can allow for systemic injection of a

particular contrast agent. Since myelin covers many nerve axons, targeting the myelin region could allow for cargo to be transported to the nerve body[32, 96, 97]. The agents targeting the myelin region will need to be carefully designed to prevent disruption of the myelin sheath and to not penetrate the blood brain barrier (BBB). Styryl pyridinium derivatives[98], distyrylbenzene derivatives[99-102], coumarin derivatives[103-106], and oxazine derivatives[82, 107-109] are good candidates for targeting nerves through the myelin region. Nerve-specific agents need to be further researched to enable specific targeting to a nerve, but many provide low toxicity, complete clearance, low non-specific binding, and good tissue penetration. Targeting different regions of a nerve by systemic administration are characterized by a few disadvantages including low tissue penetration, low signal-to-background (muscle) ratio (SBR), low signal-to-noise ratio (SNR), and lengthy circulation times from systemic injections. Nerve molecules naturally produced in the body, such as proteins, are another group of candidates in the development of nerve-specific contrast agents.

Neurotrophic factors are proteins that are present in the nervous system that each have specific roles to support the survival of the system. Each of these factors have specific receptors that mediate its respective biological activity[110]. Proteins that act as naturally occurring ligands found within the nervous system would be of significant benefit for use in development of nerve specific targets. Some neurotropic factors include nerve growth factor (NGF), brain derived neurotrophic factor (BDNF), and neurotrophin-3 (NT-3). These factors have specific receptors, tropomyosin kinase receptors A, B, and C (TrkA, B, and C), that function as key regulators in the nervous system survival and growth. (**Figure 3**). Neurotrophins and Trk receptors are not only an essential part of the nervous system, they also play a broader role in the immune system[111]. The Trk receptors can be found within the nervous system at different expression levels. For instance, the peripheral nervous system (PNS) has high expression levels of TrkA and TrkC, while the central nervous system (CNS) is characterized by high TrkB expression levels[112, 113]. Therefore,

the next generation of nerve-specific contrast agents could utilize the naturally occurring neurotrophic factor proteins as a backbone to improve binding and ultimately the visualization of nerves.

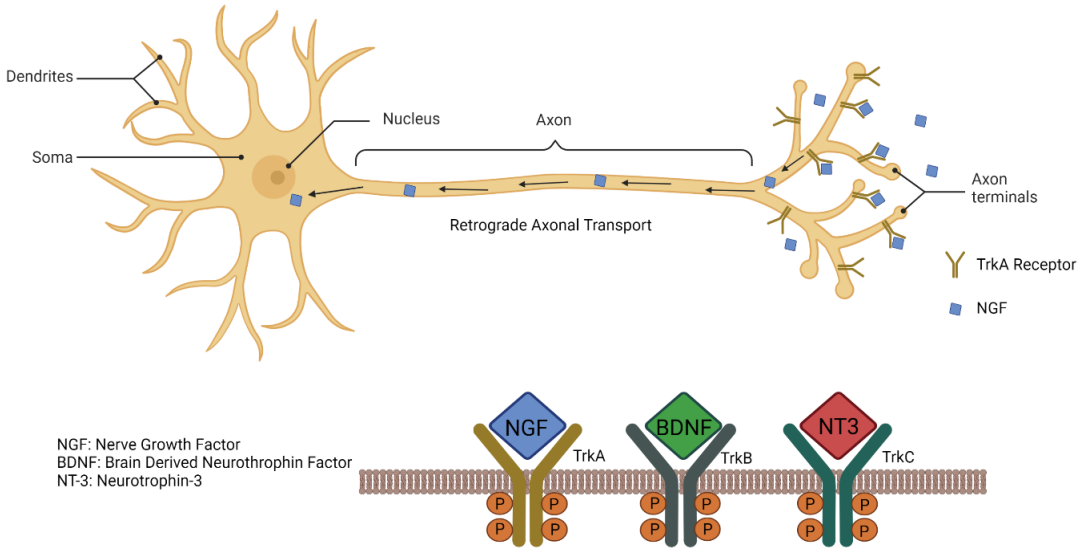

Figure 3. Neurotrophins and their binding receptors. Created using biorender.com.

Lastly, the location of the injection of contrast agents plays a role in the binding effectiveness of a nerve-specific contrast agent. Depending on the end goal of a conjugate and the type of disease, systemic or local routes of administration may provide a better delivery route to the targeted tissue. The route of administration for the delivery of conjugates to nerves is determined by the location site and composition of the nerve-specific contrast agent. During surgery for visualizing nerves, local administration allows a contrast agent to be directly applied at the target site, enabling the intended amount to accumulate at the site[109, 114]. Direct administration of a contrast agent during surgery would label only the at-risk nerves during surgery rather than potentially labeling all nerves by systemic injection. Systemic injection is often used in the clinic due to the ease of administration, but a higher dose is often needed to reach the intended target site due to circulation time as once the contrast agent reaches the site, the SBR and SNR may be much lower[114]. Specific clinical scenarios, such as nerve preservation,

could allow for a lower dose to be administered due to direct application at the target site and the potential for a surgeon to reapply the contrast agent during surgery to an area. Optimization of the direct administration technique is needed before integration into a surgical procedure, especially for surgeries that have limited timeframes. By optimizing the direct application approach for at-risk nerve sites, local administration could improve the labeling and resulting visualization of at-risk nerves during surgical intervention reducing nerve damage complications.

In developing nerve-specific fluorescent contrast agents, imaging of nerves would significantly reduce the risk of nerve damage and consequential outcomes. Prevalence of chronic pain and loss of nerve function are a few of the consequences of nerve damage following surgical interventions[47, 50-58]. Visualization of nerves during surgeries would aid surgeons with an imaging tool that can supplement their skillset by indicating where at-risk nerve sites are located. This additional tool has the potential to impact many patients as surgical procedures are a common treatment for oncology patients to remove all cancerous tissue and preserve other vital structures, including nerves[12, 61, 115, 116]. Many neurological diseases may also benefit from the development of nerve-specific contrast agents that can be utilized to label damaged nerve tissue or inflammation[117-120]. Nerves are quite small, found in nerve bundles, and can be buried in the surrounding tissue, all factors that make real-time visualization challenging without the use of fluorescent imaging. A nerve targeting agent would need to be selected with a good emission profile, non-toxic, and provide a high SBR in the NIR emission window for nerve selectivity over other tissue[10, 11]. Despite challenges, there is a clinical need to develop a NIR nerve-specific contrast agent to assist in visualizing nerves during surgical intervention, preserving nerves, and reducing the risk of nerve damage and post-surgical consequences.

Bibliography

1. Ludwig, P. E.; Reddy, V.; Varacallo, M., Neuroanatomy, Central Nervous System (CNS). **2017**.

2. Oosting, P., Signal Transmission in the Nervous System. *Rep. Prog. Phys.* **1979**, *42* (9), 1479.

3. Holmes, D.; Reading-Ikkanda, L., Repairing the Neural Highway. *Nature.* **2017**, *552* (7684), S50-S51.

4. Koht, A.; Sloan, T. B.; Hemmer, L. B., et al., Neuromonitoring in Surgery and Anesthesia. *UpToDate. Waltham: UpToDate.* **2015**.

5. Mazzone, S.; Esposito, A.; Giacomarra, V., Continuous Intraoperative Nerve Monitoring in Thyroid Surgery: Can Amplitude Be a Standardized Parameter? *Front. Endocrinol.* **2021**, 873.

6. Ghatol, D.; Widrich, J., Intraoperative Neurophysiological Monitoring. *StatPearls [Internet]*. **2020**.

7. Ghani, U.; Assad, S.; Assad, S., Role of Intraoperative Nerve Monitoring During Parathyroidectomy to Prevent Recurrent Laryngeal Nerve Injury. *Cureus.* **2016**, *8* (11).

8. Timmermann, W.; Dralle, H.; Hamelmann, W., et al., Does Intraoperative Nerve Monitoring Reduce the Rate of Recurrent Nerve Palsies During Thyroid Surgery? *Zentralbl. Neurochir.* **2002**, *127* (5), 395-399.

9. Harper, C. M., Intraoperative Cranial Nerve Monitoring. *Muscle Nerve.* **2004**, *29* (3), 339-351.

10. Eisele, D. W.; Wang, S. J.; Orloff, L. A., Electrophysiologic Facial Nerve Monitoring During Parotidectomy. *Head Neck.* **2010**, *32* (3), 399-405.

11. Silverstein, H.; Rosenberg, S., Intraoperative Facial Nerve Monitoring. *Otolaryngol. Clin. N. Am.* **1991**, *24* (3), 709-725.

12. Harner, S. G.; Daube, J. R.; Beatty, C. W., et al., Intraoperative Monitoring of the Facial Nerve. *Laryngoscope.* **1988**, *98* (2), 209-212.

13. Kartush, J. M., Electroneurography and Intraoperative Facial Monitoring in Contemporary Neurotology. *Otolaryngol. Head Neck Surg.* **1989**, *101* (4), 496-503.

14. Nuwer, M. R.; Daube, J.; Fischer, C., et al., Neuromonitoring During Surgery. Report of an IFCN Committee. *Electroencephalogr. Clin. Neurophysiol.* **1993**, *87* (5), 263-276.

15. Gantz, B. J., Intraoperative Facial Nerve Monitoring. *Am. J. Otol.* **1985**, 58-61.

16. Dong, C. C.; MacDonald, D. B.; Akagami, R., et al., Intraoperative Facial Motor Evoked Potential Monitoring with Transcranial Electrical Stimulation During Skull Base Surgery. *Neurophysiol. Clin. Neurophysiol.* **2005**, *116* (3), 588-596.

17. Meier, J. D.; Wenig, B. L.; Manders, E. C., et al., Continuous Intraoperative Facial Nerve Monitoring in Predicting Postoperative Injury During Parotidectomy. *Laryngoscope.* **2006**, *116* (9), 1569-1572.

18. Miller, M. C.; Spiegel, J. R., Identification and Monitoring of the Recurrent Laryngeal Nerve During Thyroidectomy. *Surg. Oncol. Clin. N. Am.* **2008**, *17* (1), 121-144.

19. Prell, J.; Rachinger, J.; Scheller, C., et al., A Real-Time Monitoring System for the Facial Nerve. *Neurosurgery.* 2010, *66* (6), 1064-1073.

20. Chen, Y.; Zhang, H.; Lei, Z., et al., Recent Advances in Intraoperative Nerve Bioimaging: Fluorescence-Guided Surgery for Nerve Preservation. *Small Struct.* **2020,** *1* (1), 2000036.

21. Walz, J.; Burnett, A. L.; Costello, A. J., et al., A Critical Analysis of the Current Knowledge of Surgical Anatomy Related to Optimization of Cancer Control and Preservation of Continence and Erection in Candidates for Radical Prostatectomy. *Eur. Urol.* **2010**, *57* (2), 179-192.

22. Gonzalez, A. A.; Jeyanandarajan, D.; Hansen, C., et al., Intraoperative Neurophysiological Monitoring During Spine Surgery: A Review. *Neurosurg. Focus.* **2009**, *27* (4), E6.

23. Asghar, J. K.; Shufflebarger, H. L., Intraoperative Neuro-Monitoring During Spondylolisthesis Surgery. *Spondylolisthesis.* **2015**, 331-338.

24. Moini, J.; Avgeropoulos, N.; Samsam, M., *Epidemiology of Brain and Spinal Tumors*. Academic Press: **2021**.

25. Gibbs, S. L., Near Infrared Fluorescence for Image-Guided Surgery. *Quant. Imaging Med. Surg.* **2012**, *2* (3), 177.

26. Haldeman, C. L.; Baggott, C. D.; Hanna, A. S., Intraoperative Ultrasound-Assisted Peripheral Nerve Surgery. *Neurosurg. Focus.* **2015**, *39* (3), E4.

27. Du, R.; Auguste, K. I.; Chin, C. T., et al., Magnetic Resonance Neurography for the Evaluation of Peripheral Nerve, Brachial Plexus, and Nerve Root Disorders. *Journal of Neurosurg.* **2010**, *112* (2), 362-371.

28. Zaidman, C. M.; Seelig, M. J.; Baker, J. C., et al., Detection of Peripheral Nerve Pathology: Comparison of Ultrasound and Mri. *Neurology.* **2013**, *80* (18), 1634-1640.

29. Chiou, H.-J.; Chou, Y.-H.; Chiou, S.-Y., et al., Peripheral Nerve Lesions: Role of High-Resolution Us. *Radiographics* **2003**, *23* (6), e15-e15.

30. Grant, G. A.; Britz, G. W.; Goodkin, R., et al., The Utility of Magnetic Resonance Imaging in Evaluating Peripheral Nerve Disorders. *Muscle Nerve.* 2002, *25* (3), 314-331.

31. Padua, L.; Liotta, G.; Di Pasquale, A., et al., Contribution of Ultrasound in the Assessment of Nerve Diseases. *Eur. J. Neurol.* **2012**, *19* (1), 47-54.

32. Kim, S.; Choi, J.-Y.; Huh, Y.-M., et al., Role of Magnetic Resonance Imaging in Entrapment and Compressive Neuropathy—What, Where, and How to See the Peripheral Nerves on the Musculoskeletal Magnetic Resonance Image: Part 2. Upper Extremity. *Eur. Radiol.* **2007**, *17* (2), 509-522.

33. Luzhansky, I. D.; Sudlow, L. C.; Brogan, D. M., et al., Imaging in the Repair of Peripheral Nerve Injury. *Nanomedicine.* **2019**, *14* (20), 2659-2677.

34. Mathieson, C.; Strongin, R., Nerve Tissue Targeted Fluorophore Synthesis: From Scheme to Administration. **2021**.

35. Rogers, M.; Henderson, L.; Mahajan, R., et al., Preliminary Findings in the Neurophysiological Assessment of Intercostal Nerve Injury During Thoracotomy. *European J. CardioThorac Surg.* **2002**, *21* (2), 298-301.

36. Borsook, D.; Kussman, B. D.; George, E., et al., Surgically-Induced Neuropathic Pain (Snpp): Understanding the Perioperative Process. *Ann. Surg.* **2013**, *257* (3), 403.

37. Mahan, M. A.; Spinner, R. J., Clinical Importance of Anatomic Variation of the Nerves of the Upper Extremity. In *Nerves and Nerve Injuries*, Elsevier: **2015**; pp 589-605.

38. Staff, N. P.; Engelstad, J.; Klein, C. J., et al., Post-Surgical Inflammatory Neuropathy. *Brain.* **2010,** *133* (10), 2866-2880.

39. Shipton, E.; Tait, B., Flagging the Pain: Preventing the Burden of Chronic Pain by Identifying and Treating Risk Factors in Acute Pain. *Eur. J. Anaesthesiol.* **2005**, *22* (6), 405-412.

40. VanDenKerkhof, E. G.; Hopman, W. M.; Towheed, T., et al., Pain, Health-Related Quality of Life and Health Care Utilization after Inpatient Surgery: A Pilot Study. *Pain Res. Manag.* **2006**, *11* (1), 41-47.

41. Haller, G.; Laroche, T.; Clergue, F., Morbidity in Anaesthesia: Today and Tomorrow. *Best Pract. Res. Clin. Anaesthesiol.* **2011**, *25* (2), 123-132.

42. O'Connor, A. B., Neuropathic Pain. *Pharmacoeconomics.* **2009**, *27* (2), 95-112.

43. Felder, J. M.; Ducic, I., Chronic Nerve Injuries and Delays in Surgical Treatment Negatively Impact Patient-Reported Quality of Life. *Plast. Reconstr. Surg. Glob. Open* **2021**, *9* (5).

44. Pelz, M.; Merskey, H., A Description of the Psychological Effects of Chronic Painful Lesions. *Pain.* **1982**, *14* (3), 293-301.

45. Novak, C. B.; Anastakis, D. J.; Beaton, D. E., et al., Patient-Reported Outcome after Peripheral Nerve Injury. *J. Hand Surg. Am.* **2009**, *34* (2), 281-287.

46. Novak, C. B.; Anastakis, D. J.; Beaton, D. E., et al., Biomedical and Psychosocial Factors Associated with Disability after Peripheral Nerve Injury. *J. Bone Joint Surg.* **2011**, *93* (10), 929-936.

47. Ring, D., Symptoms and Disability after Major Peripheral Nerve Injury. *Hand Clinics* **2013**, *29* (3), 421-425.

48. Kehlet, H.; Jensen, T. S.; Woolf, C. J., Persistent Postsurgical Pain: Risk Factors and Prevention. *Lancet.* **2006**, *367* (9522), 1618-1625.

49. Gioux, S.; Choi, H. S.; Frangioni, J. V., Image-Guided Surgery Using Invisible near-Infrared Light: Fundamentals of Clinical Translation. *Mol. Imaging.* **2010**, *9* (5), 7290.2010. 00034.

50. Burke, S., & Shorten, G. D., When Pain after Surgery Doesn't Go Away. *Biochem. Soc. Trans.* **2009**, 318-322.

51. Mondal, S. B.; Gao, S.; Zhu, N., et al., Real-Time Fluorescence Image-Guided Oncologic Surgery. *Adv. Cancer Res.* **2014**, *124*, 171-211.

52. Zhang, R. R.; Schroeder, A. B.; Grudzinski, J. J., et al., Beyond the Margins: Real-Time Detection of Cancer Using Targeted Fluorophores. *Nat. Rev. Clin.Oncol.* **2017**, *14* (6), 347-364.

53. Verbeek, F. P.; van der Vorst, J. R.; Schaafsma, B. E., et al., Intraoperative near Infrared Fluorescence Guided Identification of the Ureters Using Low Dose Methylene Blue: A First in Human Experience. *J. Urol.* **2013**, *190* (2), 574-579.

54. Dip, F. D.; Grecco, A. D. M.; Nguyen, D., et al., Ureter Identification Using Methylene Blue and Fluorescein. In *Fluorescence Imaging for Surgeons*, Springer: **2015**; pp 327-332.

55. Seif, C.; Portillo, F. J. M.; Osmonov, D. K., et al., Methylene Blue Staining for Nerve-Sparing Operative Procedures: An Animal Model. *Urology.* **2004**, *63* (6), 1205-1208.

56. Osorio, J. A.; Breshears, J. D.; Arnaout, O., et al., Ultrasound-Guided Percutaneous Injection of Methylene Blue to Identify Nerve Pathology and Guide Surgery. *Neurosurg. Focus.* **2015**, *39* (3), E2.

57. Candell, L.; Campbell, M. J.; Shen, W. T., et al., Ultrasound-Guided Methylene Blue Dye Injection for Parathyroid Localization in the Reoperative Neck. *World J. Surg.* **2014**, *38* (1), 88-91.

58. Gotoh, K.; Yamada, T.; Ishikawa, O., et al., A Novel Image-Guided Surgery of Hepatocellular Carcinoma by Indocyanine Green Fluorescence Imaging Navigation. *J. Surg. Oncol.* **2009**, *100* (1), 75-79.

59. Schaafsma, B. E.; Mieog, J. S. D.; Hutteman, M., et al., The Clinical Use of Indocyanine Green as a Near-Infrared Fluorescent Contrast Agent for Image-Guided Oncologic Surgery. *J. Surg. Oncol.* **2011**, *104* (3), 323-332.

60. Hill, T. K.; Abdulahad, A.; Kelkar, S. S., et al., Indocyanine Green-Loaded Nanoparticles for Image-Guided Tumor Surgery. *Bioconjug. Chem.* **2015**, *26* (2), 294-303.

61. Aoki, T.; Yasuda, D.; Shimizu, Y., et al., Image-Guided Liver Mapping Using Fluorescence Navigation System with Indocyanine Green for Anatomical Hepatic Resection. *World J. Surg.* **2008**, *32* (8), 1763-1767.

62. He, K.; Chi, C.; Kou, D., et al., Comparison between the Indocyanine Green Fluorescence and Blue Dye Methods for Sentinel Lymph Node Biopsy Using Novel Fluorescence Image-Guided Resection Equipment in Different Types of Hospitals. *Transl. Res.* **2016**, *178*, 74-80.

63. Yokoyama, J.; Ooba, S.; Fujimaki, M., et al., Impact of Indocyanine Green Fluorescent Image-Guided Surgery for Parapharyngeal Space Tumours. *J. CranioMaxillofac. Surg.* **2014**, *42* (6), 835-838.

64. Hadjipanayis, C. G.; Widhalm, G.; Stummer, W., What Is the Surgical Benefit of Utilizing 5-Aminolevulinic Acid for Fluorescence-Guided Surgery of Malignant Gliomas? *Neurosurgery.* **2015**, *77* (5), 663-673.

65. Lakomkin, N.; Hadjipanayis, C. G., Fluorescence-Guided Surgery for High-Grade Gliomas. *J. Surg. Oncol.* **2018**, *118* (2), 356-361.

66. Eljamel, S., 5-ALA Fluorescence Image Guided Resection of Glioblastoma Multiforme: A Meta-Analysis of the Literature. *Int.J. Mol. Sci.* **2015**, *16* (5), 10443-10456.

67. Liu, J. T.; Meza, D.; Sanai, N., Trends in Fluorescence Image-Guided Surgery for Gliomas. *Neurosurgery.* **2014**, *75* (1), 61-71.

68. Goedee, H. S.; van der Pol, W. L.; Hendrikse, J., et al., Nerve Ultrasound and Magnetic Resonance Imaging in the Diagnosis of Neuropathy. *Curr. Opin. Neurol.* **2018**, *31* (5), 526-533.

69. Kermarrec, E.; Demondion, X.; Khalil, C., et al. In Ultrasound and Magnetic Resonance Imaging of the Peripheral Nerves: Current Techniques, Promising Directions, and Open Issues, *Semin. Musculoskelet. Radiol.*, Thieme Medical Publishers: **2010**; pp 463-472.

70. Holzgrefe, R. E.; Wagner, E. R.; Singer, A. D., et al., Imaging of the Peripheral Nerve: Concepts and Future Direction of Magnetic Resonance Neurography and Ultrasound. *J. Hand Surg. Am.* **2012**, *44* (12), 1066-1079.

71. Walker, F. O.; Cartwright, M. S.; Wiesler, E. R., et al., Ultrasound of Nerve and Muscle. *Neurophysiol. Clin. Neurophysiol.* **2004**, *115* (3), 495-507.

72. Chance, B., Near-Infrared Images Using Continuous, Phase-Modulated, and Pulsed Light with Quantitation of Blood and Blood Oxygenation A. *Ann. N. Y. Acad. Sci.* **1998**, *838* (1), 29-45.

73. Barth, C. W.; Gibbs, S. L., Fluorescence Image-Guided Surgery: A Perspective on Contrast Agent Development. *Proc. SPIE Int. Soc. Opt. Eng. VI* **2020**, *11222*, 112220J.

74. Hill, T. K.; Mohs, A. M., Image-Guided Tumor Surgery: Will There Be a Role for Fluorescent Nanoparticles? *Wiley Interdiscipl. Rev.: Nanomed. Nanobiotechnol.* **2016**, *8* (4), 498-511.

75. Ashoka, A. H.; Kong, S.-H.; Seeliger, B., et al., Near-Infrared Fluorescent Coatings of Medical Devices for Image-Guided Surgery. *Biomaterials.* **2020**, *261*, 120306.

76. Chi, C.; Du, Y.; Ye, J., et al., Intraoperative Imaging-Guided Cancer Surgery: From Current Fluorescence Molecular Imaging Methods to Future Multi-Modality Imaging Technology. *Theranostics.* **2014**, *4* (11), 1072.

77. Walsh, E. M.; Cole, D.; Tipirneni, K. E., et al., Fluorescence Imaging of Nerves During Surgery. *Ann. Surg.* **2019**, *270* (1), 69-76.

78. Vahrmeijer, A. L.; Hutteman, M.; Van Der Vorst, J. R., et al., Image-Guided Cancer Surgery Using near-Infrared Fluorescence. *Nat. Rev. Clin. Oncol.* **2013**, *10* (9), 507-518.

79. Pedro, M. T.; Eissler, A.; Schmidberger, J., et al., Sodium Fluorescein–Guided Surgery in Peripheral Nerve Sheath Tumors: First Experience in 10 Cases of Schwannoma. *World Neurosurg.* **2019**, *124*, e724-e732.

80. Fanaropoulou, N. M.; Chorti, A.; Markakis, M., et al., The Use of Indocyanine Green in Endocrine Surgery of the Neck: A Systematic Review. *Medicine.* **2019**, *98* (10).

81. Gragnaniello, C.; Kamel, M.; Al-Mefty, O., Utilization of Fluorescein for Identification and Preservation of the Facial Nerve and Semicircular Canals for Safe Mastoidectomy: A Proof of Concept Laboratory Cadaveric Study. *Neurosurgery.* **2010**, *66* (1), 204-207.

82. Torres, V. C.; Vuong, V. D.; Wilson, T., et al., Cranial Nerve Contrast Using Nerve-Specific Fluorophores Improved by Paired-Agent Imaging with Indocyanine Green as a Control Agent. *J. Biomed. Opt.* **2017**, *22* (9), 096012.

83. Li, C.; Cao, L.; Zhang, Y., et al., Preoperative Detection and Intraoperative Visualization of Brain Tumors for More Precise Surgery: A New Dual-Modality Mri and Nir Nanoprobe. S*mall.* **2015**, *11* (35), 4517-4525.

84. Institute, N. C. Head and Neck Cancers.

85. Shao, L.; Song, B., Toxicity of Titanium Dioxide Nanoparticles on Brain. In *Neurotoxicity of Nanomaterials and Nanomedicine*, Elsevier: **2017**; pp 99-125.

86. Boyette, L. B.; Reardon, M. A.; Mirelman, A. J., et al., Fiberoptic Imaging of Cavernous Nerves in Vivo. *J. Urol.* **2007**, *178* (6), 2694-2700.

87. Poduslo, J. F.; Curran, G. L., Polyamine Modification Increases the Permeability of Proteins at the Blood-Nerve and Blood-Brain Barriers. *J. Neurochem.* **1996**, *66* (4), 1599-1609.

88. Poduslo, J. F.; Curran, G. L., Increased Permeability of Superoxide Dismutase at the Blood-Nerve and Blood-Brain Barriers with Retained Enzymatic Activity after Covalent Modification with the Naturally Occurring Polyamine, Putrescine. *J. Neurochem.* **1996**, *67* (2), 734-741.

89. Gibbs-Strauss, S. L.; Vooght, C.; Fish, K. M., et al., Molecular Imaging Agents Specific for the Annulus Fibrosus of the Intervertebral Disk. *Mol. Imaging.* **2010**, *9* (3), 7290.2010. 00009.

90. Hackman, K. M.; Doddapaneni, B. S.; Barth, C. W., et al., Polymeric Micelles as Carriers for Nerve-Highlighting Fluorescent Probe Delivery. *Mol. Pharm.* **2015**, *12* (12), 4386-4394.

91. Liu, W.; Gu, R.; Zhu, Q., et al., Rapid Fluorescence Imaging of Spinal Cord Following Epidural Administration of a Nerve-Highlighting Fluorophore. *Theranostics.* **2017**, *7* (7), 1863.

92. Wu, C.; Tian, D.; Feng, Y., et al., A Novel Fluorescent Probe That Is Brain Permeable and Selectively Binds to Myelin. *J. Histochem. Cytochem.* **2006**, *54* (9), 997-1004.

93. Cotero, V. E.; Siclovan, T.; Zhang, R., et al., Intraoperative Fluorescence Imaging of Peripheral and Central Nerves through a Myelin-Selective Contrast Agent. *Mol. Imaging Biol.* **2012**, *14* (6), 708-717.

94. Wang, C.; Wu, C.; Popescu, D. C., et al., Longitudinal Near-Infrared Imaging of Myelination. *J. Neurosci.* **2011**, *31* (7), 2382-2390.

95. Wang, C.; Wu, C.; Zhu, J., et al., Design, Synthesis, and Evaluation of Coumarin-Based Molecular Probes for Imaging of Myelination. *J. Med. Chem.* **2011**, *54* (7), 2331-2340.

96. Gibbs, S. L.; Xie, Y.; Goodwill, H. L., et al., Structure-Activity Relationship of Nerve-Highlighting Fluorophores. *PloS One.* **2013**, *8* (9), e73493.

97. Wu, C.; Wei, J.; Tian, D., et al., Molecular Probes for Imaging Myelinated White Matter in Cns. *J. Med. Chem.* **2008**, *51* (21), 6682-6688.

98. Park, M. H.; Hyun, H.; Ashitate, Y., et al., Prototype Nerve-Specific Near-Infrared Fluorophores. *Theranostics.* **2014**, *4* (8), 823.

99. Wang, L. G.; Barth, C. W.; Kitts, C. H., et al., Near-Infrared Nerve-Binding Fluorophores for Buried Nerve Tissue Imaging. *Sci. Transl. Med.* **2020**, *12* (542), eaay0712.

100. Barth, C. W.; Gibbs, S. L., Direct Administration of Nerve-Specific Contrast to Improve Nerve Sparing Radical Prostatectomy. *Theranostics.* **2017**, *7* (3), 573.

101. Razavi, S.; Nazem, G.; Mardani, M., et al., Neurotrophic Factors and Their Effects in the Treatment of Multiple Sclerosis. *Adv. Biomed. Res.* **2015**, *4*.

102. Vega, J. A.; García-Suárez, O.; Hannestad, J., et al., Neurotrophins and the Immune System. *J. Anat.* **2003**, *203* (1), 1-19.

103. Vigneswara, V.; Kundi, S.; Ahmed, Z., Receptor Tyrosine Kinases: Molecular Switches Regulating Cns Axon Regeneration. *J. Signal Transd.* **2012**, *2012*.

104. Nikoletopoulou, V.; Lickert, H.; Frade, J. M., et al., Neurotrophin Receptors TrkA and TrkC Cause Neuronal Death Whereas Trkb Does Not. *Nature.* **2010**, *467* (7311), 59-63.

105. Serwer, L.; Hashizume, R.; Ozawa, T., et al., Systemic and Local Drug Delivery for Treating Diseases of the Central Nervous System in Rodent Models. *J. Vis. Exp.: JoVE* **2010**, (42).

106. Rosenthal, E. L.; Warram, J. M.; De Boer, E., et al., Successful Translation of Fluorescence Navigation During Oncologic Surgery: A Consensus Report. *J. Nucl. Med.* **2016**, *57* (1), 144-150.

107. Gilson, S.; Stone, E., Principles of Oncologic Surgery. *Compendium on Continuing Education for the Practicing Veternarian.* **1990**, *12* (6), 827-838.

108. Petersen, M. A.; Ryu, J. K.; Akassoglou, K., Fibrinogen in Neurological Diseases: Mechanisms, Imaging and Therapeutics. *Nat. Rev. Neurosci.* **2018**, *19* (5), 283-301.

109. Misgeld, T.; Kerschensteiner, M., In Vivo Imaging of the Diseased Nervous System. *Nat. Rev. Neurosci.* **2006**, *7* (6), 449-463.

110. Zhang, B.; Yan, W.; Zhu, Y., et al., Nanomaterials in Neural-Stem-Cell-Mediated Regenerative Medicine: Imaging and Treatment of Neurological Diseases. *Adv. Mater.* **2018**, *30* (17), 1705694.

111. Xu, D.; Wu, D.; Qin, M., et al., Efficient Delivery of Nerve Growth Factors to the Central Nervous System for Neural Regeneration. *Adv. Mater.* **2019**, *31* (33), 1900727.

CHAPTER 3: TARGETED INTRAOPERATIVE FLUORESCENT IMAGING OF FACIAL NERVES

Abstract

Purpose: Nerve damage during surgical procedures can significantly affect a patient's quality of life. There is an increased need to preserve nerve function and FGS is a promising candidate. FGS enables surgeons to precisely maneuver their instruments around hidden nerve sites during procedures. Nerve visualization to help ensure the safety of nerves, especially during head and neck procedures, is a clinical need and solving it could improve the quality of life for numerous patients every year.

Procedures: Evaluating a nerve-specific fluorescent contrast agent may provide a solution to visualize facial nerves during intraoperative procedures. This agent, Nervelight™, consists of an 800 nm NIR dye attached to a naturally occurring protein, NGF. The performance of Nervelight™ will be compared to the performance of a control dye intended for a similar purpose.

Results: In these studies, topical application of Nervelight™ on the targeted facial nerve provided evidence of specific labeling after just minutes. These results show that Nervelight™ could successfully serve as an image guiding tool during surgery.

Conclusions: Fluorescent imaging of nerves can enable surgeons to visualize at-risk nerves during head and neck procedures. The development of Nervelight™ would improve a clinical need of preserving nerve function and reducing nerve damage.

Introduction

Cancer continues to impact patients around the world with high mortality and morbidity rates[1]. Research continues to be done related to cancerous tumors and a variety of new treatment options and research opportunities allow scientists to explore new ways to combat disease. Head and neck cancers (benign or malignant) which total to 4% of cancers are localized to the throat,

mouth, larynx, nose, salivary glands, and eyes. There are three major salivary glands (parotid, submandibular, and sublingual), and roughly 80% of salivary gland cancers begin in the parotid gland[2, 3]. Resection of these tumors are difficult due to the presence of small anatomical structures and complicated further by the location of these features. Surgery is a common strategy for acute and chronic diseases, including cancer[4, 5], however, many surgeries are completed under white light, and shaped predominantly a surgeon's skill of knowing the location of small structures. Intra-operative guidance allows for visualization of small structures, such as nerves. Nerve damage is a major cause of pain and loss of function of nerves after surgical interventions, some of which include prostatectomies[6-9], head and neck surgeries[10, 11], and breast cancer surgeries[12-16]. The resulting damage can lead to loss of function, weakness, chronic pain, or paralysis of nerves[10, 15-21]. The need for surgeons to perform surgical procedures consistently and reliably on patients without instigating complications has become a critical issue to solve. FGS is becoming a popular tool to aid surgeons during surgical procedures[4, 17].

Unintentional nerve damage is a significant risk of surgical procedures and can have lasting consequences for the patient. This is especially concerning in areas present with many nerve branches, such as the facial nerve area. Nerve anatomy is expansive and highly variable between patients. Add in the challenges of visually locating and tracking nerves during surgery and it is clear why surgeons face significant challenges when attempting to completely resect tumor and spare surrounding nerves[10, 17, 22]. Nerves can be found embedded in the muscle tissue challenging nerve detection which leads to an increased risk of nerve damage which then leads to adverse consequences such as pain or loss of nerve function, consequences that may persist long after the surgical procedure is complete.

Injury to the facial nerve from surgery or trauma impairs the nerve's ability to properly function which can result in paralysis of the facial muscles, restrictions in facial movement, weakness, and functional impediments such as constant drooling, loss of feeling, and an impaired

blink reflex[10, 23]. The consequential injury of the facial nerve can be devastating to a patient, in which simple tasks such as smiling, which requires muscle movement on the face, would be impossible. The facial nerve or the seventh cranial nerve is responsible for a multitude of facial expressions including anger, pain, fear, smiling, salivating, as well as the movement of the mouth, lips, and ears[24]. The facial nerve encompasses motor, sensory and parasympathetic fibers and is one of the most common nerves to be impacted by disease[24]. As illustrated in **Figure 4 A-B**, the anatomy of the facial nerve is complex, with five main branches (Temporal, Zygomatic, Buccal, Marginal, and Cervical). The preauricular incision method is a commonly performed clinical procedure that can easily expose the facial area (**Figure 4 C**)[25].

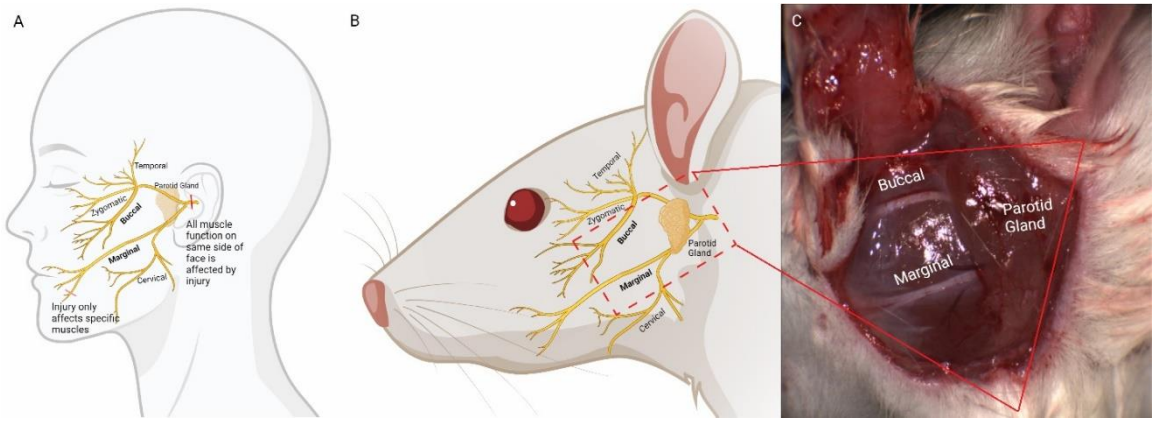

Figure 4. Facial nerve anatomy **(A)** Map of facial nerve branches and location of an injury determines extent of function loss. Adapted from "Trigeminal Nerve", by BioRender.com (2021). Retrieved from https://app.biorender.com/biorender-templates. **(B)** Rat facial nerve locations. Adapted from "Rat Head (lateral)", by BioRender.com (2021). Retrieved from https://app.biorender.com/biorender-templates. **(C)** Live rat image of the Buccal and Marginal branches conducted on the Curadel Lab FLARE™.

Nerve damage causes 10-50% of patients to experience some type of chronic neuropathic pain following surgery[26, 27]. The need for facial nerve preservation by preventing unintentional nerve damage following surgical procedures is critical. Fluorescently labeling this nerve would reduce the chances of damage and therefore reduce the consequences affiliated with that damage.

FGS provides the necessary intraoperative optical tool allowing surgeons to visualize nerves in real time, ultimately reducing nerve damage during surgeries[15, 17].

In this study, we examine the ability of a contrast agent termed Nervelight™, an NIR dye conjugated to a naturally occurring nervous system protein, NGF, to fluoresce the facial nerve intra-operatively. NGF is found to bind readily to TrkA receptors that is present in nerves[28-30]. This nerve-targeted contrast agent would provide a tool to aid surgeons during surgery to reduce the risk of nerve damage. Here, we evaluated the function of the Nervelight™ in a dose-range study on the facial nerve, using local delivery in the open surgical cavity. The goal of this study was to investigate the nerve fluorescent capacity of Nervelight™ as an image guiding tool which surgeons can use to decrease the risk of unintentional nerve damage during head and neck procedures.

Materials and Methods

Nervelight™ contrast agent

Nervelight™ is the conjugation of a naturally occurring nervous system recombinant protein, NGF, to a NIR fluorescent dye, provided by Manzanita Pharmaceuticals (Woodside, CA). Analytics and conjugation were completed by Abzena Pharmaceuticals (Bristol, PA), and to confirm the function of NGF after conjugation to a NIR dye, a neuronal survival bioassay was conducted (Pamela Lein, PhD Laboratory, University of California at Davis; Davis, CA). The sample absorption and emission spectra of the Nervelight™ were performed on the ThermoFisher Scientific Evolution 220 UV-Visible Spectrophotometer (Waltham, MA, USA) and a Horiba Scientific FluoroMax-4 (Edison, New Jersey, USA). Both Nervelight™ and an NIR unmodified control dye were examined with a dose-range study of three doses: 1.75 nmol, 0.87 nmol, and 0.35 nmol of NIR dye.

Animal model

All animal work was performed under an approved protocol by the University of Nebraska Medical Center Institutional Animal Care and Use Committee (IACUC). Male Sprague-Dawley rats were purchased from Charles River Laboratories (Wilmington, MA) ranging in body weight from 320-400g. All applicable institutional and/or national guidelines for the care and use of animals were followed.

Topical application procedure and study design

Sprague Dawley rats were euthanized and separated into two experimental groups (n = 9 rats per group): (1) Nervelight™ contrast agent and (2) unmodified NIR control dye. Rats were anesthetized using 4% isoflurane in oxygen and monitored for the duration of the procedure. A preauricular incision[25] was made along the left side of the face to expose the Buccal and Marginal branches of the facial nerve. Anesthetic levels were lowered to 3% in oxygen following surgery and animals were continuously monitored by toe pinching. Nervelight™ or control dye equivalent doses (50 µl of the 1.75, 0.87, and 0.35 nmol of NIR dye) were topically applied to the exposed nerve branches for 10 mins (**Table 1**). Following 10 mins of incubation, three washes of 100 µl Phosphate Buffered Saline (PBS) (Corning; Corning, NY) was administered to the area to remove any unbound agent.

Dose	Nervelight™	NIR Control Dye Equivalent
1.75 nmol of NIR dye	50 µg/ml	1.67 µg/ml
0.87 nmol of NIR dye	25 µg/ml	0.83 µg/ml
0.35 nmol of NIR dye	10 µg/ml	0.33 µg/ml

Table 1. Doses of Nervelight™ and NIR control dye equivalent.

Near infrared fluorescence imaging

Intraoperative imaging was performed by a FGS imaging system. The Curadel Lab FLARE™ (Curadel, LLC; Natick, MA, USA) was used to capture the visible color and NIR fluorescence (NIR range of 800-1000 nm), using the exposure times of 50, 138.04 and 200 ms. FGS images were collected at timepoints of 0^+ (immediately following PBS washes), 15, 30, and 60 mins after washing steps that followed the topical application. The nerve and muscle mean fluorescent signals were quantified using the ImageJ 1.52v software (National Institutes of Health, Bethesda, MD, USA) by the following equation: $SBR = \frac{mean\ nerve\ fluorescent\ signal}{mean\ muscle\ fluorescent\ signal}$ [31].

Following the 60-minute timepoint, the rats were euthanized by decapitation and the nerves and organs were excised for imaging using the LI-COR Pearl Trilogy small animal imaging system (LI-COR; Lincoln, NE, USA) with both white and 800 nm (785 nm excitation, 820 nm emission) channels. The fluorescent intensity was determined for the nerve and organ regions of interest and were analyzed by Image Studio Version 5.0 software (LI-COR Biosciences, Lincoln, NE, USA). The SNR values were quantified by the following equation: $SNR = \frac{mean\ organ\ fluorescent\ signal}{background\ standard\ deviation}$ [31].

Histological Analysis

The resected nerves and organs were placed in Tissue-Tek O.C.T. Compound gel (Sakura Finetek USA; Torrence, CA). Frozen O.C.T. samples were sectioned on a Cryostat Tissue Sectioning System (Leica Biosystems; Buffalo Grove, Il) at 8 μm sections. Samples were air dried for 30 minutes, placed in cold acetone for 10 minutes, and air dried for an additional 30 minutes. Fluorescent images were captured using the Olympus IX73 inverted Fluorescent Microscope utilizing the brightfield, FITC (513-556 nm emission), and NIR (700-1000 nm emission) channels on the Olympus fluorescent microscope (Olympus Life Sciences; Waltham, MA). Further confirmation of the nerves was completed by histology (Hematoxylin and Eosin staining) and immunohistochemistry (IHC) techniques with a nerve-targeting antibody, TrkA. For histological

staining, samples were (1) placed in Mayer's Hematoxylin Solution (IHC World; Woodstock, MD) for two minutes, (2) rinsed in running water for two minutes, (3) rinsed in 95% ethanol solution for 30 seconds, (4) counterstained in Eosin Solution (IHC World; Woodstock, MD) for 45 seconds, (5) 95% ethanol solution rinse, (6) two 5 minute changes of 100% ethanol solution, (7) cleared in two 5 minute changes of xylenes, and (8) dried and sealed with Cytoseal 280 mounting media (Richard-Allan Scientific; Kalamazoo, MI) and covered (Thermo Scientific Company LLC). For immunohistochemistry staining, (1) sections were encompassed by a hydrophobic barrier by an ImmEDGE Hydrophobic Barrier Pen (Vector Laboratories; Burlingame, CA), (2) PBS wash, (3) 100 µl of 0.2% Triton X-100 solution (Sigma-Aldrich; St. Louis, MO) for 10 minutes, (4) PBS wash, (5) 100 µl 0.3% Hydrogen Peroxide solution (Fisher Scientific; Waltham, MA) for 5 minutes, (6) PBS wash, (7) 100 µl Blocking Buffer solution [10% Goat serum (IGT-SER-10ml Innovative Grade US Origin Goat Serum; Novi, MI), 1% Bovine Serum Albumin (Sigma-Aldrich; St. Louis, MO) and 89% PBS] for 1 hour, (8) PBS wash, (9) 100 µl of 1:1000 Trk A primary antibody (abcam; Cambridge, UK) overnight at 4 °C, (10) PBS wash, (11) 100 µl 1:1000 Peroxidase-conjugated AffiniPure Goat Anti-Rabbit IgG secondary antibody (Jackson Immuno Research Laboratories; West Grove, PA) for 2 hours, (12) PBS wash, (13) 100 µl of ImmPACT DAB Peroxidase Substrate (Vector Laboratories; Burlingame, CA) for 5 to 8 minutes, (14) rinse under water, (15) counterstained in Hematoxylin solution, (16) rinse under water, (17) dried and mounted. This process was adapted from the antibody manufacturer's standard IHC protocol (abcam, United Kingdom). The Olympus IX73 inverted fluorescent microscope was used for imaging both histological and IHC sections via the brightfield channel.

Data Analysis

All statistical analysis was performed using Microsoft Excel version 16051.15 (Microsoft Corporation). ANOVA: single factor was used to compare Nervelight™ dose-dependency and to compare time-dependency of Nervelight™ or NIR dye. Unpaired t-tests were used to compare SBR values between the contrast agents at each timepoint within the 0.87 nmol group as well as

comparing the Nervelight™ and NIR control dye organ SNR values within dose groups. P-values < 0.05 were considered statistically significant.

Results

Chemical and optical characterization of Nervelight™

The chemical structure of Nervelight™ (**Figure 5 A**) consists of the conjugation of an NIR dye to a lysine residue (away from the binding site to TrkA) on the recombinant NGF protein (9 possible lysine sites on a NGF monomer) via an amide bond. The spectral measurements of Nervelight™ were performed to confirm presence of the NIR dye (**Figure 5 B**). The absorbance spectra was collected between 600 and 900 nm; the observed maximum at 788 nm was similar to the NIR dye absorption maximum. The fluorescence emission collected between 798 and 900 nm demonstrated an emission peak at 797 nm, consistent with the location of the emission peak of the NIR dye. The fluorescent properties of Nervelight™ provided confirmation of dye presence in the contrast agent.

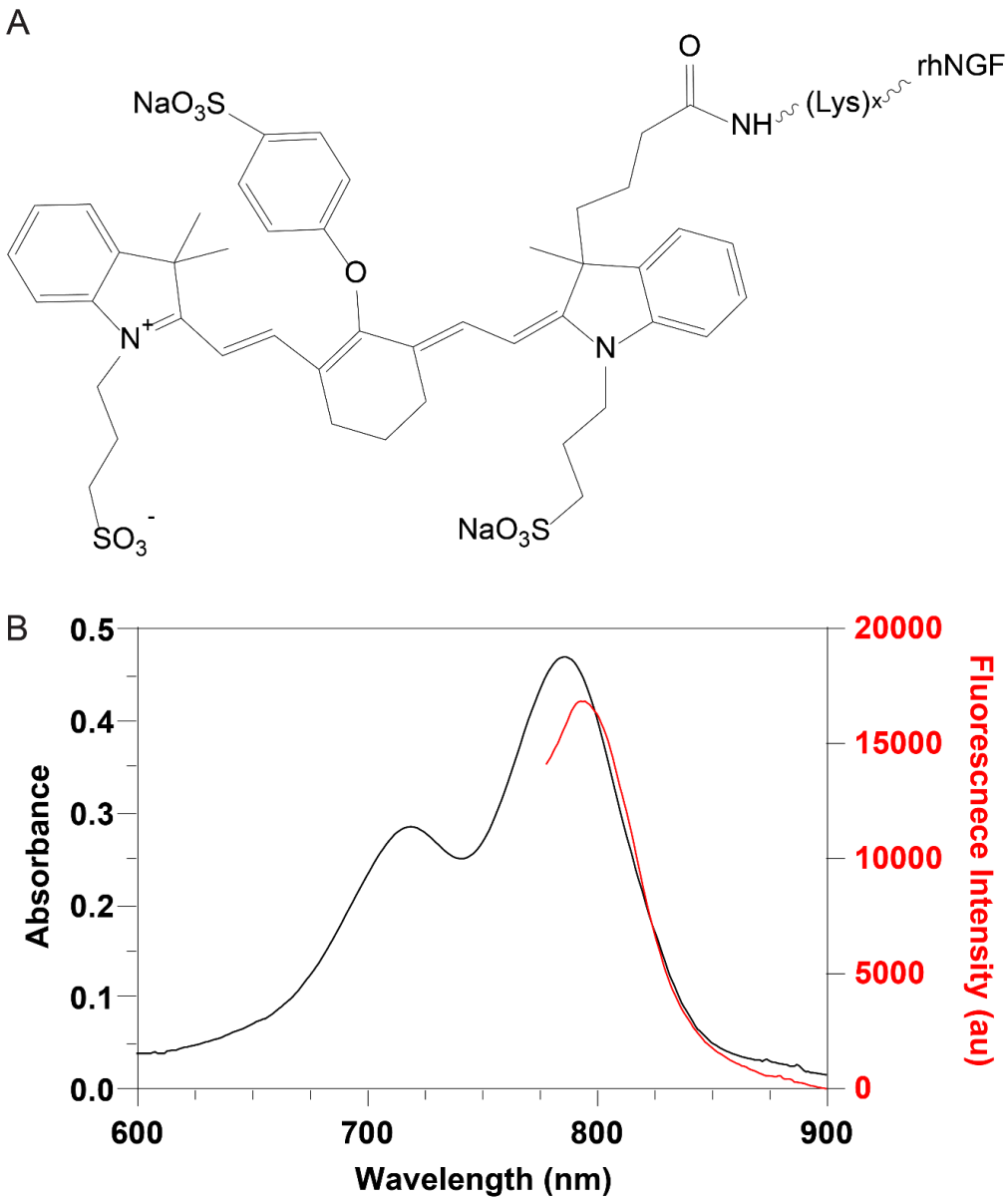

Figure 5. (A) Nervelight™ structure after conjugation with a NIR dye. **(B)** Absorbance and fluorescence spectra of 50 µg/ml Nervelight™ dose.

Nervelight™ facial nerve topical application procedure

Nervelight™ and unmodified NIR control dye were evaluated on rat Buccal and Marginal facial nerve branches. A dose-range study was performed to evaluate the upper and lower bounds of the Nervelight™ agent. **Figure 6** provides the topical application and imaging timeline for

Nervelight™ on the facial nerve. Intraoperative images were captured at the timepoints of 0^{+} (immediately following PBS washes), 15, 30, and 60 mins post-topical application and washes.

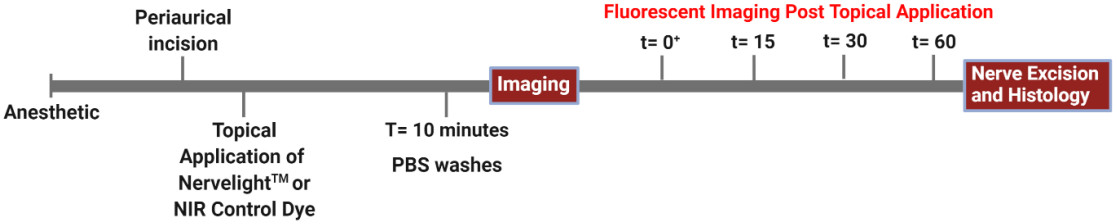

Figure 6. Schematic timeline of Nervelight™ topical application procedure and associated imaging on the facial nerve. Created using Biorender.com.

Nervelight™ dose range finding study

Three different doses of Nervelight™ and NIR control dye equivalent (00.35, 0.87, and 1.75 nmol of NIR dye) were evaluated at several timepoints following topical application, Representative intraoperative images are shown in **Figure 7**. In each of the Nervelight™ panels, we observed strong fluorescent signal on the nerve sites immediately following the incubation timeframe. The fluorescent signal in the nerve areas with the higher doses (0.87 and 1.75 nmol) of Nervelight™ appeared to at these sites. The highest dose (1.75 nmol) showed the most fluorescence signal at the 60 min timepoint. In contrast, the NIR control dye equivalent was observed to be washed off by PBS after application. Following 15 minutes of intraoperative imaging, the NIR control dye was observed to dissipate nearly entirely from the facial area, while the Nervelight™ signal remained present. The representative images suggest that the detectable Nervelight™ fluorescent signal was present for 60 min and was found to highlight the exposed facial nerve branches post-topical application.

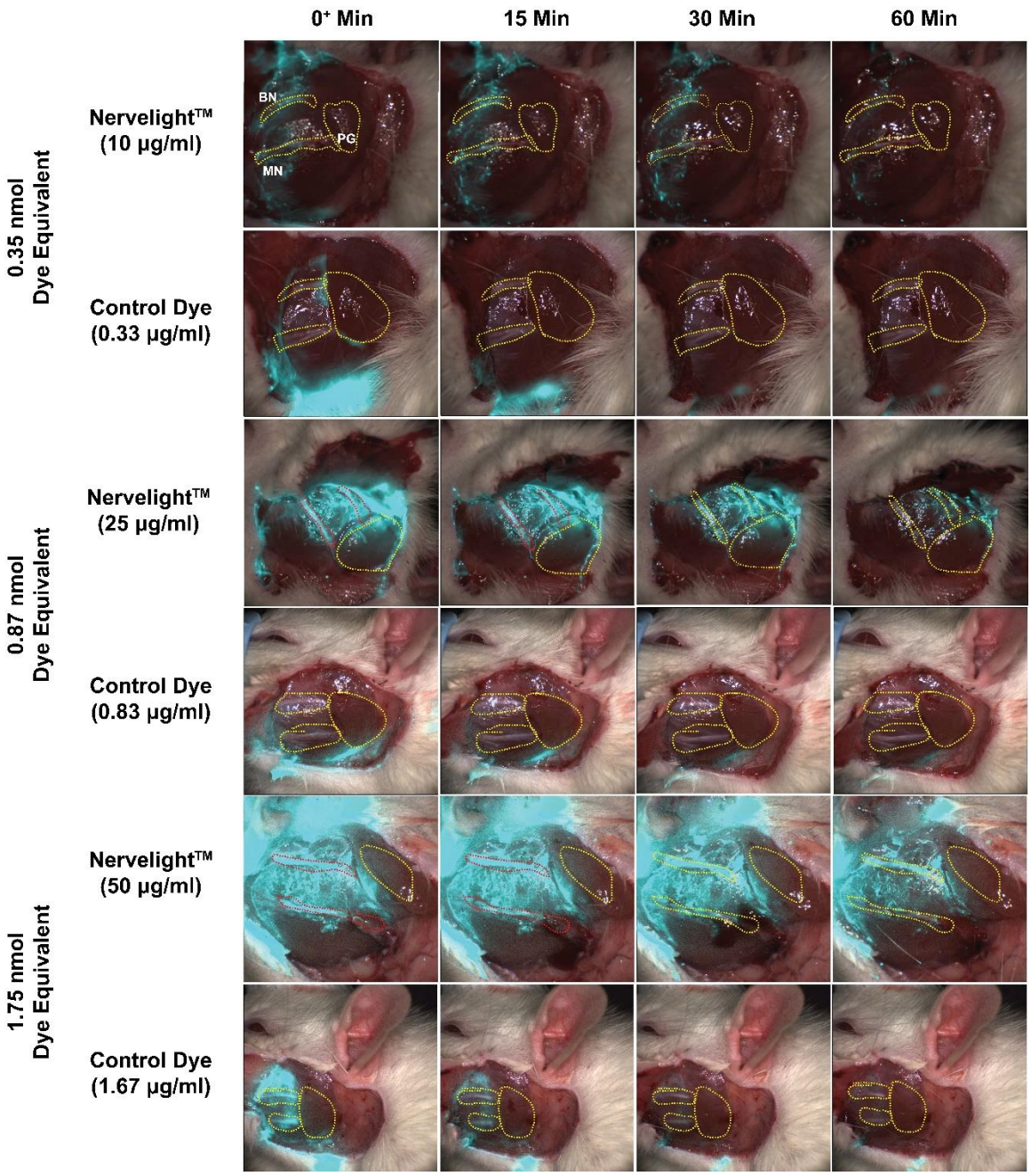

Figure 7. Representative time course intraoperative images of Nervelight™ and NIR control dye in the facial nerve area on anesthetized rats. Three doses (0.35, 0.87, and 1.75 nmol of NIR dye equivalent) were evaluated. BN: Buccal Nerve, MN: Marginal Nerve, and PG: Parotid Gland

Analysis of Nervelight™ dose-dependency and time-dependency

The analysis of the Nervelight™ and unmodified NIR control dye was done by examining the SBR and dose response curves. These curves provide necessary details regarding the nerve signal intensity in comparison to the signal observed in the muscle tissue. The dose response curves were analyzed to evaluate whether Nervelight™ was dose dependent. The results in **Figure 8 A-H** provide evidence that this Nervelight™ contrast agent is not dose-dependent in either the Buccal or Marginal nerve sites as the differences in fluorescent signal were not statistically significant between dose levels. Since Nervelight™ did not show dose-dependency, further evaluation was focused on the intermediate dose, 0.87 nmol, to determine if time had any effect on the nerve signal. Nervelight™ and the NIR dye equivalent were not observed to have a time-dependency over the procedure timeframe (**Figure 8 I-J**), suggesting that time does not influence the fluorescent nerve signal. To determine if Nervelight™ provides higher nerve signal over the NIR dye at any of the timepoints, comparisons were made between the groups. The intermediate dose group of Nervelight™ was observed to have higher nerve targeting at the 15 min ($t(4) = 3.2$, $p = 0.03$) and 30 min ($t(4) = 3.6$, $p = 0.02$) timepoints on the Buccal nerve (**Figure 8 I**) and at the 60 min timepoint ($t(4) = 5.9$, $p = 0.004$) on the Marginal nerve (**Figure 8 J**) post topical application.

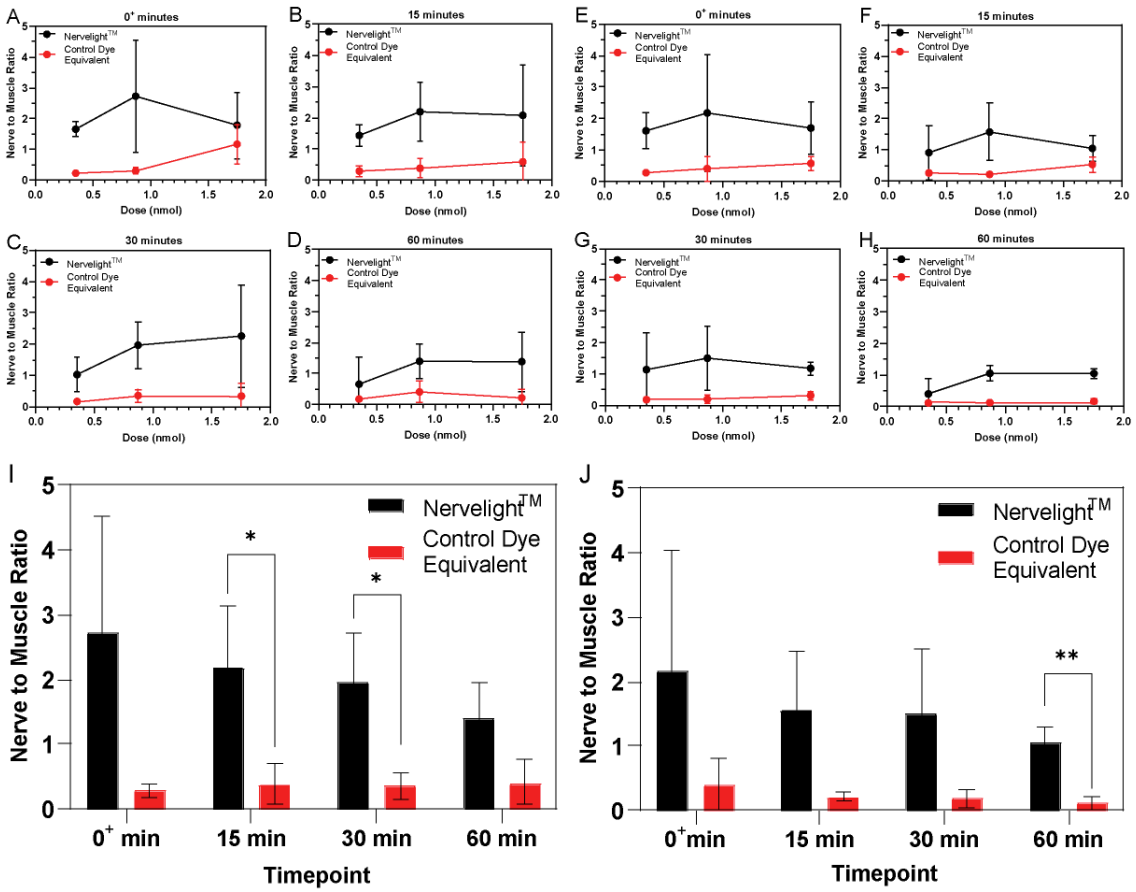

Figure 8. Dose response curves of the Buccal and Marginal nerves at each dose and timepoint in the form of SBR values **(A-D)** Buccal nerve branch, **(E-H)** Marginal nerve branch at 0+ minutes, 15 minutes, 30 minutes, and 60 minutes dosed with Nervelight™ and control dye equivalent. Time-dependency of 0.87 nmol intermediate dose, Buccal (**I**) and Marginal (**J**). *p < 0.05, **p < 0.01.

Determination of nerve fluorescent intensity signal

The nerve branches, muscle tissue, parotid gland, contralateral nerve, and clearance organs were excised for determination of fluorescence signal intensity. The fluorescent images were acquired under the LICOR Pearl imaging system, where the intensity signal was calculated for each organ. Relatively high signal intensity of Nervelight™ was seen in the buccal and marginal nerves. **Figure 9** presents the calculated SNR values of the nerves, surrounding tissue, and clearance organs. The facial nerve can interact with the parotid gland depending on the nerve orientation; therefore, signal was seen in the parotid gland at all Nervelight™ doses. The 0.35 nmol dose SNR

did not show any significant difference in values between the Nervelight™ and unmodified dye groups (**Figure 9 A**). Within the 0.87 and 1.75 nmol doses, both had higher nerve signal intensity values in the Nervelight™ group compared to the unmodified control NIR dye group. Nervelight™ was observed to have a stronger statistical significance of nerve fluorescent signal intensity in comparison to the unmodified NIR control dye within the buccal nerve at the 0.87 nmol dose ($t(4) = 5.7$, $p = 0.004$)) as well as in the 1.75 nmol dose for both the buccal nerve ($t(4) = 13.3$, $p = 0.0002$) and marginal nerve ($t(4) = 2.9$, $p = 0.04$) (**Figures 9 C-E**). This could suggest higher interaction at the nerve sites within the 0.87 and 1.75 nmol doses with Nervelight™.

Figures 9 B, D and F provide SNR values of the excised clearance organs. The kidney and spleen were observed to have a higher SNR value in all three dose groups. These elevated signals support that the clearance mechanism of Nervelight™ and NIR control dye is suggested through the kidney and spleen. The heart and lungs were excised to provide details about potential non-binding of the contrast agents and low SNR values were observed in these organs. To assess biodistribution of the fluorescent conjugates all organs were imaged at 60 minutes post topical application on the LI-COR Pearl (**Figure 10**). SNR values were quantified from the biodistribution images by drawing regions of interest around each organ tissue.

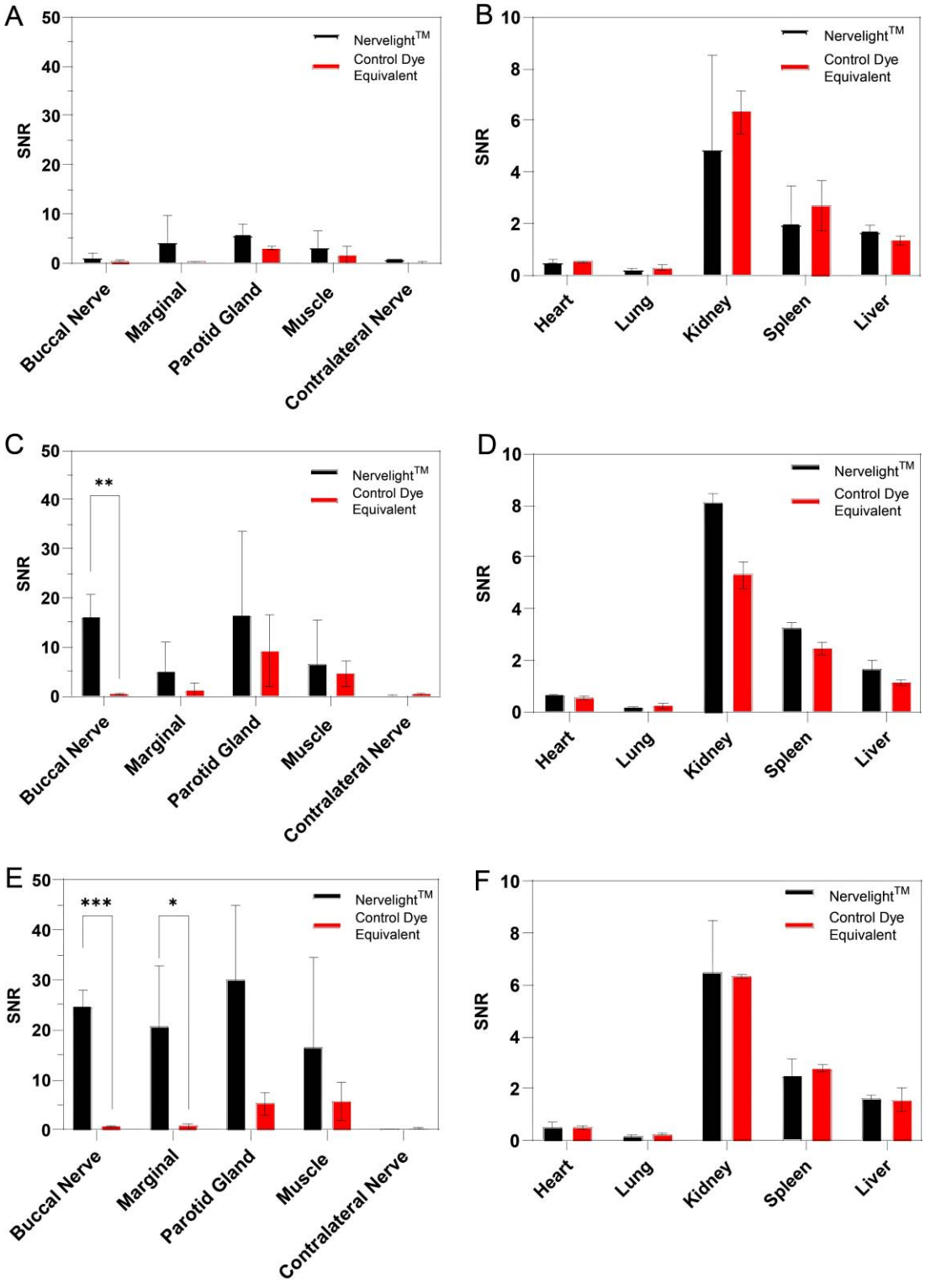

Figure 9. SNR of nerves, surrounding tissue, and clearance organs of Nervelight™ and NIR control dye. **(A-B)** 0.35 nmol dose **(C-D)** 0.87 nmol dose, **(E-F)** 1.75 nmol dose. *P < 0.05, **P < 0.01, ***P < 0.0001.

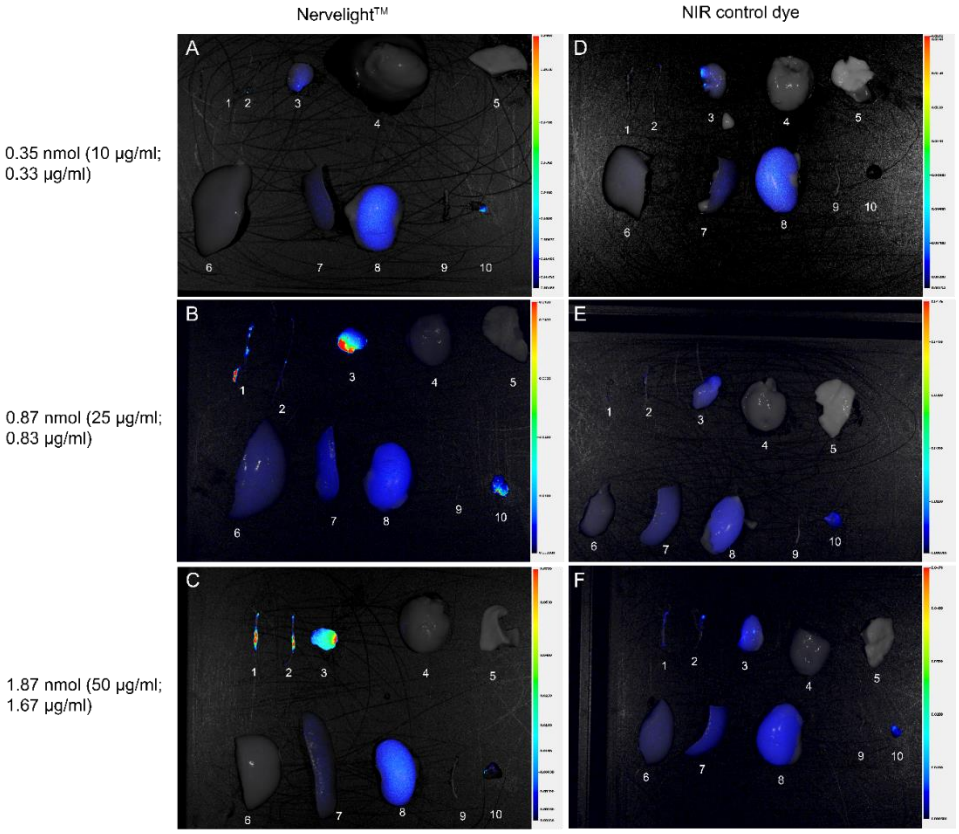

Figure 10. Representative biodistribution of Nervelight™ and unmodified NIR control dye excised organs. 1= Buccal nerve, 2= Marginal nerve, 3= parotid gland, 4= heart, 5= lung, 6= liver, 7= spleen, 8= kidney, 9= contralateral nerve, 10= muscle.

Fluorescence and histological analysis of nerve sections

Nerve sections were analyzed under the Olympus fluorescent microscope for confirmation of NIR signal. Sectioning of the nerve provides that the Nervelight™ contrast agent has the ability to target the nerve. **Figure 11** shows histological analysis of the facial nerve sections. Determination of co-occurrence between the NIR and TrkA antibody would suggest targeting of the contrast agent to nerve tissue. Standard H&E staining of the facial nerve (**Figure 11 A-B**) allows the structure of the nerve to be seen. After further examination of the facial nerve section, TrkA primary antibody was seen to co-occur with the Nervelight™ NIR signal. **Figure 11 C-D** show darker brown staining corresponding to the TrkA receptors and NIR staining (**Figure 11 E**). Autofluorescence and NIR merged signal of the facial nerve (**Figure 11 E-F**), the autofluorescence

highlights the entirety of the nerve sample, while the NIR signal provides the localization of the Nervelight™ on the nerve, shown as the strong magenta coloring. **Figure 11 D** provided dark brown staining due to the TrkA receptors but does not co-occur with the NIR signal in **Figure 11 F**, indicating the NIR signal of the unmodified control dye does not preferential bind to the nerve.

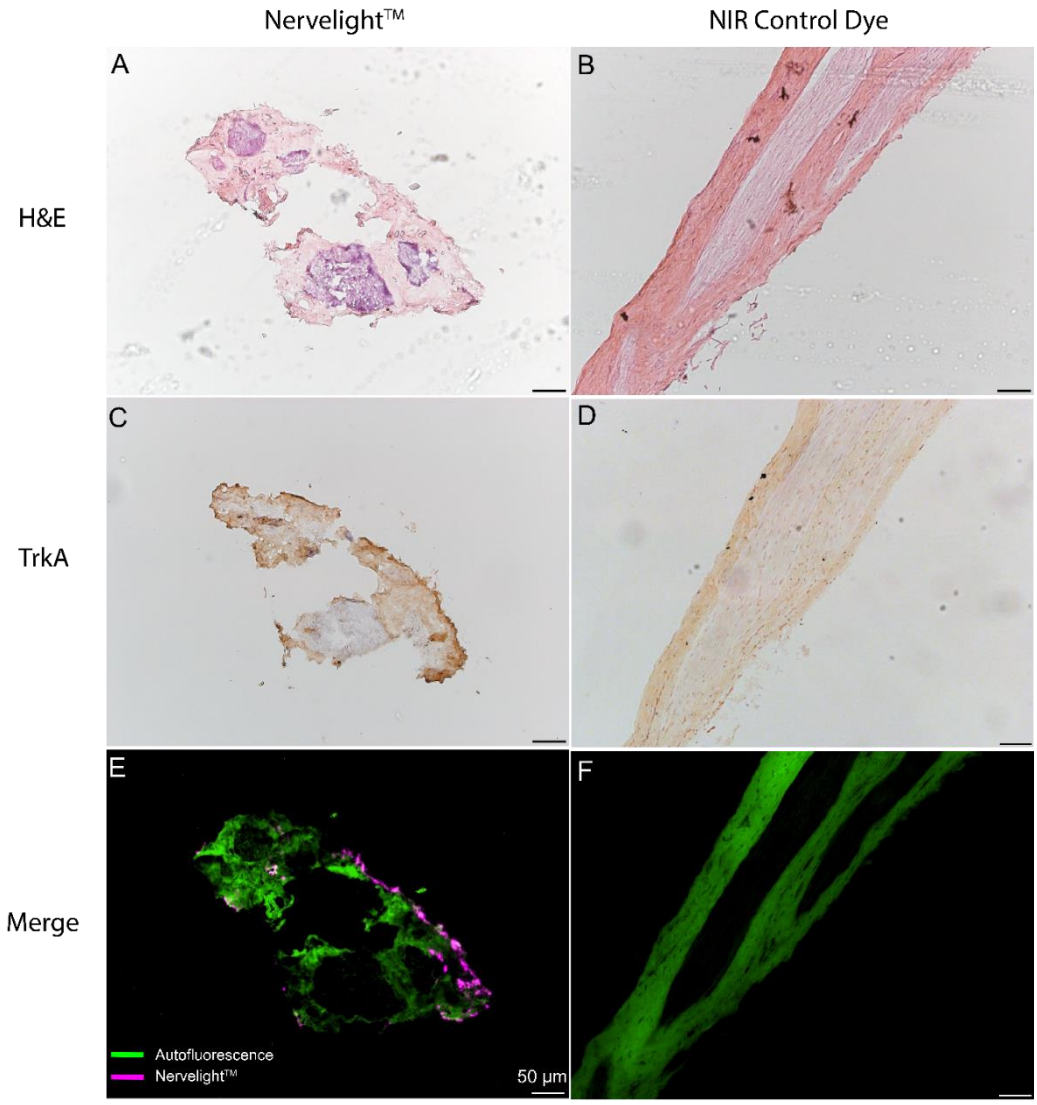

Figure 11 1.75 nmol Buccal Nerve Histology: **(A)** Nervelight™ cross section and **(B)** equivalent control dye longitudinal section Hematoxylin and Eosin (H&E) stain, **(C-D)** TrkA antibody staining (darker brown stain along the edge of the nerve), and **(E-F)** autofluorescence (green) and Nervelight™ (magenta) merged image. Scale bar is 50 µm.

Discussion

Nerve damage is a well-known risk of surgical interventions, during which surgeons may not be aware of nerve presence due to variability in anatomy, among other factors[4]. This damage can result in pain, loss of nerve function, and reduction of normal bodily functions for the patients. Nerves can be found in many different orientations, especially when a tumor is present, in addition to being obscured by other tissue, forcing surgeons to rely on their anatomy knowledge. Nerve sparing techniques have been used for many years[32-35], but patients remain exposed to high risk of nerve damage, loss of function, or pain following surgery. Therefore, the most crucial tissues to locate during surgery are the nerve branches that play pivotal roles in facial expression, function, and movement. Highlighting nerve branches during surgical interventions can aid surgeons with tools to reduce the risk of nerve damage. The use of FGS techniques is a strategy that can aid surgeons in preventing nerve damage during surgical interventions[4, 22, 36]. Development of tissue specific NIR contrast agents for use in image guided surgery could enable higher targeting to fluoresce the nerve of interest. Tissue selective contrast agents can target tumor tissue for resection and allow normal tissue, particularly highly valuable tissue such as nerves, to be avoided during surgery. These techniques give surgeons another tool to complement their training, skill, and anatomical expertise.

The goal of a nerve specific contrast agent is to enable at-risk nerves to be labeled for surgeons to improve visualization and identification during surgery[4]. These contrast agents would be beneficial for labeling surface and buried nerves. The importance of visualizing both surface and buried nerves can be explained by the facial nerve. The facial nerve trunk begins in the cranial area and expands towards the face, passing through the parotid gland[24, 37], before splitting into 5 branches, each with important sensory and motor function. In the case of the facial nerve and surgeries such as parotidectomies, to preserve all of these functions it is crucial to label all nerve tissue that may intersect with facial tissue.

Nervelight™ is a potential solution to reduce nerve damage and minimize the risk of pain and loss of nerve function in a patient. As a nerve specific contrast agent, labeling of nerves would provide less risk for patients during and following surgery. Extensive research has been examined to highlight nerves during radical prostatectomies[9, 32, 38-41], in which the nerves surrounding the bladder and prostate are labeled resulting in nerve sparing. The knowledge gained through these studies laid the groundwork to develop nerve specific contrast agents with low toxicity. Examining the ability of a nerve specific agent to successfully target facial nerve branches would enable the use of that agent in head and neck surgeries to spare these nerves in a similar way as seen with prostatectomies. The literature provided some studies that highlighted the facial nerve through intravenous injection, which enables binding within a few hours, but also carried the risk of not reaching the nerve site[10, 23, 42]. Direct administration would ensure that the agent reaches a specific target site and enables the integration of the agent into the surgery[41].

Herein, we show after the direct administration method, the Buccal and Marginal nerve branches are successfully highlighted but Nervelight™ in comparison to the unmodified NIR control dye. Similarities in human and rat facial nerve anatomies allow for a rat model to be utilized for preliminary dose studies (**Figure 4**). The visualization of both nerve branches following a preauricular incision method enables a clinically relevant surgical method for the head and neck region. The development of a NIR dye-conjugated recombinant nerve growth factor protein, Nervelight™ provides targeting to nerve sites. The NIR contrast agent and the direct topical application method provides robust visualization of the facial nerve branches to aid surgeons with a new tool. By confirming fluorescent intensity of NIR dye attachment to the protein, the contrast agent can be topically applied to the target site for specific targeting.

In vivo work confirmed fluorescent targeting to the Buccal and Marginal nerves while lower signal was observed in the surrounding muscle tissue (**Figure 7**). Once the nerves were excised, the SNR analysis shows the fluorescent intensity capability of Nervelight™ on the nerves, surrounding muscle and clearance organs, in which the higher fluorescent intensity is present on

the nerves at the 0.87 and 1.75 nmol doses (**Figure 9**). The NIR control dye equivalent was observed to have lower signal in the nerve sites with higher signal in the muscle tissue. By analyzing NIR images, Nervelight™ was found to be dose-independent and time-independent in the facial nerve area (**Figure 8**). Within the intermediate dose (0.87 nmol of dye), Nervelight™ indicated a significant difference of nerve fluorescent intensity in the Buccal nerve at 15 and 30 min and Marginal nerve at 60 min post topical application. After further analysis of the nerve sections, Nervelight™ NIR signal was observed co-occur with the TrkA (**Figure 11**). Co-occurrence of the TrkA receptors and the NIR signal suggests evidence that this nerve specific agent can interact with nerve receptors, thus providing labeling of nerves. This study indicates that a developed nerve specific fluorescent agent can provide high fluorescent contrast at nerve sites via topical administration aiding surgeons with a much-needed surgical tool to help reduce the risk of nerve damage.

Conclusions

Nerve specific contrast agents combined with image-guided surgery techniques provides a step towards limiting nerve damage during surgical procedures. The surgeon's enhanced ability to effectively maneuver surgical tools around at-risk nerve sites would allow for the quality of life of patients to be preserved after surgeries. This fluorescent contrast agent, Nervelight™ was observed to specifically target facial nerve areas improving visualization during surgery. Nervelight™ provides a solution to the clinical need to reduce potential risk of nerve damage during surgical operations.

Bibliography

1. Bailar, J. C.; Gornik, H. L., Cancer Undefeated. *N. Engl. J. Med.* **1997**, *336* (22), 1569-1574.

2. Institute, N. C. Head and Neck Cancers. *US Departmentof Health and Human Services* [Online]. **2021**.

3. Paddock, M. What to Know About Salivary Gland Cancer *Medline News Today* [Online]. **2021**.

4. Gibbs, S. L., Near Infrared Fluorescence for Image-Guided Surgery. *Quant. Imaging Med. Surg.* **2012**, *2* (3), 177.

5. Burke, S., & Shorten, G. D., When Pain after Surgery Doesn't Go Away. *Biochem. Soc. Trans.* **2009**, 318-322.

6. Marien, T. P.; Lepor, H., Does a Nerve-Sparing Technique or Potency Affect Continence After Open Radical Retropubic Prostatectomy? *BJU Int.* **2008**, *102* (11), 1581-1584.

7. Michaelson, M. D.; Cotter, S. E.; Gargollo, P. C., et al., Management of Complications of Prostate Cancer Treatment. *CA: Cancer J. Clin.* **2008**, *58* (4), 196-213.

8. Penson, D. F.; McLerran, D.; Feng, Z., et al., 5-Year Urinary and Sexual Outcomes after Radical Prostatectomy: Results from the Prostate Cancer Outcomes Study. *J. Urol.* **2005**, *173* (5), 1701-1705.

9. Walz, J.; Graefen, M.; Huland, H., Basic Principles of Anatomy for Optimal Surgical Treatment of Prostate Cancer. *World J. Urol.* **2007**, *25* (1), 31-38.

10. Gonzales, J.; Pirovano, G.; Chow, C. Y., et al., Fluorescence Labeling of a Na V 1.7-Targeted Peptide for near-Infrared Nerve Visualization. *EJNMMI Res.* **2020**, *10* (1), 1-8.

11. Chen, Y.; Zhang, H.; Lei, Z., et al., Recent Advances in Intraoperative Nerve Bioimaging: Fluorescence-Guided Surgery for Nerve Preservation. *Small Struct.* **2020**, *1* (1), 2000036.

12. Carpenter, J. S.; Sloan, P.; Andrykowski, M. A., et al., Risk Factors for Pain after Mastectomy/Lumpectomy. *Cancer Pract.* **1999**, *7* (2), 66-70.

13. Macdonald, L.; Bruce, J.; Scott, N. W., et al., Long-Term Follow-up of Breast Cancer Survivors with Post-Mastectomy Pain Syndrome. *Brit. J. Cancer.* **2005**, *92* (2), 225-230.

14. Poleshuck, E. L.; Katz, J.; Andrus, C. H., et al., Risk Factors for Chronic Pain Following Breast Cancer Surgery: A Prospective Study. *J. Pain.* **2006**, *7* (9), 626-634.

15. Cotero, V. E.; Siclovan, T.; Zhang, R., et al., Intraoperative Fluorescence Imaging of Peripheral and Central Nerves through a Myelin-Selective Contrast Agent. *Mol. Imaging Biol.* **2012**, *14* (6), 708-717.

16. Wallner, C.; Lange, M. M.; Bonsing, B. A., et al., Causes of Fecal and Urinary Incontinence after Total Mesorectal Excision for Rectal Cancer Based on Cadaveric Surgery: A Study from the Cooperative Clinical Investigators of the Dutch Total Mesorectal Excision Trial. *J. Clin. Oncol.* **2008**, *26* (27), 4466-4472.

17. Gibbs-Strauss, S. L.; Nasr, K. A.; Fish, K. M., et al., Nerve-Highlighting Fluorescent Contrast Agents for Image-Guided Surgery. *Mol. Imaging.* **2011**, *10* (2), 7290.2010. 00026.

18. Gordin, E.; Lee, T. S.; Ducic, Y., et al., Facial Nerve Trauma: Evaluation and Considerations in Management. *Craniomaxillofac. Trauma Reconstruct.* **2015**, *8* (1), 1-13.

19. Varaldo, E.; Ansaldo, G. L.; Mascherini, M., et al., Neurological Complications in Thyroid Surgery: A Surgical Point of View on Laryngeal Nerves. *Front. Endocrinol.* **2014**, *5*, 108.

20. Echternach, M.; Maurer, C.; Mencke, T., et al., Laryngeal Complications after Thyroidectomy: Is It Always the Surgeon? *Arch. Surg.* **2009**, *144* (2), 149-153.

21. Sosa, J. A.; Bowman, H. M.; Tielsch, J. M., et al., The Importance of Surgeon Experience for Clinical and Economic Outcomes from Thyroidectomy. *Ann. Surg.* **1998**, *228* (3), 320.

22. Walsh, E. M.; Cole, D.; Tipirneni, K. E., et al., Fluorescence Imaging of Nerves During Surgery. *Ann. Surg.* **2019**, *270* (1), 69-76.

23. Hussain, T.; Mastrodimos, M. B.; Raju, S. C., et al., Fluorescently Labeled Peptide Increases Identification of Degenerated Facial Nerve Branches During Surgery and Improves Functional Outcome. *PloS One.* **2015**, *10* (3), e0119600.

24. Al-Zwaini, I. J.; Hussein, M. J., Introductory Chapter: Facial Nerve-an Overview. *Selected Topics in Facial Nerve Disorders.* **2019**.

25. Sun, F.; Zhou, K.; Mi, W.-j., et al., Combined Use of Decellularized Allogeneic Artery Conduits with Autologous Transdifferentiated Adipose-Derived Stem Cells for Facial Nerve Regeneration in Rats. *Biomaterials.* **2011**, *32* (32), 8118-8128.

26. Borsook, D.; Kussman, B. D.; George, E., et al., Surgically-Induced Neuropathic Pain (Snpp): Understanding the Perioperative Process. *Ann. Surg.* **2013**, *257* (3), 403.

27. Kehlet, H.; Jensen, T. S.; Woolf, C. J., Persistent Postsurgical Pain: Risk Factors and Prevention. *Lancet.* **2006**, *367* (9522), 1618-1625.

28. Mok, S. A.; Campenot, R. B., A Nerve Growth Factor-Induced Retrograde Survival Signal Mediated by Mechanisms Downstream of Trka. *Neuropharmacol.* **2007**, *52* (2), 270-278.

29. Neet, K.; Campenot, R., Receptor Binding, Internalization, and Retrograde Transport of Neurotrophic Factors. *Cell. Mol. Life Sci. CMLS* **2001**, *58* (8), 1021-1035.

30. Lykissas, M. G.; Batistatou, A. K.; Charalabopoulos, K. A., et al., The Role of Neurotrophins in Axonal Growth, Guidance, and Regeneration. *Curr. Neurovasc. Res.* **2007**, *4* (2), 143-151.

31. Hill, T. K.; Abdulahad, A.; Kelkar, S. S., et al., Indocyanine Green-Loaded Nanoparticles for Image-Guided Tumor Surgery. *Bioconjug. Chem.* **2015**, *26* (2), 294-303.

32. Tewari, A.; Peabody, J. O.; Fischer, M., et al., An Operative and Anatomic Study to Help in Nerve Sparing During Laparoscopic and Robotic Radical Prostatectomy. *Eur. Urol.* **2003**, *43* (5), 444-454.

33. Walsh, P. C.; Lepor, H.; Eggleston, J. C., Radical Prostatectomy with Preservation of Sexual Function: Anatomical and Pathological Considerations. *Prostate.* **1983**, *4* (5), 473-485.

34. Walsh, P.; Mostwin, J., Radical Prostatectomy and Cystoprostatectomy with Preservation of Potency. Results Using a New Nerve-Sparing Technique. *Brit. J. Urol.* **1984**, *56* (6), 694-697.

35. Stenzl, A.; Colleselli, K.; Poisel, S., et al., Rationale and Technique of Nerve Sparing Radical Cystectomy before an Orthotopic Neobladder Procedure in Women. *J. Urol.* **1995**, *154* (6), 2044-2049.

36. Olson, M. T.; Ly, Q. P.; Mohs, A. M., Fluorescence Guidance in Surgical Oncology: Challenges, Opportunities, and Translation. *Mol. Imaging Biol.* **2019**, *21* (2), 200-218.

37. Ronald Bergman, A. K. A., & Ryosuke Miyauchi Variations in Branching of Facial Nerve. anatomyatlases.org/AnatomicVariants/NervousSystem/Images/20.shtml.

38. Walsh, P. C.; Donker, P. J., Impotence Following Radical Prostatectomy: Insight into Etiology and Prevention. *J. Urol.* **1982**, *128* (3), 492-497.

39. Damber, J.-E.; Khatami, A., Surgical Treatment of Localized Prostate Cancer. *Acta Oncol.* **2005**, *44* (6), 599-604.

40. Hingorani, D. V.; Whitney, M. A.; Friedman, B., et al., Nerve-Targeted Probes for Fluorescence-Guided Intraoperative Imaging. *Theranostics.* **2018**, *8* (15), 4226.

41. Barth, C. W.; Gibbs, S. L., Direct Administration of Nerve-Specific Contrast to Improve Nerve Sparing Radical Prostatectomy. *Theranostics* **2017**, *7* (3), 573.

42. Hussain, T.; Nguyen, L. T.; Whitney, M., et al., Improved Facial Nerve Identification During Parotidectomy with Fluorescently Labeled Peptide. *Laryngoscope.* **2016**, *126* (12), 2711-2717.

CHAPTER 4: NANOMATERIALS AND NANOTECHNOLOGY

Nanotechnology has contributed to the clinical improvement of therapeutic delivery, detection, and treatment of diseases and can be defined as technology designed at the nanoscale level[1]. Typically, nanomaterials are classified as having a small size, usually less than a few hundred nanometers[2]. Nanomaterials can be categorized into organic, inorganic, or hybrid-based materials with each group possessing their own advantages[3]. The categories of nanomaterials incorporate chemical, physical, and biological properties that enable these materials to be used as platforms for many different applications. Utilization of the unique properties that nanomaterials possess can exploit key advantages of the controlled design and synthesis. Nanomaterials have an increased surface area to volume ratio, allowing for their surfaces to be used as binding entities due to reactive functional groups leading to improved specificity for detection or targeting[4, 5]. The presence of unique properties and small, controlled size gives nanotechnology distinct improvements over the bulk counterparts for use in research.

Nanomaterials can be synthesized in various ways, but each synthesis is dependent on the material and intended final product. There are two general strategies for synthesizing nanomaterials: a top-down or a bottom-up approach[6-8] (**Figure 12**). Ultimately, many factors can influence the strategy used, including the material makeup and consideration of the intended application purpose, for which the size, shape, and surface functionalization are all critical. The first general approach is the top-down approach which involves a bulk material being reduced in size to form nanoparticles[9-12]. This approach breaks down a selected bulk material into smaller parts and methods include mechanical milling[10, 11, 13, 14], laser ablation[10, 15-19], and sputtering[7, 10, 20-23]. Mechanical milling involves griding of a bulk material into smaller particles and is a common method when nanomaterials are needed across a broad range in size and where the size distribution of the particles can be less consistent; nanocomposites are one example of a mechanically milled nanoparticle[7, 24]. This method of nanoparticle synthesis is unsuitable for

applications requiring a specific size and uniform shape of nanomaterials. Laser ablation is another method to produce nanomaterials using high-energy waves of laser light to create material fragments from a solid bulk material[17-19]. The small particles that form after the laser process come together to form the desired nanomaterial which has properties that result from specific laser parameters, including wavelength, repetition rate, and pulse energy[16]. The sputtering method involves using high energy directed at the solid bulk material to form particles within a chamber[7, 20, 21]. Nanofilms are commonly formed by this method[25]. In this method, high energy is applied to a solid sample; the particles produced may be almost identical to the bulk material but smaller, which may be beneficial when the bulk material properties are desired. The top-down approach can be utilized to create many nanomaterials from solid bulk material and specifically tailored nanomaterials by changing the methods used to break apart the bulk sample.

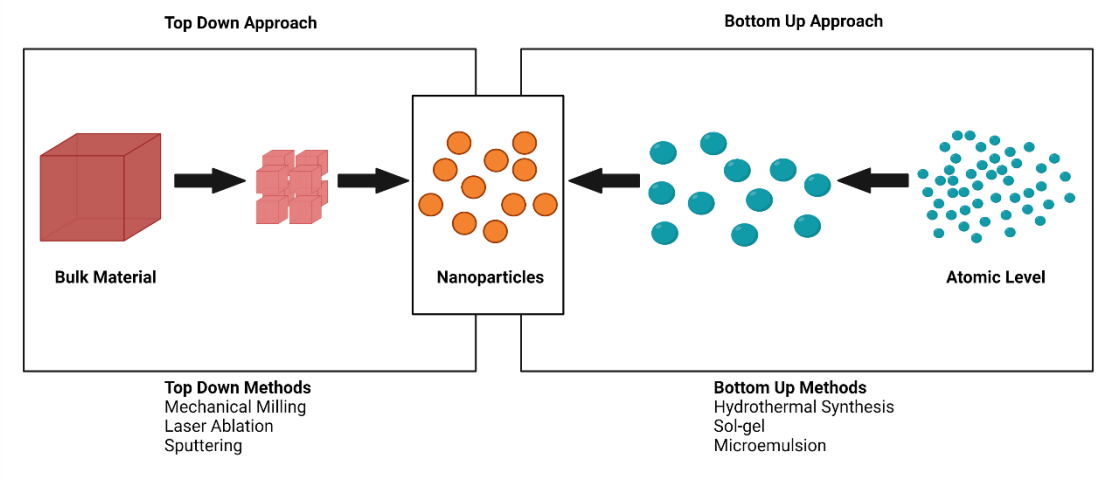

Figure 12. Top-Down and Bottom-Up approaches to synthesizing nanomaterials. Created using biorender.com.

The second general approach for nanomaterial synthesis is the bottom-up approach, which entails starting at the atomic level and generating nanomaterials using chemical reactions with atoms or precursor molecules to form nanomaterials. A few common methods include microemulsion[26-31], colloidal[32], hydrothermal synthesis[7, 11, 33-35], sol-gel[7, 11, 33], and biologically synthesis[36, 37]. Microemulsion synthesis is a common method to produce nanomaterials by

bringing together two immiscible liquids, such as oil and water, into a single phase that is stabilized by a co-surfactant[26-28 30, 31]. This type of nanomaterial synthesis forms stable, spherical aggregates and can be widely utilized in nanotechnology applications. Liposomes, polymeric micelles, and nanocapsules can be formulated and synthesized through microemulsion techniques[38, 39]. Colloidal synthesis methods of preparing metal nanomaterials are characterized by reducing complexes in a dilute solution to create a supersaturated solution of atoms that nucleate and form nanoparticles[40]. Parameters can be controlled to create tailored shape, size, and growth of the nanoparticles, providing potential benefits. Hydrothermal synthesis is another commonly used method to produce nanomaterials by heating a solution to high temperatures before cooling down the solution. A higher order of structured elemental atom composition from the precursor materials can be produced within the nanoparticles. The sol-gel method of nanomaterial production is done by the process utilizing a solution of metal or carbon-based precursors that crosslink to form a gel. A typical representation of a sol-gel is the processing of metal oxide nanoparticles through hydrolysis and condensation reactions, which results in crosslinking, producing strong bonds. The size and morphology can be tailored by changing different parameters within the reaction, including the pH[4, 41, 42]. This process can be represented as a simple two-step process of hydrolysis and condensation reactions to form tailored nanoparticles. Another example of a bottom-up approach method is the process of biological synthesis to produce nanomaterials. This process requires the use of biological entities (bacteria, fungi, plants, and yeasts)[36]. Biological entities can be a potential solution for bypassing the need for harsh chemicals, high temperatures, or time-consuming reactions, and these entities can perform synthesis through intracellular or extracellular mechanisms[37]. Depending on the intended application, avoiding harsh chemical and physical may be desirable or even necessary, making biological synthesis the most appealing option. Both approaches (Top-down and Bottom-up) consist of various methods that can be used to produce a wide array of useful nanomaterials.

The variety of methods to produce nanomaterials has led to an extensive list of nanomaterials used in research. Categories of these nanomaterials used include inorganic, organic, and composite-based nanomaterials[3, 43]. Each type of nanomaterial has distinct advantages for use in specific applications but can also carry disadvantages which are largely due to the reaction conditions. Inorganic-based nanomaterials can be made from metals, metal oxides, and quantum dots[44]. Inorganic-based materials have unique properties with great versatility that researchers have been interested in for their usage in biomedical applications. The optical and magnetic physical properties, along with the stability and ease of functionalization via chemical properties, provide a variety of advantages[45]. Inorganic-based nanomaterials are a great option for biomedical applications due to surface modification feasibility and physiochemical properties. A few common examples of inorganic materials used to produce a nanomaterial scaffold are metals such as gold[44-48] and silver[45, 47], and other materials including silica[44, 47, 49]. Organic-based nanomaterials are materials that mainly consist of organic compounds with some form of carbon as the main element, such as carbohydrates, lipids, and polymers. These organic nanomaterials have strong stability and the ability to control certain parameters, such as higher colloidal stability, size, and surface properties, which are great advantages for the production of nanomaterials[45, 47, 50, 51]. The incorporation of nanotechnology comprised of organic materials can allow for higher biocompatibility in the biological environment. Carbon-based nanomaterials, including nanodots, fullerenes, and carbon tubes, are common organic-based nanomaterials[52-55]. Combining two or more inorganic and organic-based materials allows for a hybrid or composite nanomaterials. These nanocomposite materials can encompass the advantageous properties of both organic and inorganic materials present[47, 56-58]. The components of these hybrid nanomaterials can be structured to create very complex entities for use in nanotechnology applications. This variety of materials that can be used enables the creation of a wide array of nanotechnology platforms.

The newly designed nanotechnology platforms can be utilized in imaging or delivery applications which are key areas at the forefront of nanotechnology development. The delivery of drugs, proteins, and other small molecules has played an essential role in the detection and treatment strategies of diseases currently being studied and those that will be studied in the future. Nanotechnology can allow for improved delivery of poorly soluble drugs, targeting of tissue-specific delivery of drugs, co-delivery of multiple drugs, bioavailability, sustained delivery at a target site, and therapeutic effect[59-63]. A disease may require only one specific drug delivery mechanism or specific region for a therapeutic effect or treatment to occur. Nanotechnology can help overcome the challenges presented in drug delivery systems. Drug delivery can be defined as the process of administering a compound to achieve a therapeutic effect and may be achieved through several different routes[64]. Nanotechnology-based delivery systems help overcome the challenges of conventional delivery systems and their associated interactions with the biological environment as well as the challenges of targeted delivery to the intended cell. Targeted drug delivery ensures that the drug interacts only with the intended target, while untargeted delivery exposes all cells to the potentially harmful effects of a drug[65]. Unintended drug delivery to healthy cells can produce unwanted consequences and may result in diseased sites. Targeted drug delivery systems can circulate for a prolonged time and release the drug cargo at a specific time and location, increasing the therapeutic benefit at the intended region while minimizing the risk to healthy cells. Various nanotechnologies can be utilized as drug delivery vehicles, including liposomes[66-69], micelles[70-73], dendrimers[74-79], and nanoparticle formulations[63, 80-85]. Ultimately, some factors determine the effectiveness of a nanotechnology-driven drug delivery system such as the advantages and disadvantages of the delivery system platform, evaluating the fate of the drug after release, and assessing the effect of the unreleased drug. Along with usage as drug delivery carriers, nanotechnology-based systems have the potential for use as imaging systems.

Incorporating nanomaterial-based platforms for imaging applications in the clinic could improve the detection of diseases. Improvements in detection would then positively impact the diagnosis and treatment of these diseases, improving the quality of life for patients. Fluorescent imaging techniques are non-invasive tools that would allow clinicians to observe, document, and analyze physiological or pathophysiological changes. When compared to existing technologies used in the clinic, these techniques are characterized by high sensitivity, being less-invasive, enabling safer detection, and allowing for probe manipulation or targeting[86]. The modification for selectivity and improved targeting would enable these different fluorescent probes to be tailored to a specific disease or region in the body for enhanced visualization. Successful nanomaterial-based systems could potentially be used to detect and visualize many different diseases by simply manipulating surface attachments. For instance, different cancers and diseases have an upregulation of different receptors which could be used as targeting sites for surface ligand attachment[87].

Imaging applications with nanomaterial-based platforms have steadily increased as visualization methods in the clinic, especially in the removal of cancer tumors[88-90] and the avoidance of vital structures[91] during surgical operations. A variety of fluorescent nanomaterials have already been designed for targeting cancer tumors[88, 92-97]. In addition to simply visualizing cancer tumors, nanotechnologies can be further advanced by combining visualization and delivery approaches. The ability to have a fluorescent nanomaterial system and a therapeutic agent incorporated for controlled release may increase the number of clinical applications for nanomaterials[98]. These types of nanomaterial-based fluorescent platform advancements could allow for a dual nanotechnology system to be designed, which could provide both the detection and treatment of a disease.

As nanotechnology is incorporated into various clinical areas, challenges may arise in the design and development of nanomaterial-based systems. Novel therapeutics or imaging agents

undergo extensive testing and validation before approval and usage in the clinic. Challenges will arise along the testing and development process of any therapeutics and imaging agents, including nanotechnology-based systems. These challenges include fluorescent quenching of fluorophores, reaction conditions or the types of materials, and specific tissue targeting.

For imaging agents, fluorophores can inadvertently be quenched, and the fluorescent signal can be lost or significantly reduced by various processes such as excited state reactions, energy transfer, complex formation, and collisional quenching[99]. Therefore, these different processes can affect the fluorescent quantum yield of fluorescent nanotechnology. Aggregation can play a significant role in how fluorescent molecules interact with one another, leading to a weakened fluorescence. Aggregation-Caused Quenching (ACQ) is a phenomenon that occurs when dye molecules in highly concentrated solutions or in the proximity of one another reduce or weaken the fluorescent signal. On the other hand, in diluted solutions, due to high efficiency, fluorescent molecules can emit light [100-106]. A key concept for the development of nanotechnologies as imaging platforms, determining the appropriate concentration of the fluorescent fluorophores is crucial to allow for the dye molecules to emit light at the highest efficiency without the risk of quenching. The phenomenon of Aggregation-Induced Emission (AIE) has been achieved and allows for the fluorescent intensity of organic fluorescent molecules in a solid state[102, 107]. With the emergence of certain organic fluorophores that can emit a high intensity of fluorescence while aggregated, aggregation may provide a solution for quenching at specific concentrations. Nonetheless, the research of AIE dye molecules will need to undergo extensive development for use with fluorescent probes in the generation of nanotechnology-based platforms.

Controlling different nanomaterial properties, such as size, can influence the behavior and performance of a nanomaterial-based system in biomedical applications. Specific properties may be required for the function of a nanotechnology-based platform to provide the intended

benefit or function. In many cases, the nanotechnology size plays a critical role in the delivery to the target site. Size-controlled design and development of functional materials allow for advantages over bulk materials[108-113]. The ability to control and tailor different parameters of nanomaterials, especially the size, to specific properties allows for the engineering of materials specific to biomedical applications. The size of nanoparticles is a critical area of design of deliverables as cell receptors and channels present throughout the body have size restrictions that determine what can enter the cell. Nanomaterials for use in bioimaging applications can have specific sizes at which they reach their optimal emission properties and provide the highest signal to be attained[108, 114, 115]. Tuning size-dependent nanomaterials to offer the highest emission properties at the nanometer scale is groundbreaking, particularly when considering those properties are critical in determining whether the nanomaterial successfully enters cells. Although size-dependent properties are a vitally important aspect for nanomaterials, targeting at the intended site is another critical factor to consider in designing and developing these platforms.

Specifically targeting regions of cells or tissue requires the use of cell receptors or ligand attachment. Surface modifications enable nanotechnology and delivery vehicles to interact with the biological environment and function at the region of interest. Different surface modifications can improve the ability of the imaging and delivery agents to overcome biological barriers[116-118]. Various nanomaterials are engineered for an intended therapeutic purpose through specific functioning at the surface. Surface attachment of ligands that bind to certain cell surface receptors, addition of biocompatible materials as a surface coating, and responsive stimuli for drug release are commonly used for nanomaterials to reach the intended site and release the drug for a therapeutic or imaging purpose. The engineering of the nanomaterial surface helps overcome the challenges of other nanotherapeutics by determining the appropriate modifications that result in the most effective targeted delivery[116, 119, 120]. The development and design of nanotechnologies may depend on the disease type and patient, both of which can vary widely.

The success of nanoparticle drug delivery lies in reaching the intracellular space and delivering the entrapped cargo to the intended target site. Diagnosis, detection, and treatment of diseases can be improved by the localized delivery and targeting of nanotechnologies. For instance, many diseases, such as cancer, have an upregulation of cell surface receptors that are available for targeting. The upregulation of receptors on cancer cells gives rise to localized regions that can be identified for targeting by nanoparticles. Once identified, nanotechnology can perform its imaging or therapeutic function. Surface targeting ligands can be of potential use in actively targeting specific cells or tissue through biomarkers. Through various surface ligands, such as CD44[121-127], CD31[128-130], and EGFR[131-137], the binding of nanomaterials to a target region on a cell surface can be increased. Once bound to the target site of a cell, a nanotechnology system can deliver the cargo for its intended use.

The fate of nanoparticles relies on the ability to be internalized into the intracellular spaces of the biological environment. Developing efficient and safe nanomaterial-based nanotechnologies is possible through optimizing the physiochemical properties of the nanomaterial for the intended application[138-142]. The properties of nanoparticles ultimately play a role in overcoming various biological barriers to reaching the target site. Size, shape, pH, and surface charge are all common physiochemical factors that are critical in nanotechnology design that enable nanoparticle identification and shape interactions with the biological environments[138, 143-146]. After reaching the cellular membrane, nanoparticles need to be internalized into the cell to continue their journey, and various factors play a role on the nanoparticle mechanism of internalization. These factors can include the physiochemical properties of the nanoparticles, the presence of proteins or biomolecules involved in the process, and targeted cell type. The different mechanisms of endocytosis include phagocytosis, clathrin-mediated, caveolin mediated, clathrin/caveolae independent mediated, and micropinocytosis[138]. Each of the uptake mechanisms has specific parameters that control entry into a cell. Nanoparticles conjugated with ligands or

biomolecules on the surface are commonly internalized through the clathrin/caveolae-independent mechanism or surface receptor-mediated endocytosis[146-155] (**Figure 13**). The upregulation of surface receptors allows for the binding of targeted nanoparticles to internalize into the cell; CD44 (hyaluronic acid) and folate (folic acid) receptors can be found upregulated on various cancer cells. These targeting biomolecules (ligands) on the nanoparticle surface can be utilized to bind to the cell surface receptors. Nanoparticles could use other internalization methods to internalize into the cell, including modifying the physiochemical properties to change the interaction with the cellular membrane and result in phagocytosis or micropinocytosis, which is the engulfing of entities present into the intracellular space[138, 156-158]. Both mechanisms can enable the internalization of nanoparticles with or without a ligand targeting moiety. Nanoparticles without targeting ligands can bypass the limitation of lacking affinity to a surface receptor to be internalized. There are a variety of nanomaterials that can be utilized as a carrier vehicle as well as numerous surface targeting ligands to be exploited for specific binding. Silica and carbon nanodot-based nanotechnologies are two of these platforms that can be harnessed in biomedical applications, especially bioimaging.

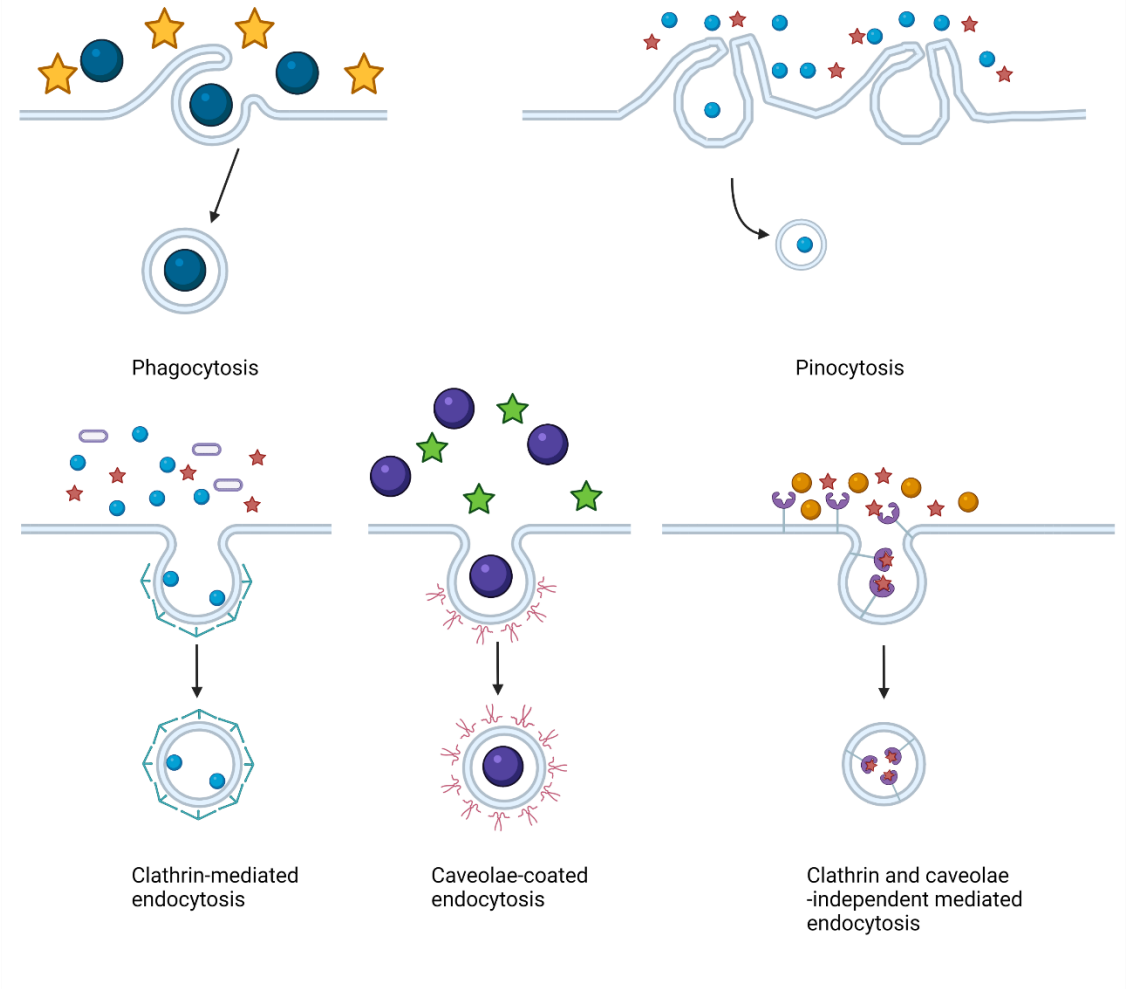

Figure 13. Endocytosis internalization mechanisms. Created using biorender.com.

Silica nanoparticles have emerged as promising nanomaterials for nanotechnology-based applications, especially in bioimaging and drug delivery. As is the case with carbon nanodots, the size of silica nanoparticles can be controlled by the reaction conditions during synthesis. In addition, silica nanoparticles possess easy and low-cost preparation methods, good biocompatibility, a large surface area, and have a hydrophilic nature[159-161]. These unique properties of silica nanoparticles allow for engineering of surface modifications and make these materials desirable for use in a variety of applications. Several synthesis methods form these silica nanoparticles, but the Stöber and the sol-gel methods are the most common. Werner Stöber and his team developed the Stöber method in 1967 to synthesize spherical and monodispersed

nanoparticles in the size of 5-2000 nm from silica alkoxides in the presence of ammonia through hydrolysis and condensation reactions[159, 162]. An advantage of the Stöber method is creating monodispersed nanoparticles over structured silica gels. The Stöber and sol-gel methods both consist of precursor metal alkoxides that undergo hydrolysis and condensation reactions in the presence of water to encourage hydrolysis of the ethyl groups, producing the silanol groups (Si-OH groups) (**Figure 14**). Condensation is promoted in the presence of a base, usually a catalyst, to form polymerization of the silanol groups creating the silica structure through silicon-oxygen-silicon bonds[159, 163, 164]. This method can be seen as a simple process that the precursor material undergoes hydrolysis and condensation reactions to form the structured silica nanomaterial. Tetraethoxysilane (TEOS) is a common metal alkoxide used to create silica nanoparticles through these methods. The reaction conditions, including the pH of the silica reaction, can influence the resulting size and interactions[165-168]. The silica nanoparticle properties of size can impact the specific application of intended use.

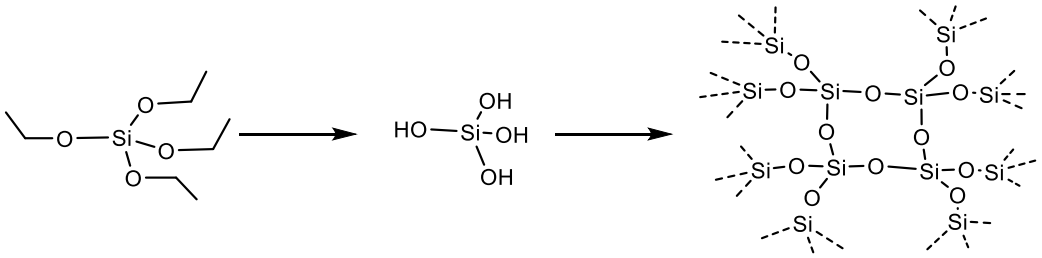

Figure 14. Stöber method of synthesizing silica nanoparticles through hydrolysis and condensation reactions utilizing TEOS as the precursor.

Newly synthesized unmodified silica nanoparticles are negatively charged due to the hydroxyl groups present on the surface. Post-synthesis functional groups can be added to the surface to bind linkers or dyes, including amines, thiols, and epoxy groups[169-172]. Derivatives of alkoxysilane are commonly used to introduce different functional groups on the surface[169]. The

ability to use molecules with silane groups allows these groups to incorporate within the silica nanoparticle synthesis for a more reactive functional group to be present on the surface. 3-aminopropyltriethoxysilane (APTES) is commonly used to produce amine functional groups to further bind other molecules. Amine functional groups can react with dyes, linkers, or other biomolecules, including aldehyde or NHS-ester-based groups. In addition, linker molecules bound to the surface can be functionalized with proteins or other biomolecules, enabling the protein to be in the correct folded shape[169, 173, 174]. The further modifications of these silica nanoparticles can be used for specific bioimaging[175-184] or drug delivery[161, 185-189] applications. Coating the nanoparticle surface by targeting ligands would enhance the delivery of the nanoparticle system to an intended site of interest. There are various conjugation methods to first modify the silica surface with functional groups that can be further modified to link different biomolecules or proteins to allow for targeted binding to biological cells. Silica nanoparticles possess unique structures and properties that enable easy synthesis and surface functionalization methods.

Carbon nanodots are also emerging as a nanomaterial-based nanotechnology intended for use in biomedical applications. These nanodots are a quasi-spherical class of carbon-based nanomaterials with a size of less than 30 nm and provide their own unique properties[190, 191]. The properties of carbon nanodots exhibit carbon elements in an sp^2 hybridized core and oxygen to form carboxyl, hydroxyl, and aldehyde functional groups. Carboxylic functional groups are commonly found on these synthesized nanodots, which allow for a variety of surface modifications that can be tailored for specific uses such as imaging or delivery vehicles. The surface modifications and relatively simple methods for creating these carbon nanodots provide potential advantages over toxic metal-based quantum dots[191]. Creating biocompatible nanomaterials that are also biodegradable without the use of toxic materials or reactants is essential for applications in the clinic. Quantum dots are a class of carbon nanomaterials used in a

variety of applications but show limitations due to the toxic nature of core components of cadmium and selenium, which are harmful to cells and organisms[192]. Both top-down and bottom-up methods can be used to synthesize this carbon dot nanotechnology-based platform due to an abundance of carbon sources, including carbon soot[193-197], citric acid[198-203], and biomass waste[191, 204-206]. One of these methods, the hydrothermal method, is seen as a simplified approach to synthesizing carbon nanodots from various precursors. This process allows for the higher-order crosslinking of the carbon-carbon bonds within the nanodot structure without using toxic materials or highly specialized equipment. In the most basic sense, the hydrothermal synthesis method is a series of condensation reactions that allow the formation of these higher-order carbon bond interactions[198]. This synthesis method is quite simple, only requiring a carbon precursor and a heating mechanism to heat the precursor material to the melting temperature, before allowing the materials to carbonize into more structured carbon bonds. Activation of the surface functional groups can then be utilized as anchoring points for ligand or imaging moiety attachment.

With simple synthesis and the ability to attach functional groups at the surface, silica nanoparticles and carbon nanodots have great potential for bioimaging applications. The incorporation of NIR dye molecules at the surface allows for a nanodot platform to be used to fluoresce certain cells or tissue. Utilizing the fluorescent properties enables the detection of different diseases through fluorescent probes. Cancer detection is one crucial area of interest for many nanomaterial-based systems[207-211]. Targeting cell surface receptors would require ligands attached at the surface to provide specific binding to the intended cell or region. The NIR region of the fluorescent nanodot probes would have a strong emission peak in the 700-1000 nm window where image-guided surgery instrumentation modalities are commonly found to measure fluorescent molecules. Nanodots can have the unique property of exhibiting robust and tunable fluorescence on their own [212]. Targeting cancer cells would enable detection and visualization to help delineate cancerous tissue from healthy tissue. This delineation can also be complimented by

the delivery of encapsulated drugs to the same site[213, 214]. Fluorescently visualizing tumor tissue would significantly improve the correct tissue's likelihood of surgically removed, while improvements to the drug delivery system through surface modifications on nanomaterials would limit the release of encapsulated therapeutic drugs to healthy tissue, a situation that otherwise can be toxic. Silica nanoparticles and carbon nanodots are two of the many nanomaterial-based platforms that can be utilized as bioimaging agents to visualize cancer tumors as well as delivery vehicles for encapsulated therapeutics. Nanomaterial-based platforms are great candidates for the future of nanotechnology in biomedical applications. Many nanomaterials possess unique properties and engineering capabilities for a broad range of biomedical applications. Although there is more research to be completed on these nanomaterial systems and the interaction with the biological environment, the future is promising for the advancement of nanotechnologies because of nanomaterials.

Bibliography

1. Ramsden, J., *Nanotechnology: An Introduction*. William Andrew: **2016**.

2. Findik, F., Nanomaterials and Their Applications. *Period. Eng. Nat. Sci.* **2021**, *9* (3), 62-75.

3. Bhardwaj, V.; Kaushik, A., Biomedical Applications of Nanotechnology and Nanomaterials. Multidisciplinary Digital Publishing Institute: **2017**; Vol. 8, p 298.

4. Li, Y.; Somorjai, G. A., Nanoscale Advances in Catalysis and Energy Applications. *Nano Lett.* **2010**, *10* (7), 2289-2295.

5. Filipponi, L.; Sutherland, D., Nanotechnologies: Principles, Applications, Implications and Hands-on Activities. *Publications Office of the European Union, Luxembourg* **2013**.

6. Zhong, W.-H., Nanoscience and Nanomaterials: Synthesis, Manufacturing and Industry Impacts. DEStech Publications, Inc: **2012**.

7. Baig, N.; Kammakakam, I.; Falath, W., Nanomaterials: A Review of Synthesis Methods, Properties, Recent Progress, and Challenges. *Mater. Adv.* **2021**, *2* (6), 1821-1871.

8. Tulinski, M.; Jurczyk, M., Nanomaterials Synthesis Methods. *Metrology and Standardization of Nanotechnology: Protocols and Industrial Innovations* **2017**, 75-98.

9. Khan, F. A., Synthesis of Nanomaterials: Methods & Technology. In *Applications of Nanomaterials in Human Health*, Springer: **2020**; pp 15-21.

10. Abid, N.; Khan, A. M.; Shujait, S., et al., Synthesis of Nanomaterials Using Various Top-Down and Bottom-up Approaches, Influencing Factors, Advantages, and Disadvantages: A Review. *Adv. Colloid Interface Sci.* **2021**, 102597.

11. Arole, V.; Munde, S., Fabrication of Nanomaterials by Top-Down and Bottom-Up Approaches-an Overview. *J. Mater. Sci.* **2014**, *1*, 89-93.

12. Saravanan, P.; Gopalan, R.; Chandrasekaran, V., Synthesis and Characterisation of Nanomaterials. *Def. Sci. J.* **2008**, *58* (4).

13. Yadav, T. P.; Yadav, R. M.; Singh, D. P., Mechanical Milling: A Top Down Approach for the Synthesis of Nanomaterials and Nanocomposites. *Nanosci. Nanotechnol.* **2012**, *2* (3), 22-48.

14. Neikov, O. D., Mechanical Crushing and Grinding. In *Handbook of Non-Ferrous Metal Powders*, **2009**; pp 45-62.

15. Kim, M.; Osone, S.; Kim, T., et al., Synthesis of Nanoparticles by Laser Ablation: A Review. *KONA.* **2017**, 2017009.

16. Semaltianos, N. G., Nanoparticles by Laser Ablation. *Crit. Rev. Solid State Mater. Sci.* **2010**, *35* (2), 105-124.

17. Lu, K., Nanoparticulate Materials: Synthesis, Characterization, and Processing. John Wiley & Sons: **2012**.

18. Hartanto, A. B.; Ning, X.; Nakata, Y., et al., Growth Mechanism of ZNO Nanorods from Nanoparticles Formed in a Laser Ablation Plume. *Appl. Phys. A.* **2004**, *78* (3), 299-301.

19. Park, H.; Reddy, D. A.; Kim, Y., et al., Synthesis of Ultra-Small Palladium Nanoparticles Deposited on Cds Nanorods by Pulsed Laser Ablation in Liquid: Role of Metal Nanocrystal Size in the Photocatalytic Hydrogen Production. *Chem. Eur. J.* **2017**, *23* (53), 13112-13119.

20. Son, H. H.; Seo, G. H.; Jeong, U., et al., Capillary Wicking Effect of a Cr-Sputtered Superhydrophilic Surface on Enhancement of Pool Boiling Critical Heat Flux. *Int. J. Heat Mass Transf.* **2017**, *113*, 115-128.

21. Wender, H.; Migowski, P.; Feil, A. F., et al., Sputtering Deposition of Nanoparticles onto Liquid Substrates: Recent Advances and Future Trends. *Coord. Chem. Rev.* **2013**, *257* (17-18), 2468-2483.

22. Rane, A. V.; Kanny, K.; Abitha, V., et al., Methods for Synthesis of Nanoparticles and Fabrication of Nanocomposites. *Synthesis of Inorganic Nanomaterials*, Elsevier: **2018**; pp 121-139.

23. Jamkhande, P. G.; Ghule, N. W.; Bamer, A. H., et al., Metal Nanoparticles Synthesis: An Overview on Methods of Preparation, Advantages and Disadvantages, and Applications. *J. Drug Deliv. Sci. Technol.* **2019**, *53*, 101174.

24. Sapkota, B.; Mishra, S., A Simple Ball Milling Method for the Preparation of P-Cuo/N-Zno Nanocomposite Photocatalysts with High Photocatalytic Activity. *J. Nanosci. Nanotechnol.* **2013**, *13* (10), 6588-6596.

25. Ayyub, P.; Chandra, R.; Taneja, P., et al., Synthesis of Nanocrystalline Material by Sputtering and Laser Ablation at Low Temperatures. *Appl. Phys. A* **2001**, *73* (1), 67-73.

26. Langevin, D., Microemulsions. *Acc. Chem. Res.* **1988**, *21* (7), 255-260.

27. Langevin, D., Micelles and Microemulsions. *Annu. Rev. Phys. Chem.* **1992**, *43* (1), 341-369.

28. Paul, B. K.; Moulik, S. P., Microemulsions: An Overview. *J. Dispers. Sci. Technol.* **1997**, *18* (4), 301-367.

29. Ita, K., *Transdermal Drug Delivery: Concepts and Application*. Academic Press: **2020**.

30. Paul, B. K.; Moulik, S. P., Uses and Applications of Microemulsions. *Curr. Sci.* **2001**, 990-1001.

31. Paul, B. K.; Nandy, D., Dilution Method Study on the Interfacial Composition, Thermodynamic Properties and Structural Parameters of W/O Microemulsions Stabilized by 1-Pentanol and Surfactants in Absence and Presence of Sodium Chloride. *J. Colloid Interface Sci.* **2007**, *316* (2), 751-761.

32. Ghimire, P. P.; Jaroniec, M., Renaissance of Stöber Method for Synthesis of Colloidal Particles: New Developments and Opportunities. *J. Colloid Interface Sci.* **2021**, *584*, 838-865.

33. Kolahalam, L. A.; Viswanath, I. K.; Diwakar, B. S., et al., Review on Nanomaterials: Synthesis and Applications. *Mater. Today Proc.* **2019**, *18*, 2182-2190.

34. Schäf, O.; Ghobarkar, H.; Knauth, P., Hydrothermal Synthesis of Nanomaterials. In *Nanostructured Materials*, Springer: **2004**; pp 23-41.

35. Gan, Y. X.; Jayatissa, A. H.; Yu, Z., et al., Hydrothermal Synthesis of Nanomaterials. *Hindawi*: **2020**; Vol. 2020.

36. Hasan, M.; Ullah, I.; Zulfiqar, H., et al., Biological Entities as Chemical Reactors for Synthesis of Nanomaterials: Progress, Challenges and Future Perspective. *Mater. Today Chem.* **2018**, *8*, 13-28.

37. Tantra, R., Nanomaterial Characterization: An Introduction. John Wiley & Sons: **2016**.

38. Arredondo-Ochoa, T.; Silva-Martínez, G. A., Microemulsion Based Nanostructures for Drug Delivery. *Front. Nanotechnol.* **2022**, 98.

39. Fanun, M., Microemulsions as Delivery Systems. *Curr. Opin. Colloid Interface Sci.* **2012**, *17* (5), 306-313.

40. Turkevich, J.; Stevenson, P. C.; Hillier, J., A Study of the Nucleation and Growth Processes in the Synthesis of Colloidal Gold. *Discuss. Faraday Soc.* **1951**, *11*, 55-75.

41. Corriu, R.; Anh, N. T., Molecular Chemistry of Sol-Gel Derived Nanomaterials. John Wiley & Sons: **2009**.

42. Sakka, S.; Kozuka, H., Handbook of Sol-Gel Science and Technology. *1. Sol-Gel Processing*. Springer Science & Business Media: **2005**; Vol. 1.

43. Majhi, K. C.; Yadav, M., Synthesis of Inorganic Nanomaterials Using Carbohydrates. In *Green Sustainable Process for Chemical and Environmental Engineering and Science*, Elsevier: **2021**; pp 109-135.

44. Nasirzadeh, K.; Nazarian, S.; Gheibi Hayat, S. M., Inorganic Nanomaterials: A Brief Overview of the Applications and Developments in Sensing and Drug Delivery. *J. Appl. Biotechnol. Rep.* **2016**, *3* (2), 395-402.

45. Khalid, K.; Tan, X.; Mohd Zaid, H. F., et al., Advanced in Developmental Organic and Inorganic Nanomaterial: A Review. *Bioengineered.* **2020**, *11* (1), 328-355.

46. Paul, W.; Sharma, C. P., Inorganic Nanoparticles for Targeted Drug Delivery. *Biointegration of Medical Implant Materials.* **2020**, 333-373.

47. Rizwan, M.; Shoukat, A.; Ayub, A., et al., Types and Classification of Nanomaterials. *Nanomaterials: Synthesis, Characterization, Hazards and Safety*, Elsevier: **2021**; pp 31-54.

48. Asta, M.; Kauzlarich, S. M.; Liu, K., et al., Inorganic Nanoparticles. Unique Properties and Novel Applications. *Material Matters. (Milwaukee, WI, USA)* **2007**, *2* (1), 3-6.

49. Chen, Y.-C.; Huang, X.-C.; Luo, Y.-L., et al., Non-Metallic Nanomaterials in Cancer Theranostics: A Review of Silica-and Carbon-Based Drug Delivery Systems. *Sci. Technol. Adv. Mater*. **2013**.

50. Wang, J.; Qiu, J., A Review of Organic Nanomaterials in Photothermal Cancer Therapy. *Cancer Research Frontiers.* **2016**, *2* (1), 67-84.

51. Grimsdale, A. C.; Müllen, K., The Chemistry of Organic Nanomaterials. *Angew. Chem. Int. Ed. Engl.* **2005**, *44* (35), 5592-5629.

52. Cartaxo, A., Nanoparticles Types and Properties–Understanding These Promising Devices in the Biomedical Area. *Int. J. Nanomedicine.* **2018**, 1-8.

53. Cha, C.; Shin, S. R.; Annabi, N., et al., Carbon-Based Nanomaterials: Multifunctional Materials for Biomedical Engineering. *ACS nano.* **2013**, *7* (4), 2891-2897.

54. Zhang, B.-T.; Zheng, X.; Li, H.-F., et al., Application of Carbon-Based Nanomaterials in Sample Preparation: A Review. *Anal. Chim. Acta.* **2013**, *784*, 1-17.

55. Maiti, D.; Tong, X.; Mou, X., et al., Carbon-Based Nanomaterials for Biomedical Applications: A Recent Study. *Front. Pharmacol.* **2019**, *9*, 1401.

56. Jeon, I.-Y.; Baek, J.-B., Nanocomposites Derived from Polymers and Inorganic Nanoparticles. *Materials.* **2010**, *3* (6), 3654-3674.

57. Nagraik, R.; Sharma, A.; Kumar, D., et al., Amalgamation of Biosensors and Nanotechnology in Disease Diagnosis: Mini-Review. *Sensors International* **2021**, 100089.

58. Ananikov, V. P., Organic–Inorganic Hybrid Nanomaterials. Multidisciplinary Digital Publishing Institute: **2019**; Vol. 9, p 1197.

59. Liong, M.; Lu, J.; Kovochich, M., et al., Multifunctional Inorganic Nanoparticles for Imaging, Targeting, and Drug Delivery. *ACS nano.* **2008**, *2* (5), 889-896.

60. Farokhzad, O. C.; Langer, R., Impact of Nanotechnology on Drug Delivery. *ACS nano.* **2009**, *3* (1), 16-20.

61. Ochekpe, N. A.; Olorunfemi, P. O.; Ngwuluka, N. C., Nanotechnology and Drug Delivery Part 1: Background and Applications. *Trop. J. Pharm. Res.* **2009**, *8* (3).

62. Nevozhay, D.; Kańska, U.; Budzyńska, R., et al., Current Status of Research on Conjugates and Related Drug Delivery Systems in the Treatment of Cancer and Other Diseases. *Postepy Higieny i Medycyny Doswiadczalnej (Online).* **2007**, *61*, 350-360.

63. Wilczewska, A. Z.; Niemirowicz, K.; Markiewicz, K. H., et al., Nanoparticles as Drug Delivery Systems. *Pharmacol. Rep.* **2012**, *64* (5), 1020-1037.

64. Tiwari, G.; Tiwari, R.; Sriwastawa, B., et al., Drug Delivery Systems: An Updated Review. *Int. J. Pharm. Investig.* **2012**, *2* (1), 2.

65. Suri, S. S.; Fenniri, H.; Singh, B., Nanotechnology-Based Drug Delivery Systems. *J. Occup. Med. Toxicol.* **2007**, *2* (1), 1-6.

66. Jijie, R.; Barras, A.; Boukherroub, R., et al., Nanomaterials for Transdermal Drug Delivery: Beyond the State of the Art of Liposomal Structures. *J. Mater. Chem. B.* **2017**, *5* (44), 8653-8675.

67. Malam, Y.; Loizidou, M.; Seifalian, A. M., Liposomes and Nanoparticles: Nanosized Vehicles for Drug Delivery in Cancer. *Trends Pharmacol. Sci.* **2009**, *30* (11), 592-599.

68. Skourtis, D.; Stavroulaki, D.; Athanasiou, V., et al., Nanostructured Polymeric, Liposomal and Other Materials to Control the Drug Delivery for Cardiovascular Diseases. *Pharm.* **2020**, *12* (12), 1160.

69. Tewari, A.; Peabody, J. O.; Fischer, M., et al., An Operative and Anatomic Study to Help in Nerve Sparing During Laparoscopic and Robotic Radical Prostatectomy. *Eur. Urol.* **2003**, *43* (5), 444-454.

70. Hubbell, J. A.; Chilkoti, A., Nanomaterials for Drug Delivery. *Science.* **2012**, *337* (6092), 303-305.

71. Park, J. H.; von Maltzahn, G.; Ruoslahti, E., et al., Micellar Hybrid Nanoparticles for Simultaneous Magnetofluorescent Imaging and Drug Delivery. *Angew. Chem.* **2008**, *120* (38), 7394-7398.

72. Li, Z.; Tan, S.; Li, S., et al., Cancer Drug Delivery in the Nano Era: An Overview and Perspectives. *Oncol. Rep.* **2017**, *38* (2), 611-624.

73. Yadav, H. K.; Almokdad, A. A.; Sumia, I., et al., Polymer-Based Nanomaterials for Drug-Delivery Carriers. In *Nanocarriers Drug Deliv.*, Elsevier: **2019**; pp 531-556.

74. Mehdipoor, E.; Adeli, M.; Bavadi, M., et al., A Possible Anticancer Drug Delivery System Based on Carbon Nanotube–Dendrimer Hybrid Nanomaterials. *J. Mater. Chem.* **2011**, *21* (39), 15456-15463.

75. Hsu, H. J.; Bugno, J.; Lee, S. r., et al., Dendrimer-Based Nanocarriers: A Versatile Platform for Drug Delivery. *Wiley Interdiscipl. Rev.: Nanomed. Nanobiotechnol.* **2017**, *9* (1), e1409.

76. Zhu, Y.; Liu, C.; Pang, Z., Dendrimer-Based Drug Delivery Systems for Brain Targeting. *Biomolecules.* **2019**, *9* (12), 790.

77. Sherje, A. P.; Jadhav, M.; Dravyakar, B. R., et al., Dendrimers: A Versatile Nanocarrier for Drug Delivery and Targeting. *Int. J. Pharm.* **2018**, *548* (1), 707-720.

78. Kesharwani, P.; Jain, K.; Jain, N. K., Dendrimer as Nanocarrier for Drug Delivery. *Prog. Polym. Sci.* **2014**, *39* (2), 268-307.

79. Kambhampati, S. P.; Kannan, R. M., Dendrimer Nanoparticles for Ocular Drug Delivery. *J. Ocul. Pharm.Ther.* **2013**, *29* (2), 151-165.

80. Douglas, S.; Davis, S.; Illum, L., Nanoparticles in Drug Delivery. *Crit. Rev. Ther. Drug Carrier Syst.* **1987**, *3* (3), 233-261.

81. Haley, B.; Frenkel, E. In Nanoparticles for Drug Delivery in Cancer Treatment, Urologic Oncology: *Semin. Orig. Investig.*, Elsevier: **2008**; pp 57-64.

82. Hans, M. L.; Lowman, A. M., Biodegradable Nanoparticles for Drug Delivery and Targeting. *Curr. Opin. Solid State Mater. Sci.* **2002**, *6* (4), 319-327.

83. Soppimath, K. S.; Aminabhavi, T. M.; Kulkarni, A. R., et al., Biodegradable Polymeric Nanoparticles as Drug Delivery Devices. *J. Controlled Release.* **2001**, *70* (1-2), 1-20.

84. Cho, K.; Wang, X.; Nie, S., et al., Therapeutic Nanoparticles for Drug Delivery in Cancer. *Clin. Cancer Res.* **2008**, *14* (5), 1310-1316.

85. Couvreur, P., Nanoparticles in Drug Delivery: Past, Present and Future. *Adv. Drug Deliv. Rev.* **2013**, *65* (1), 21-23.

86. Nagano, T., Development of Fluorescent Probes for Bioimaging Applications. *Proc. Jpn Acad., Ser. B Phys. Biol. Sci.* **2010**, *86* (8), 837-847.

87. Srinivasarao, M.; Galliford, C. V.; Low, P. S., Principles in the Design of Ligand-Targeted Cancer Therapeutics and Imaging Agents. *Nat. Rev. Drug Discov.* **2015**, *14* (3), 203-219.

88. Barreto, J. A.; O'Malley, W.; Kubeil, M., et al., Nanomaterials: Applications in Cancer Imaging and Therapy. *Adv. Mater.* **2011**, *23* (12), H18-H40.

89. Park, J.-H.; von Maltzahn, G.; Xu, M. J., et al., Cooperative Nanomaterial System to Sensitize, Target, and Treat Tumors. *Proc.Natl. Acad. Sci.* **2010**, *107* (3), 981-986.

90. Vankayala, R.; Hwang, K. C., Near-Infrared-Light-Activatable Nanomaterial-Mediated Phototheranostic Nanomedicines: An Emerging Paradigm for Cancer Treatment. *Adv. Mater.* **2018**, *30* (23), 1706320.

91. Liang, Y.-X.; Cheung, S. W.; Chan, K. C., et al., CNS Regeneration after Chronic Injury Using a Self-Assembled Nanomaterial and Memri for Real-Time in Vivo Monitoring. *Nanomedicine.* **2011**, *7* (3), 351-359.

92. Bae, K. H.; Chung, H. J.; Park, T. G., Nanomaterials for Cancer Therapy and Imaging. *Mol. Cell.* **2011**, *31* (4), 295-302.

93. Saleem, J.; Wang, L.; Chen, C., Carbon-Based Nanomaterials for Cancer Therapy Via Targeting Tumor Microenvironment. *Adv. Healthc. Mater.* **2018**, *7* (20), 1800525.

94. Chen, F.; Cai, W., Tumor Vasculature Targeting: A Generally Applicable Approach for Functionalized Nanomaterials. *Small.* **2014**, *10* (10), 1887-1893.

95. Qin, W.; Huang, G.; Chen, Z., et al., Nanomaterials in Targeting Cancer Stem Cells for Cancer Therapy. *Front. Pharmacol.* **2017**, *8*, 1.

96. Ovais, M.; Guo, M.; Chen, C., Tailoring Nanomaterials for Targeting Tumor-Associated Macrophages. *Adv. Mater.* **2019**, *31* (19), 1808303.

97. Ji, T.; Zhao, Y.; Ding, Y., et al., Using Functional Nanomaterials to Target and Regulate the Tumor Microenvironment: Diagnostic and Therapeutic Applications. *Adv. Mater.* **2013**, *25* (26), 3508-3525.

98. Bradbury, M. S.; Phillips, E.; Montero, P. H., et al., Clinically-Translated Silica Nanoparticles as Dual-Modality Cancer-Targeted Probes for Image-Guided Surgery and Interventions. *Integr. Biol.* **2013**, *5* (1), 74-86.

99. Lakowicz, J. R., Quenching of Fluorescence. *Principles of Fluorescence Spectroscopy*. **1983**, 257-301.

100. Xiao, D.; Qi, H.; Teng, Y., et al., Advances and Challenges of Fluorescent Nanomaterials for Synthesis and Biomedical Applications. *Nanoscale Res. Lett.* **2021**, *16* (1), 1-23.

101. Bünau, G. v.; Birks, J., Photophysics of Aromatic Molecules. Wiley-Interscience, London 1970. 704 Seiten. Preis: 210s. *Ber. Bunsenges. Physik. Chem.* **1970**, *74*, 1294-1295.

102. Zhu, C.; Kwok, R. T.; Lam, J. W., et al., Aggregation-Induced Emission: A Trailblazing Journey to the Field of Biomedicine. *ACS Appl. Bio Mater.* **2018**, *1* (6), 1768-1786.

103. Hong, Y.; Lam, J. W.; Tang, B. Z., Aggregation-Induced Emission. *Chem. Soc. Rev.* **2011**, *40* (11), 5361-5388.

104. Mei, J.; Hong, Y.; Lam, J. W., et al., Aggregation-Induced Emission: The Whole Is More Brilliant Than the Parts. *Adv. Mater.* **2014**, *26* (31), 5429-5479.

105. Mei, J.; Leung, N. L.; Kwok, R. T., et al., Aggregation-Induced Emission: Together We Shine, United We Soar! *Chem. Rev.* **2015**, *115* (21), 11718-11940.

106. Qian, J.; Tang, B. Z., Aie Luminogens for Bioimaging and Theranostics: From Organelles to Animals. *Chem.* **2017**, *3* (1), 56-91.

107. Luo, J.; Xie, Z.; Lam, J. W., et al., Aggregation-Induced Emission of 1-Methyl-1, 2, 3, 4, 5-Pentaphenylsilole. *Chem. Commun.* **2001**, (18), 1740-1741.

108. Dolai, J.; Mandal, K.; Jana, N. R., Nanoparticle Size Effects in Biomedical Applications. *ACS Appl. Nano Mater.* **2021**, *4* (7), 6471-6496.

109. Peynshaert, K.; Manshian, B. B.; Joris, F., et al., Exploiting Intrinsic Nanoparticle Toxicity: The Pros and Cons of Nanoparticle-Induced Autophagy in Biomedical Research. *Chem. Rev.* **2014**, *114* (15), 7581-7609.

110. Blanco, E.; Shen, H.; Ferrari, M., Principles of Nanoparticle Design for Overcoming Biological Barriers to Drug Delivery. *Nature Biotechnol.* **2015**, *33* (9), 941-951.

111. Pradhan, N.; Debnath, K.; Mandal, S., et al., Antiamyloidogenic Chemical/Biochemical-Based Designed Nanoparticle as Artificial Chaperone for Efficient Inhibition of Protein Aggregation. *Biomacromolecules.* **2018**, *19* (6), 1721-1731.

112. Yang, B.; Chen, Y.; Shi, J., Reactive Oxygen Species (ROS)-Based Nanomedicine. *Chem. Rev.* **2019**, *119* (8), 4881-4985.

113. Liu, Y.; Wang, J.; Xiong, Q., et al., Nano–Bio Interactions in Cancer: From Therapeutics Delivery to Early Detection. *Acc. Chem. Res.* **2020**, *54* (2), 291-301.

114. Sapsford, K. E.; Algar, W. R.; Berti, L., et al., Functionalizing Nanoparticles with Biological Molecules: Developing Chemistries That Facilitate Nanotechnology. *Chem. Rev.* **2013**, *113* (3), 1904-2074.

115. Murphy, C. J.; Vartanian, A. M.; Geiger, F. M., et al., Biological Responses to Engineered Nanomaterials: Needs for the Next Decade. *ACS Cent. Sci.* **2015**, *1* (3), 117-123.

116. Amin, M. L.; Joo, J. Y.; Yi, D. K., et al., Surface Modification and Local Orientations of Surface Molecules in Nanotherapeutics. *J. Controlled Release.* **2015**, *207*, 131-142.

117. Faraji, A. H.; Wipf, P., Nanoparticles in Cellular Drug Delivery. *Bioorg. Med. Chem.* **2009**, *17* (8), 2950-2962.

118. Yih, T.; Al-Fandi, M., Engineered Nanoparticles as Precise Drug Delivery Systems. *J. Cell. Biochem.* **2006**, *97* (6), 1184-1190.

119. Ulbrich, K.; Hekmatara, T.; Herbert, E., et al., Transferrin-and Transferrin-Receptor-Antibody-Modified Nanoparticles Enable Drug Delivery across the Blood–Brain Barrier (BBB). *Eur. J. Pharm. Biopharm.* **2009**, *71* (2), 251-256.

120. Rana, S.; Bajaj, A.; Mout, R., et al., Monolayer Coated Gold Nanoparticles for Delivery Applications. *Adv. Drug Deliv. Rev.* **2012**, *64* (2), 200-216.

121. Negi, L. M.; Talegaonkar, S.; Jaggi, M., et al., Role of CD44 in Tumour Progression and Strategies for Targeting. *J. Drug Target.* **2012**, *20* (7), 561-573.

122. Wang, L.; Su, W.; Liu, Z., et al., CD44 Antibody-Targeted Liposomal Nanoparticles for Molecular Imaging and Therapy of Hepatocellular Carcinoma. *Biomaterials.* **2012**, *33* (20), 5107-5114.

123. Alshaer, W.; Hillaireau, H.; Vergnaud, J., et al., Functionalizing Liposomes with Anti-CD44 Aptamer for Selective Targeting of Cancer Cells. *Bioconjug. Chem.* **2015**, *26* (7), 1307-1313.

124. Hayward, S. L.; Wilson, C. L.; Kidambi, S., Hyaluronic Acid-Conjugated Liposome Nanoparticles for Targeted Delivery to CD44 Overexpressing Glioblastoma Cells. *Oncotarget.* **2016**, *7* (23), 34158.

125. Seo, J.-H.; Lee, S. Y.; Hwang, C., et al., Multi-Layered Cellulose Nanocrystal System for Cd44 Receptor-Positive Tumor-Targeted Anticancer Drug Delivery. *Int. J. Biol. Macromol.* **2020**, *162*, 798-809.

126. Yang, C.; He, Y.; Zhang, H., et al., Selective Killing of Breast Cancer Cells Expressing Activated Cd44 Using Cd44 Ligand-Coated Nanoparticles in Vitro and in Vivo. *Oncotarget.* **2015**, *6* (17), 15283.

127. Platt, V. M.; Szoka Jr, F. C., Anticancer Therapeutics: Targeting Macromolecules and Nanocarriers to Hyaluronan or Cd44, a Hyaluronan Receptor. *Mol. Pharm.* **2008**, *5* (4), 474-486.

128. Säälik, P.; Lingasamy, P.; Toome, K., et al., Peptide-Guided Nanoparticles for Glioblastoma Targeting. *J. Controlled Release.* **2019**, *308*, 109-118.

129. Kuznetsova, N. R.; Stepanova, E. V.; Peretolchina, N. M., et al., Targeting Liposomes Loaded with Melphalan Prodrug to Tumour Vasculature Via the Sialyl Lewis X Selectin Ligand. *J. Drug Target.* **2014**, *22* (3), 242-250.

130. Tietjen, G. T.; Bracaglia, L. G.; Saltzman, W. M., et al., Focus on Fundamentals: Achieving Effective Nanoparticle Targeting. *Trends Mol. Med.* **2018**, *24* (7), 598-606.

131. Castillo, L.; Etienne-Grimaldi, M.; Fischel, J., et al., Pharmacological Background of Egfr Targeting. *Ann. Oncol.* **2004**, *15* (7), 1007-1012.

132. Nguyen, P. V.; Allard-Vannier, E.; Chourpa, I., et al., Nanomedicines Functionalized with Anti-Egfr Ligands for Active Targeting in Cancer Therapy: Biological Strategy, Design and Quality Control. *Int. J. Pharm.* **2021**, *605*, 120795.

133. Nguyen, P. V.; Hervé-Aubert, K.; Chourpa, I., et al., Active Targeting Strategy in Nanomedicines Using Anti-Egfr Ligands–a Promising Approach for Cancer Therapy and Diagnosis. *Int. J. Pharm.* **2021**, *609*, 121134.

134. Song, S.; Liu, D.; Peng, J., et al., Peptide Ligand-Mediated Liposome Distribution and Targeting to Egfr Expressing Tumor in Vivo. *Int. J. Pharm.* **2008**, *363* (1-2), 155-161.

135. Kenny, P. A.; Bissell, M. J., Targeting Tace-Dependent Egfr Ligand Shedding in Breast Cancer. *J. Clin. Investig.* **2007**, *117* (2), 337-345.

136. Arteaga, C. In Targeting Her1/Egfr: A Molecular Approach to Cancer Therapy, *Semin. Oncol.*, Elsevier: **2003**; pp 3-14.

137. Mickler, F. M.; Möckl, L.; Ruthardt, N., et al., Tuning Nanoparticle Uptake: Live-Cell Imaging Reveals Two Distinct Endocytosis Mechanisms Mediated by Natural and Artificial Egfr Targeting Ligand. *Nano Lett.* **2012**, *12* (7), 3417-3423.

138. Behzadi, S.; Serpooshan, V.; Tao, W., et al., Cellular Uptake of Nanoparticles: Journey inside the Cell. *Chem. Soc. Rev.* **2017**, *46* (14), 4218-4244.

139. Petros, R. A.; DeSimone, J. M., Strategies in the Design of Nanoparticles for Therapeutic Applications. *Nat. Rev. Drug Disc.* **2010**, *9* (8), 615-627.

140. Chou, L. Y.; Ming, K.; Chan, W. C., Strategies for the Intracellular Delivery of Nanoparticles. *Chem. Soc. Rev.* **2011**, *40* (1), 233-245.

141. Pridgen, E. M.; Alexis, F.; Farokhzad, O. C., Polymeric Nanoparticle Drug Delivery Technologies for Oral Delivery Applications. *Expert Opin. Drug Deliv.* 2015, *12* (9), 1459-1473.

142. Yameen, B.; Choi, W. I.; Vilos, C., et al., Insight into Nanoparticle Cellular Uptake and Intracellular Targeting. *J. Controlled Release.* **2014**, *190*, 485-499.

143. Prabhakar, U.; Maeda, H.; Jain, R. K., et al., Challenges and Key Considerations of the Enhanced Permeability and Retention Effect for Nanomedicine Drug Delivery in Oncology. *Clin. Cancer Res.*: **2013,** *73*, 2412-2417.

144. Zhang, X.-Q.; Xu, X.; Bertrand, N., et al., Interactions of Nanomaterials and Biological Systems: Implications to Personalized Nanomedicine. *Adv. Drug Deliv. Rev.* **2012**, *64* (13), 1363-1384.

145. Mahmoudi, M.; Sant, S.; Wang, B., et al., Superparamagnetic Iron Oxide Nanoparticles (Spions): Development, Surface Modification and Applications in Chemotherapy. *Adv. Drug Deliv. Rev.* **2011**, *63* (1-2), 24-46.

146. Sharifi, S.; Behzadi, S.; Laurent, S., et al., Toxicity of Nanomaterials. *Chem. Soc. Rev.* **2012**, *41* (6), 2323-2343.

147. Kumari, S.; Mg, S.; Mayor, S., Endocytosis Unplugged: Multiple Ways to Enter the Cell. *Cell Res.* **2010**, *20* (3), 256-275.

148. Kirkham, M.; Fujita, A.; Chadda, R., et al., Ultrastructural Identification of Uncoated Caveolin-Independent Early Endocytic Vehicles. *J. Cell Biol.* **2005**, *168* (3), 465-476.

149. Damm, E.-M.; Pelkmans, L.; Kartenbeck, J. r., et al., Clathrin-and Caveolin-1–Independent Endocytosis: Entry of Simian Virus 40 into Cells Devoid of Caveolae. *J. Cell Biol.* **2005**, *168* (3), 477-488.

150. Doherty, G. J.; McMahon, H. T., Mechanisms of Endocytosis. *Annu. Rev. Biochem.* **2009**, *78*, 857-902.

151. Lu, Y.; Low, P. S., Folate-Mediated Delivery of Macromolecular Anticancer Therapeutic Agents. *Adv. Drug Deliv. Rev.* **2002**, *54* (5), 675-693.

152. Gao, H.; Shi, W.; Freund, L. B., Mechanics of Receptor-Mediated Endocytosis. *Proc. Natl. Acad. Sci.* **2005**, *102* (27), 9469-9474.

153. Wileman, T.; Harding, C.; Stahl, P., Receptor-Mediated Endocytosis. *Biochem. J.* **1985**, *232* (1), 1.

154. Stahl, P.; Schwartz, A. L., Receptor-Mediated Endocytosis. *J. Clin. Investig.* **1986**, *77* (3), 657-662.

155. Vácha, R.; Martinez-Veracoechea, F. J.; Frenkel, D., Receptor-Mediated Endocytosis of Nanoparticles of Various Shapes. *Nano Lett.* **2011**, *11* (12), 5391-5395.

156. Hillaireau, H.; Couvreur, P., Nanocarriers' Entry into the Cell: Relevance to Drug Delivery. *Cell. Mol. Life Sci.* **2009**, *66* (17), 2873-2896.

157. Lim, J. P.; Gleeson, P. A., Macropinocytosis: An Endocytic Pathway for Internalising Large Gulps. *Immunol. Cell Biol.* **2011**, *89* (8), 836-843.

158. Li, Y.-X.; Pang, H.-B., Macropinocytosis as a Cell Entry Route for Peptide-Functionalized and Bystander Nanoparticles. *J. Controlled Release.* **2021**, *329*, 1222-1230.

159. Jeelani, P. G.; Mulay, P.; Venkat, R., et al., Multifaceted Application of Silica Nanoparticles. A Review. *Silicon.* **2020**, *12* (6), 1337-1354.

160. Rao, K. S.; El-Hami, K.; Kodaki, T., et al., A Novel Method for Synthesis of Silica Nanoparticles. *J. Colloid Interface Sci.* **2005**, *289* (1), 125-131.

161. Wang, Y.; Zhao, Q.; Han, N., et al., Mesoporous Silica Nanoparticles in Drug Delivery and Biomedical Applications. *Nanomedecine.*. **2015**, *11* (2), 313-327.

162. Stöber, W.; Fink, A.; Bohn, E., Controlled Growth of Monodisperse Silica Spheres in the Micron Size Range. *J. Colloid Interface Sci.* **1968**, *26* (1), 62-69.

163. Klabunde, K. J.; Stark, J.; Koper, O., et al., Nanocrystals as Stoichiometric Reagents with Unique Surface Chemistry. *J. Phys. Chem.* **1996**, *100* (30), 12142-12153.

164. Hench, L. L., West, J. K.; The Sol-Gel Process *Chem. Rev.* **1990**, *90*, 33-72.

165. Mehmood, A.; Ghafar, H.; Yaqoob, S., et al., Mesoporous Silica Nanoparticles: A Review. *J. Dev. Drugs.* **2017**, *6* (02).

166. Monnier, A.; Schuth, F.; Kumar, Q., et al., High-Resolution Transmission Electron Microscopy of Mesoporous Mcm-41 Type Materials. *Science.* **1993**, *261*, 1299.

167. Zhao, D.; Sun, J.; Li, Q., et al., Morphological Control of Highly Ordered Mesoporous Silica Sba-15. *Chem. Mater.* **2000**, *12* (2), 275-279.

168. Huo, Q.; Margolese, D. I.; Stucky, G. D., Surfactant Control of Phases in the Synthesis of Mesoporous Silica-Based Materials. *Chem. Mater.* **1996**, *8* (5), 1147-1160.

169. Gubala, V.; Giovannini, G.; Kunc, F., et al., Dye-Doped Silica Nanoparticles: Synthesis, Surface Chemistry and Bioapplications. *Cancer Nanotechnol.* **2020**, *11* (1), 1-43.

170. Claesson, E. M.; Philipse, A. P., Thiol-Functionalized Silica Colloids, Grains, and Membranes for Irreversible Adsorption of Metal (Oxide) Nanoparticles. *Colloids Surf. A Physicochem. Eng. Asp.* **2007**, *297* (1-3), 46-54.

171. Zhang, Q.; Huang, R.; Guo, L.-H., One-Step and High-Density Protein Immobilization on Epoxysilane-Modified Silica Nanoparticles. *Sci. Bull.* **2009**, *54* (15), 2620-2626.

172. Bagwe, R. P.; Hilliard, L. R.; Tan, W., Surface Modification of Silica Nanoparticles to Reduce Aggregation and Nonspecific Binding. *Langmuir.* **2006**, *22* (9), 4357-4362.

173. Korzeniowska, B.; Nooney, R.; Wencel, D., et al., Silica Nanoparticles for Cell Imaging and Intracellular Sensing. *Nanotechnology.* **2013**, *24* (44), 442002.

174. Moore, C.; Monton, H.; O'Kennedy, R., et al., Controlling Colloidal Stability of Silica Nanoparticles During Bioconjugation Reactions with Proteins and Improving Their Longer-Term Stability, Handling and Storage. *J. Mater. Chem. B.* **2015**, *3* (10), 2043-2055.

175. Cha, B. G.; Kim, J., Functional Mesoporous Silica Nanoparticles for Bio-Imaging Applications. *Wiley Interdiscip. Rev. Nanomed Nanobiotechnol.* **2019**, *11* (1), e1515.

176. Santra, S.; Bagwe, R. P.; Dutta, D., et al., Synthesis and Characterization of Fluorescent, Radio-Opaque, and Paramagnetic Silica Nanoparticles for Multimodal Bioimaging Applications. *Adv. Mater.* **2005**, *17* (18), 2165-2169.

177. Sharma, P.; Brown, S.; Walter, G., et al., Nanoparticles for Bioimaging. *Adv. Colloid Interface Sci.* **2006**, *123*, 471-485.

178. Sreejith, S.; Ma, X.; Zhao, Y., Graphene Oxide Wrapping on Squaraine-Loaded Mesoporous Silica Nanoparticles for Bioimaging. *J. Am. Chem. Soc.* **2012**, *134* (42), 17346-17349.

179. Yoo, J.; Han, S.; Park, W., et al., Defect-Induced Fluorescence of Silica Nanoparticles for Bioimaging Applications. *ACS Appl. Mater. Interfaces.* **2018**, *10* (51), 44247-44256.

180. Wang, L.; Zhao, W.; Tan, W., Bioconjugated Silica Nanoparticles: Development and Applications. *Nano Res.* **2008**, *1* (2), 99-115.

181. Yuan, D.; Ellis, C. M.; Davis, J. J., Mesoporous Silica Nanoparticles in Bioimaging. *Materials.* **2020**, *13* (17), 3795.

182. Gomes, M. C.; Cunha, A.; Trindade, T., et al., The Role of Surface Functionalization of Silica Nanoparticles for Bioimaging. *J. Innov. Opt. Health Sci.* **2016**, *9* (04), 1630005.

183. Song, X.; Li, F.; Ma, J., et al., Synthesis of Fluorescent Silica Nanoparticles and Their Applications as Fluorescence Probes. *J. Fluoresc.* **2011**, *21* (3), 1205-1212.

184. Yang, H.; Lou, C.; Xu, M., et al., Investigation of Folate-Conjugated Fluorescent Silica Nanoparticles for Targeting Delivery to Folate Receptor-Positive Tumors and Their Internalization Mechanism. *Int. J. Nanomedicine.* **2011**, *6*, 2023.

185. Argyo, C.; Weiss, V.; Bräuchle, C., et al., Multifunctional Mesoporous Silica Nanoparticles as a Universal Platform for Drug Delivery. *Chem. Mater.* **2014**, *26* (1), 435-451.

186. Vivero-Escoto, J. L.; Slowing, I. I.; Trewyn, B. G., et al., Mesoporous Silica Nanoparticles for Intracellular Controlled Drug Delivery. *Small.* **2010**, *6* (18), 1952-1967.

187. Bharti, C.; Nagaich, U.; Pal, A. K., et al., Mesoporous Silica Nanoparticles in Target Drug Delivery System: A Review. *Int. J.Pharm. Investig.* **2015**, *5* (3), 124.

188. Iturrioz-Rodríguez, N.; Correa-Duarte, M. A.; Fanarraga, M. L., Controlled Drug Delivery Systems for Cancer Based on Mesoporous Silica Nanoparticles. *Int. J. Nanomed.* **2019**, *14*, 3389.

189. Rosenholm, J. M.; Sahlgren, C.; Lindén, M., Towards Multifunctional, Targeted Drug Delivery Systems Using Mesoporous Silica Nanoparticles–Opportunities & Challenges. *Nanoscale.* **2010**, *2* (10), 1870-1883.

190. Kasouni, A.; Chatzimitakos, T.; Stalikas, C., Bioimaging Applications of Carbon Nanodots: A Review. *C.* **2019**, *5* (2), 19.

191. Baker, S. N.; Baker, G. A., Luminescent Carbon Nanodots: Emergent Nanolights. *Angew. Chem. Int. Ed. Engl.* **2010**, *49* (38), 6726-6744.

192. Bottrill, M.; Green, M., Some Aspects of Quantum Dot Toxicity. *Chem. Commun.* **2011**, *47* (25), 7039-7050.

193. Zhang, Q.; Sun, X.; Ruan, H., et al., Production of Yellow-Emitting Carbon Quantum Dots from Fullerene Carbon Soot. *Sci. China Mater.* **2017**, *60* (2), 141-150.

194. Ghosh, T.; Ghosh, R.; Basak, U., et al., Candle Soot Derived Carbon Nanodot/Polyaniline Hybrid Materials through Controlled Grafting of Polyaniline Chains for Supercapacitors. *J. Mater. Chem. A.* **2018**, *6* (15), 6476-6492.

195. Russo, C.; Apicella, B.; Ciajolo, A., Blue and Green Luminescent Carbon Nanodots from Controllable Fuel-Rich Flame Reactors. *Sci. Rep.* **2019**, *9* (1), 1-8.

196. Mohan Anu, N.; Manoj, B., Exploration of Carbon Nano Dots in Hydro Carbon Soot and Carbon Black. *Res. J. Chem. Environ.* **2017**, *21*, 2.

197. Ko, H. Y.; Chang, Y. W.; Paramasivam, G., et al., In Vivo Imaging of Tumour Bearing near-Infrared Fluorescence-Emitting Carbon Nanodots Derived from Tire Soot. *Chem. Commun.* **2013**, *49* (87), 10290-10292.

198. Loo, A. H.; Sofer, Z.; Bouša, D., et al., Carboxylic Carbon Quantum Dots as a Fluorescent Sensing Platform for DNA Detection. *ACS Appl. Mater. Interfaces.* **2016**, *8* (3), 1951-1957.

199. Gude, V., Synthesis of Hydrophobic Photoluminescent Carbon Nanodots by Using L-Tyrosine and Citric Acid Through a Thermal Oxidation Route. *Beilstein J. Nanotech.* **2014**, *5* (1), 1513-1522.

200. Strauss, V.; Margraf, J. T.; Clark, T., et al., A Carbon–Carbon Hybrid–Immobilizing Carbon Nanodots onto Carbon Nanotubes. *Chem. Sci.* **2015**, *6* (12), 6878-6885.

201. Ji, Z.; Yin, Z.; Jia, Z., et al., Carbon Nanodots Derived from Urea and Citric Acid in Living Cells: Cellular Uptake and Antioxidation Effect. *Langmuir.* **2020**, *36* (29), 8632-8640.

202. Strauss, V.; Wang, H.; Delacroix, S., et al., Carbon Nanodots Revised: The Thermal Citric Acid/Urea Reaction. *Chem. Sci.* **2020**, *11* (31), 8256-8266.

203. Zhu, S.; Zhao, X.; Song, Y., et al., Beyond Bottom-up Carbon Nanodots: Citric-Acid Derived Organic Molecules. *Nano Today.* **2016**, *11* (2), 128-132.

204. Zhao, W.; Wang, Y.; Liu, K., et al., Multicolor Biomass Based Carbon Nanodots for Bacterial Imaging. *Chin. Chem. Lett.* **2021**.

205. Marinovic, A.; Kiat, L. S.; Dunn, S., et al., Carbon-Nanodot Solar Cells from Renewable Precursors. *ChemSusChem.* **2017**.

206. Jiang, D.; Zhang, Y.; Huang, M., et al., Carbon Nanodots as Reductant and Stabilizer for One-Pot Sonochemical Synthesis of Amorphous Carbon-Supported Silver Nanoparticles for Electrochemical Nonenzymatic H2o2 Sensing. *J. Electroanal. Chem.* **2014**, *728*, 26-33.

207. Chen, Y.; Wu, Y.; Sun, B., et al., Two-Dimensional Nanomaterials for Cancer Nanotheranostics. *Small.* **2017**, *13* (10), 1603446.

208. Nazir, S.; Hussain, T.; Ayub, A., et al., Nanomaterials in Combating Cancer: Therapeutic Applications and Developments. *Nanomedicine.* **2014**, *10* (1), 19-34.

209. Chen, D.; Dougherty, C. A.; Zhu, K., et al., Theranostic Applications of Carbon Nanomaterials in Cancer: Focus on Imaging and Cargo Delivery. *J. Controlled Release.* **2015**, *210*, 230-245.

210. Wang, Y.; Sun, S.; Zhang, Z., et al., Nanomaterials for Cancer Precision Medicine. *Adv. Mater*. **2018**, *30* (17), 1705660.

211. Wang, H.; Wu, T.; Li, M., et al., Recent Advances in Nanomaterials for Colorimetric Cancer Detection. *J. Mater. Chem. B.* **2021**, *9* (4), 921-938.

212. Shafi, A.; Bano, S.; Sabir, S., et al., Eco-Friendly Fluorescent Carbon Nanodots: Characteristics and Potential Applications. In Carbon-Based Material for Environmental Protection and Remediation, *IntechOpen*. **2020**.

213. Lee, C. H.; Rajendran, R.; Jeong, M.-S., et al., Bioimaging of Targeting Cancers Using Aptamer-Conjugated Carbon Nanodots. *Chem. Commun.* **2013**, *49* (58), 6543-6545.

214. Li, X.; Shi, L.; Li, L., et al., Recent Advances in Carbon Nanodots: Properties and Applications in Cancer Diagnosis and Treatment. *J. Anal. Test.* **2019**, *3* (1), 37-49.

PREPARATION AND IN VITRO EVALUATION OF HYALURONIC ACID COATED FLUORESCENT NANOPARTICLES

Abstract

Functionalized fluorescent nanoparticles continue to emerge as promising candidates for drug delivery, bioimaging, and labeling tools for a variety of biomedical applications. The ability for nanomaterials to fluorescently label cells can enhance the detection and understanding of diseases. The concept of tailoring nanomaterial-based systems for certain functions is becoming increasingly popular. Silica nanoparticles have a variety of unique properties that can be harnessed for many different applications. They have versatile surfaces that can be functionalized with different moieties and are non-toxic. In this study, fluorescent silica nanoparticles were synthesized by a modified Stöber method utilizing tetraethyl orthosilicate (TEOS) as a precursor and the fluorophore, sulfo-Cy5-amine. They were further modified by coating with hyaluronic acid (HA) to target CD44. CD44 is a cell surface receptor that is commonly upregulated on a variety of cancer and associated cells. Using fluorescence microscopy, it was shown that the HA-coated silica nanoparticles had a higher interaction with the CD44+ breast cancer cell line, MDA-MB-231, than with the BT-474 cells, which are CD44-. These results suggest that HA-coated silica nanoparticles could be a promising bioimaging tool for visualizing CD44+ tumor cells.

Introduction

Nanotechnology has a promising role for biomedical applications, including imaging and delivery tools. New properties and functions provided through small size, control and manipulation of material at the atomic scale drive nanotechnology innovation[1]. Engineering nanoparticles as functionalized systems has increased in popularity in different applications due to their unique properties and versatility as a nanotechnology platform [2]. Silica-based systems are a widely investigated nanomaterial platform due to their unique properties such as

biocompatibility, ease of functionalization, stability, and hydrophilic surface[3-7]. Thus, silica nanoparticles can be tailored for targeting purposes through attachment of target-specific ligands or be functionalized with fluorescent dyes to serve as imaging or theranostic materials[8-11].

High quantum yields of organic fluorescent dyes are important for their efficient use as imaging tools. Their brightness can be further enhanced by entrapment into organic or inorganic matrices[12-14]. However, organic dyes are prone to self-quenching due to energy transfer or reabsorption in highly concentrated solutions or in an aggregate state[13, 15-18]. In order to achieve higher contrast and enhanced photostability of the fluorescent materials, organic fluorescent dyes can be incorporated into silica nanoparticles. This would increase the amount of the dye molecules in a localized area without reducing the fluorescent intensity and reduce the possibility of structural degradations of the dye molecules. One of the ways to achieve the dye incorporation is through modification of the Stöber method[17], which is a common approach to synthesize silica nanoparticles using silica alkoxide precursors[19, 20].

Following dye incorporation, modifications to the surface by functional groups can enhance the unique nanoscale properties and versatility to target specific receptors. The additional functional groups can be used to attach various targeting ligands to the nanoparticle's surface, which will make it specific to certain cells that are characterized by upregulation of particular surface receptors. For example, hyaluronic acid has been extensively investigated and demonstrates a strong affinity to the CD44 receptors overexpressed in various cancer cells[21-24]. Therefore, hyaluronic acid-coated nanoparticles can provide enhanced affinity to the CD44 cell receptors and exhibit preferential accumulation in cancerous tissues that overexpress CD44.

In this study, we first develop dye-incorporated silica nanoparticles. In order to target overexpressed CD44 cell receptors, bare fluorescent silica nanoparticles underwent surface modification with APTES followed by coating with hyaluronic acid (HA) via electrostatic

interaction. We further evaluate the cellular internalization of these HA-coated fluorescent silica nanoparticles in CD44+ and CD44- breast cancer cell lines.

Materials and Methods

Materials and Reagents

Sulfo-Cy5-amine (sCy5-amine) and sulfo-Cy5-NHS (sCy5-NHS) were purchased from Lumiprobe, Inc. (Hunt Valley, MD, USA). 3-triethoxysiylpropyl succinic anhydride (TSPA) was obtained from Oakwood Chemical (Estill, SC, USA). Tetraethyl orthosilicate (TEOS), Amicon centrifugal filters (10 kDa molecular weight cutoff (MWCO)), dimethyl sulfoxide (DMSO), ammonium chloride ammonium hydroxide buffer, toluene, and HEPES buffer (N-(2-Hydroxyethyl) piperazine-N′-(2-ethane sulfonic acid), 4-(2-Hydroxyethyl) piperazine-1-ethane sulfonic acid) were obtained from Sigma Aldrich (St. Louis, MO, USA). 3-aminopropyltriethoxysilane (APTES) and paraformaldehyde were purchased from Alfa Aesar (Ward Hill, MA, USA) and cyclohexane was purchased from Acros Organics (New Jersey, USA), Hyaluronic acid (10 kDa) was obtained from Lifecore Biomedical (Chaska, MN). RPMI 1640 media, penicillin-streptomycin, radioimmunoprecipitation assay (RIPA), and Halt protease inhibitor were purchased from Thermo Scientific (Carlsbad, CA, USA) and fetal bovine serum (FBS) was obtained from Mediatech, Inc. (Woodland, CA, USA). 12 mm dishes were obtained from Thermo Scientific (Rochester, NY, USA), phosphate buffered saline (PBS) was purchased from Corning (Corning, NY, USA), and DAPI solution was purchased from Invitrogen, Thermo Scientific (Waltham, MA, USA). Western blot polyacrylamide 7.5% gels and nitrocellulose membranes were purchased from BIO-RAD (Hercules, CA, USA); Odyssey tri buffered saline (TBS) blocking buffer and secondary IRDye800CW Goat-Anti Rabbit IgG fluorescent antibody were purchased from LI-COR Biosciences (Lincoln, NE, USA). Primary anti-CD44 antibody was purchased from Abcam (Waltham, MA, USA) and primary GAPDH antibody was purchased form Cell Signaling Technologies (Danvers, MA, USA).

Preparation of Surface-grafted sCy5 Silica Nanoparticles (sCy5-SiNPs-L, -M, -H)

Surface-grafted silica nanoparticles were synthesized by modifications to the Stöber method using tetraethyl orthosilicate (TEOS) as the alkoxide precursor[19, 25]. First, sCy5-amine was conjugated to 3-triethoxysiylpropyl succinic anhydride (TSPA) for 24 h at rt in the dark, yielding sCy5-TSPA. During the next step, TEOS was mixed with the sCy5-TSPA conjugates at a molar ratio of 1.2: 2.5, 5, or 10 (TEOS:sCy5-TSPA) to undergo hydrolysis followed by the condensation reaction step. Three different reaction concentrations of sCy5-TSPA, including 2.5 (low, L), 5.0 (medium, M), and 10 μg/ml (high, H) were used to achieve the different grafting ratios. The reactions were allowed to proceed with 10 mM chloride-ammonium hydroxide buffer (pH 9.0) for 24 h at 50 ^{o}C in the dark. The resulting nanoparticles, sCy5-SiNPs-L, sCy5-SiNPs-M, and sCy5-SiNPs-H, respectively, were washed with water (10 ml x 4 times) and concentrated using Amicon centrifugal filters (10 kDa MWCO).

Preparation of sCy5-incorporated silica nanoparticles, SiNP(sCy5)

sCy5-incorporated silica NPs were synthesized via a multistep procedure. First, sCy5-NHS was conjugated to APTES. The coupling procedure was adapted from literature[19, 25]. Briefly, 1.9 mg (0.0018 mmol) of dye was dissolved in 500 μl of anhydrous DMSO and APTES was added at a molar ratio of 1.2:1 APTES:dye. The reaction was allowed to proceed for 24 h at rt in the dark, which yielded sCy5-APTES as a product. The conjugate (≈5 mg/ml stock) was stored at -20^{o}C until further use. The silica condensation reaction proceeded with ammonium buffer in the presence of TEOS. Fluorescent silica nanoparticles were synthesized by a modified Stöber method. For synthesis, 10 mM ammonium chloride-ammonium hydroxide buffer (pH 9.0) was heated to 50^{o}C, and the corresponding amount of sCy5-APTES conjugate was added. This was allowed to stir for

30 min followed by the addition of TEOS and cyclohexane. The reaction mixture was vigorously stirred to mix the organic and inorganic layers to form an emulsion. The reaction was allowed to continue for 24 h. After cooling to rt, the mixture re-separated into an organic (top) and an aqueous (bottom) layer. The aqueous layer that contained the silica nanoparticles was collected, washed with water, and concentrated using Amicon centrifugal filters (10 kDa MWCO).

Preparation of surface-modified fluorescent silica nanoparticles, SiNP(sCy5)-APTES

Surface modification of the dye-incorporated silica nanoparticles was completed with APTES. The silica nanoparticle emulsion was continuously stirred while an equal volume of toluene was added. The mixture was stirred with gentle vortexing, and centrifuged (10,000 rpm; 30 min). Collected silica nanoparticles were re-dispersed in toluene and heated with 10 equiv. excess of APTES under reflux for 2 h. Particles were collected by centrifugation (10,000 rpm; 5 min), washed thrice with ethanol and re-dispersed in water.

Hyaluronic acid surface-coated silica nanoparticles, SiNP(sCy5)-HA

The surface of the amino-functionalized nanoparticles was further coated with hyaluronic acid through electrostatic interaction. Hyaluronic acid stock solution (0.5 mg/ml) was prepared in HEPES buffer. Silica nanoparticles were re-dispersed in hyaluronic acid solution (1.2 weight percent) and kept overnight at rt under mild agitation. Coated silica nanoparticles were then collected by centrifugation (10,000 rpm; 1 h), rinsed with water and re-dispersed at the desired concentration for analysis.

Nanoparticle characterization

Nanoparticle hydrodynamic diameter, polydispersity, and zeta-potential were measured for silica-based nanoparticles at a concentration of 2 mg/ml using a Malvern Panalytical Zetasizer Nano ZS90 instrument (Malvern, United Kingdom). The sample absorption and emission

properties were performed on the Thermo Fisher Scientific Evolution 220 UV-Visible Spectrophotometer (Waltham, MA, USA) and a Horiba Scientific FluoroMax-4 (Edison, NJ, USA), respectively.

Cell culture, western blot analysis, and cell labeling study

MDA-MB-231 cells that overexpress CD44, and BT-474 cells that do not express CD44 receptors, were grown in RPMI 1640 media supplemented with 10% fetal bovine serum and 1% penicillin-streptomycin at 37°C and 4.5% CO_2. MDA-MB-231 and BT-474 cells were lysed with a RIPA buffer that was supplemented with Halt protease inhibitor, and a Bradford assay was used to determine protein concentration for western blot loading. 20 μg of cell protein were separated on a 7.5% polyacrylamide gel for 80 min at 90 V and transferred to a nitrocellulose membrane for 80 min at 250 MA, followed by blocking with Odyssey tri buffered saline (TBS)-based blocking buffer for 1 h. The membrane was exposed to CD44 (1:2000) and GAPDH (1:10000) rabbit primary antibodies in TBS blocking buffer overnight at 4°C with rocking. The gel was washed with tris buffered saline with tween (TBST) thrice, followed by incubation with a IRDye800CW Goat-Anti Rabbit IgG fluorescent secondary antibody for 1 h and washed with TBST thrice. The membrane was imaged on the Odyssey M imaging system (LI-COR Biosciences; Lincoln, NE, USA).

MDA-MB-231 ($5x10^4$ cells) and BT-474 ($5x10^4$ cells) were seeded onto 12 mm dishes and left to adhere for 24 h for the cell labeling study. The MDA-MB-231 seeded dishes were then split into two groups, (1) untreated and (2) pretreated with excess of 10 mg/ml hyaluronic acid solution in serum-free RPMI media for 1 hour at 37°C to block the receptors prior to incubation with the nanoparticles as previously described[26]. MDA-MB-231 (untreated and pretreated) and BT-474 cells were washed with phosphate buffered saline (PBS) followed by incubation with 25 μg/ml HA-coated or non-coated nanoparticles or free dye at equivalent

concentration for 2 h at 37°C. Cells were washed once with PBS and fixed by adding 4% paraformaldehyde in PBS, pH 6, to each dish for 15 min at 37°C, washed thrice with PBS, and permeabilized with 0.1% Triton for 10 minutes at room temperature. The cells were washed thrice with PBS, followed by a 3 min incubation with 300 nM DAPI solution, followed by three PBS washing steps. Cells were then imaged in PBS on an Olympus IX73 inverted Fluorescent Microscope (Olympus Life Sciences; Waltham, MA, USA) utilizing the brightfield, DAPI, and Cy5.5 fluorescence channels through a xenon lamp excitation source.

Microscopy Image Analysis

A|e-UV-Vis-IR Spectral Sofware (Version 2.2, 2007 Free Software Foundation, INC.) was used to measure the relative quantum yield values of the surface-grafted conjugates. FIJI software (Version 1.53v; National Institutes of Health; Bethesda, Maryland, USA) was used to merge the brightfield and fluorescent images. The FIJI software was also used to create ROIs of each cell to quantify the fluorescence intensity of the nanoparticle conjugates within the cells. The resulting values were plotted and used to calculate the corrected total cell fluorescence *(CTCF) = Integrated Density – (Area of selected cell X Mean fluorescence of background readings*)[27, 28]. These calculated values were plotted, and statistical analysis was preformed using the GraphPad Prism software version 9.1.2 (GraphPad Software, San Diego, CA). A one-way ANOVA was used to determine significance followed by Tukey's test for multiple comparisons, p-values < 0.05 were considered significantly different.

Results and discussion

Synthesis and characterization of surface-grafted fluorescent silica nanoparticles (sCy5-SiNPs)

A modified Stöber method was used to create fluorescent silica nanoparticles by grafting the cyanine dye to the surface of the nanoparticles (**Scheme 1**). The Stöber method is often used

to create uniformly sized silica nanoparticles through a process of hydrolysis and condensation reactions. This method involves the use of TEOS, an alkoxide derivative, as the precursor by converting the TEOS ethyl groups to hydroxyl groups through hydrolysis. This process is followed by the condensation reaction of the silanol groups in the presence of an ammonium buffer to create the silica nanoparticles. sCy5-SiNPs nanoparticles were synthesized by first conjugating the cyanine dye with TSPA and then undergoing hydrolysis in the presence of TEOS molecules, followed by a series of condensation reactions to form fluorescent silica nanoparticles.

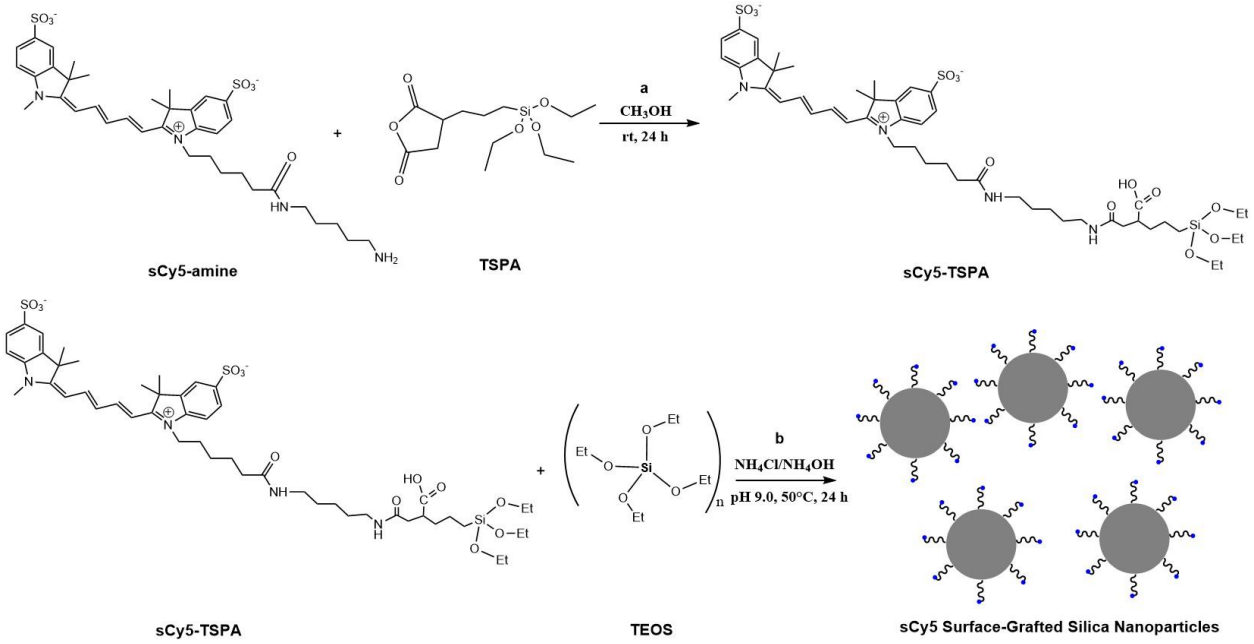

Scheme 1. Synthesis of sCy5 dye-grafted silica nanoparticles with three dye amounts (low, medium, and high). Conditions: conjugation: (**a**) methanol, 24 h at rt in the dark; (**b**) hydrolysis and condensation: molar ratio of 1.2: 2.5, 5, or 10 (TEOS: sCy5-TSPA), reactions proceeded with 10 mM chloride-ammonium hydroxide buffer, pH 9.0, 50°C, 24 hours.

One of the main goals of this first step was to determine the optimal grafting density of the dye for the highest emission intensity. Various molar ratios of sCy5-TSPA:TEOS (2.5, 5, and 10 μg/ml) were used, leading to different degrees of dye grafting (low (L), medium (M), and high (H)). The grafting efficiency was assessed by photometrically quantifying the content of the dye on the surface of the nanoparticles in the resulting products (**Table 2**). It was found that the

reaction efficiency decreases with the increase of the dye:TEOS ratio, thus further increase of the initial concentration of the dye is unlikely to result in a higher grafting density. **Figure 15** and **Table 3** represent the results of HD and zeta-potential characterization of the surface-grafted nanoparticles. The synthesis produced nanoparticles with HDs in the range of 25-35 nm. Their zeta potential was around -20 mV potential suggesting that these nanoparticles are stable in solution, which is consistent with the literature[29-31] and corresponds to the

presence of the hydroxyl groups on the nanoparticle's surface. As the amount of the dye on the nanoparticle's surface increases, a slight increase in size was observed.

Nanoparticles	**Dye Concentration (µg/ml)**	**Percent Reaction Efficiency**	**Relative Quantum Yield**
SiNPs(sCy5)-L	0.189	7.5%	1
SiNPs(sCy5)-M	0.217	4.3%	1.05
SiNPs(sCy5)-H	0.314	1.3%	1.39

Table 2. Grafting efficiency of sCy5-SiNPs

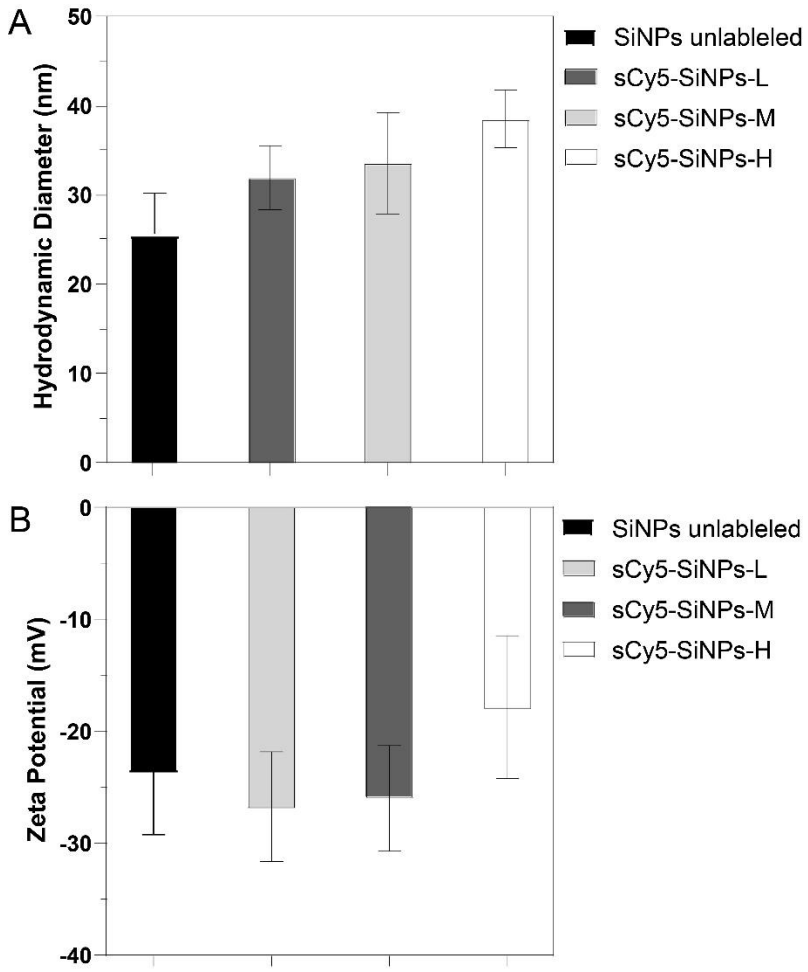

Figure 15. (A) Hydrodynamic diameter and (B) zeta-potential of sCy5 surface-grafted silica nanoparticles.

Nanoparticles	Hydrodynamic Diameter, nm	PDI	Zeta-potential, mV
SiNPs unlabeled	25.5 ± 4.6	0.22	-23.7 ± 5.5
SiNPs(sCy5)-L	31.8 ± 3.6	0.17	-27 ± 4.9
SiNPs(sCy5)-M	33.5 ± 5.6	0.20	-25.9 ± 4.7
SiNPs(sCy5)-H	38.5 ± 33	0.23	-17.9 ± 6.4

Table 3. Characterization of sCy5-SiNPs nanoparticles, C = 2 mg/ml, pH = 7.8.

The optical properties of the surface-grafted nanoparticles were evaluated (**Figure 16**). It can be noted that the absorption and fluorescence spectra of all three samples are similar and correspond to the absorption and emission of sCy5, confirming that the dye molecules were attached to the surface of the silica nanoparticles. The fluorescence intensity increases as the surface-grafted dye contents increased. This suggests that the non-radiative deactivation processes caused by the proximity of the dye molecules are not prevailing at these grafting densities, and the derivative with the highest dye content on the surface of the nanoparticles could be used on the next step of the project.

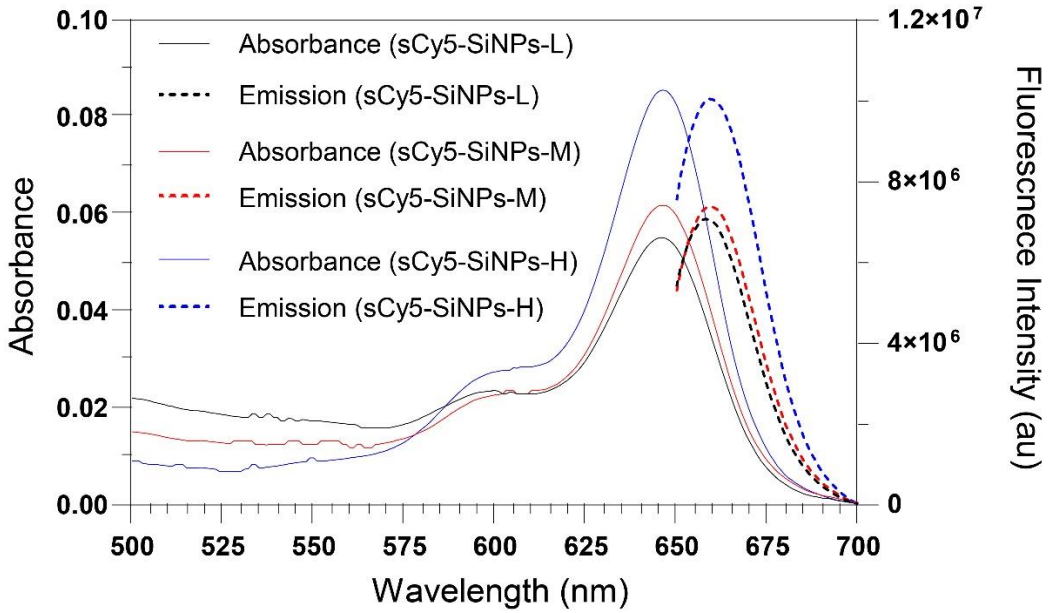

Figure 16. Absorbance and fluorescence emission spectra of the surface-grafted silica nanoparticles (λ_{ex} = 640 nm).

Synthesis and characterization of dye-incorporated silica nanoparticles, SiNPs(sCy5)

In order to further functionalize the nanoparticles with targeting ligands, the surface has to be available for this modification, and thus preferably not be occupied by the attached dye. For this reason, instead of grafting the dye onto the surface, we transitioned to the core-shell architecture of the nanoparticles. Stability is crucial in the development of fluorescent probes for use in bioimaging application, and this approach can also provide some protection for the dye

from potential environmental factors, such as photobleaching in the presence of oxygen[15, 32]. Cyanine dye molecules were conjugated to APTES to form a fluorescent sCy5-APTES conjugate (**Scheme 2**). APTES molecules possess the necessary silane groups that will undergo hydrolysis and condensation. These reactions formed the fluorescent nanoparticles with the cyanine dye molecules incorporated into the silica matrix. The addition of TEOS to the reaction created a silica shell that surrounds the fluorescent silica core. This TEOS silica shell allows for hydroxyl groups to be present on the surface so that further surface modifications can be performed.

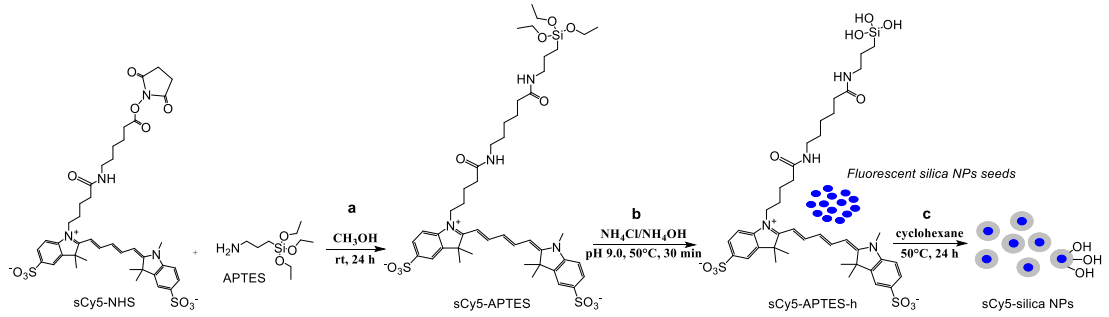

Scheme 2. Synthesis of cyanine dye-incorporated silica nanoparticles. Conditions: (a) conjugation: molar ratio of 1.2:1 (APTES:dye), methanol, rt, 24 h in the dark; (b) hydrolysis and condensation: 10 mM chloride-ammonium hydroxide buffer, pH 9.0, 50ºC, 30 min; (c) condensation and stabilization: TEOS, cyclohexane, 50ºC, 24 h.

Silica nanoparticles present opportunities for modifications to the surface with various functional groups including amines (-NH_2), thiols (-SH) or carboxylic (-COOH) groups[14, 33-36]. These surface modifications can enable attachment of the targeting ligands. In this study, amino-modified silica nanoparticles were produced with APTES molecules. APTES was reacted with the hydroxyl groups of the TEOS, producing the amino-modified silica nanoparticles (**Scheme 3**). This addition of APTES to the surface caused the zeta potential to change from approximately -20 mV to almost 30 mV as a response to protonation of the amino groups (**Figures 17 B-D** and **Tables 4-5**). Both dye-free and dye-incorporated silica nanoparticles showed the same surface charge behavior upon reaction with APTES. The size of the silica nanoparticles slightly increased after the reaction, suggesting the addition of another layer to the particles. On the next step, the

nanoparticles' surface was coated with hyaluronic acid (**Scheme 3**). Some of the hydroxylic and carboxylic groups of the latter are dissociated in aqueous solutions, and the effective negative charge helps the process through the electrostatic interaction with the positively-charged amines. This is demonstrated by the change of the zeta potential from ~30 mV to approximately -5 mV after coating with HA (**Figure 17 B and D and Tables 4-5)**. A larger negative zeta potential value observed for the non-coated SiNPs is attributed to the abundance of the hydroxylic groups on the silica surface prior to APTES modification. As in case of the dye-grafted nanoparticles, these core-shell structures showed a slight increase of their size after each step of the surface modification (**Figure 17 A-C and Tables 4-5**) and the polydispersity values are found to be at or below 0.2, which is in the acceptable range for polymer-based nanoparticle materials (**Tables 4-5)**[37].

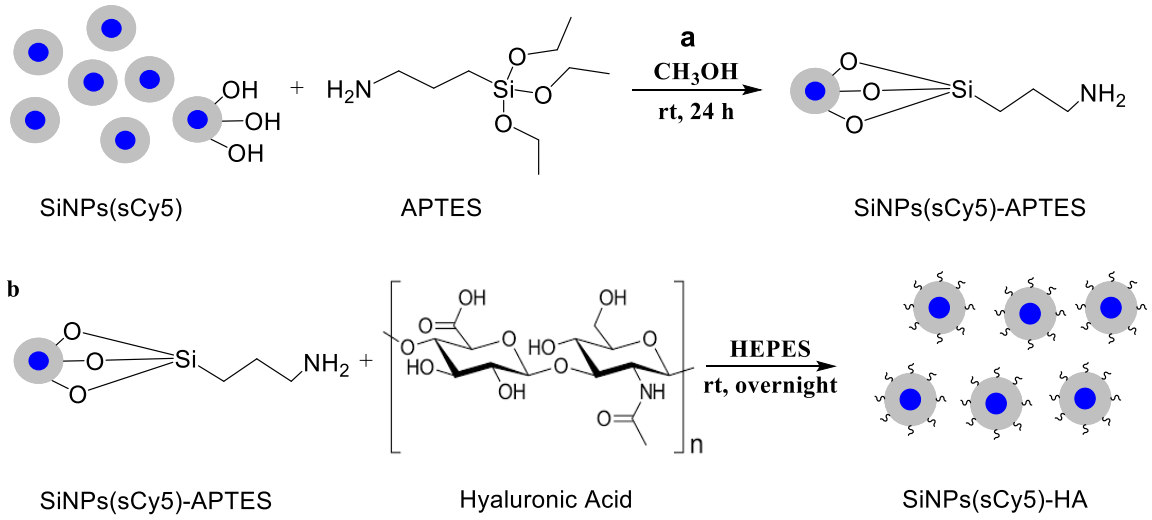

Scheme 3. Surface modification of cyanine dye-incorporated silica nanoparticles. Conditions: (a) condensation by addition of 10 eq excess APTES under reflux for 2 hours. (b) Redispersed in 0.5 mg/ml hyaluronic acid aqueous solution (1.2 wt% in HEPES buffer overnight at rt).

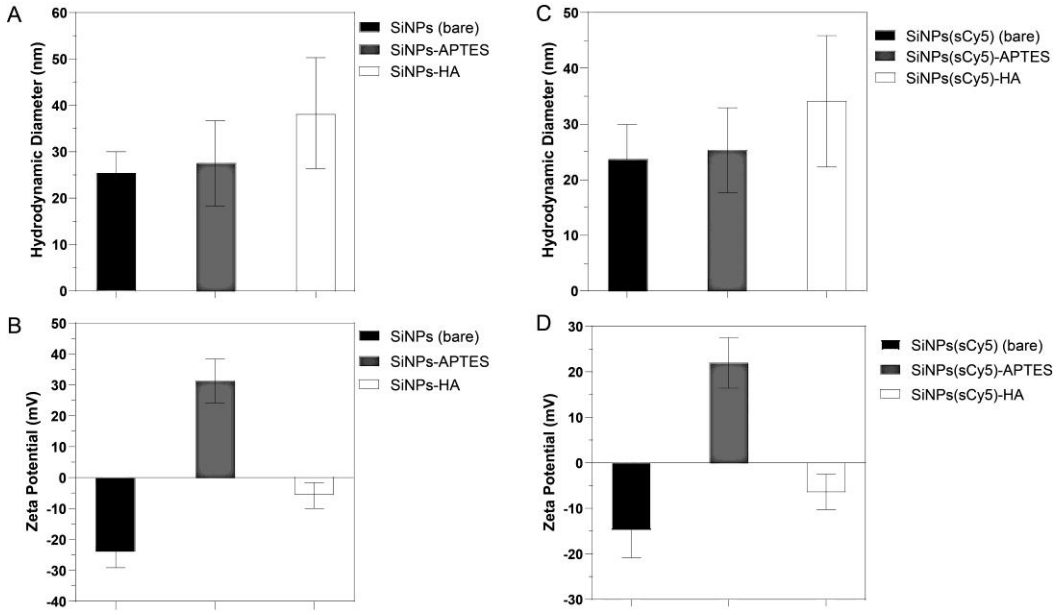

Figure 17. Hydrodynamic diameter (A) and zeta-potential (B) of the dye-free SiNPs before and after the surface modification. Hydrodynamic diameter (C) and zeta-potential (D) of sCy5 dye-incorporated nanoparticles before and after surface modifications.

Non-labeled nanoparticles	**Hydrodynamic Diameter, nm**	**PDI**	**Zeta-potential, mV**
SiNPs	25.5 ± 4.6	0.22	-23.7 ± 5.5
SiNPs-APTES	27.5 ± 9.1	0.16	31.4 ± 7.1
SiNPs-HA	38.3 ± 11.9	0.07	-5.6 ± 4.2

Table 4. Characterization of non-labeled SiNPs, C = 2 mg/ml, pH = 7.8

sCy5 labeled nanoparticles	**Hydrodynamic Diameter, nm**	**PDI**	**Zeta-potential, mV**
SiNPs(sCy5)	23.8 ± 6.1	0.04	-14.8 ± 5.9
SiNPs(sCy5)-APTES	25.4 ± 7.7	0.15	26.4 ± 5.5
SiNPs(sCy5)-HA	34.1 ± 11.8	0.08	-4.3 ± 3.9

Table 5. Characterizations of SiNPs(sCy5) nanoparticles, C = 2 mg/ml, pH = 7.8.

Spectral measurements were performed for both the uncoated and hyaluronic acid-coated nanoparticles to confirm the presence of the dye and the origin of the fluorescence emission (**Figure 18**). The absorbance spectra were recorded first, but the peak of the dye's absorption was covered by the strong scattering signal. In order to reconstruct the absorbance spectra, fluorescence excitation spectra of the nanoparticles were measured, and the observed maximum matched very well the maximum absorption of the sCy5. The fluorescence spectra also demonstrated an emission peak around 645 nm, consistent with the sCy5. These fluorescent properties confirmed the presence of the cyanine dye in the core of the silica nanoparticles.

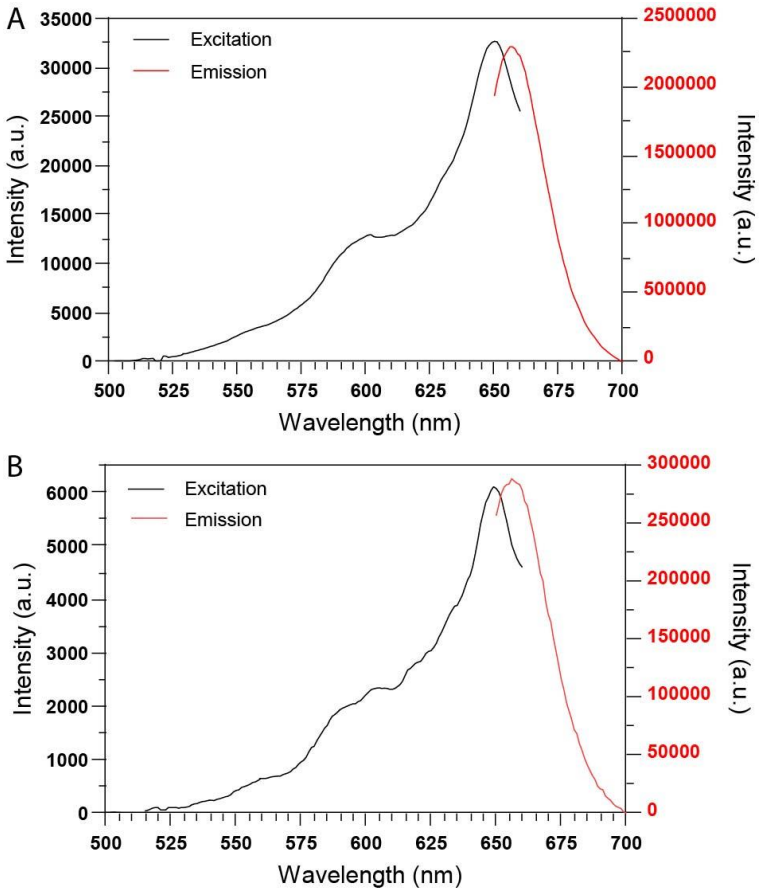

Figure 18. Fluorescence excitation and emission spectra of the dye-incorporated silica nanoparticles. (A) SiNPs(sCy5)-HA and (B) SiNPs(sCy5).

To assess the core-shell HA-coated nanoparticles targeting ability, their binding to the surface receptor, CD44, was evaluated using CD44+ (MDA-MB-231) and CD44- (BT-474) cells. First, the expression level of CD44 in these cell lines was confirmed by a Western blot. MDA-MB-231 cells were confirmed to have CD44 protein present, whereas the BT-474 cells showed no expression of CD44 (**Figure 19**). Additionally, a subgroup of MDA-MB-231 cells were pre-treated with hyaluronic acid to saturate the surface receptors, which can inhibit the CD44 binding by the HA-coated nanoparticles[26]. Similarly, Yang *et al.* investigated folate-modified fluorescent silica nanoparticles' affinity to the folate receptors. A six-fold increase of binding to the folate-positive cells was observed, while binding decreased when the cells were pre-incubated with excess of folate[10]. The hyaluronic acid pre-treated subgroup served as an additional negative control in the binding studies, along with the CD44- BT-474 cell line. The binding of the nanoparticles to CD44 was evaluated in fluorescence microscopy images of the cells incubated with the HA-coated fluorescent silica nanoparticles, as well as with the non-coated negative control (**Figure 20**).

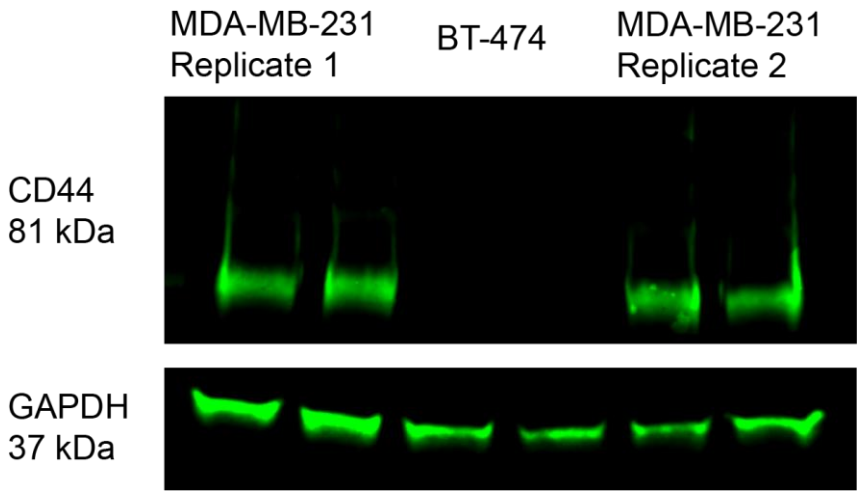

Figure 19. Western blot confirmation of CD44 protein presence in MDA-MB-231 (CD44+) and BT-474 (CD44-) cell lines. GAPDH was used as the internal control.

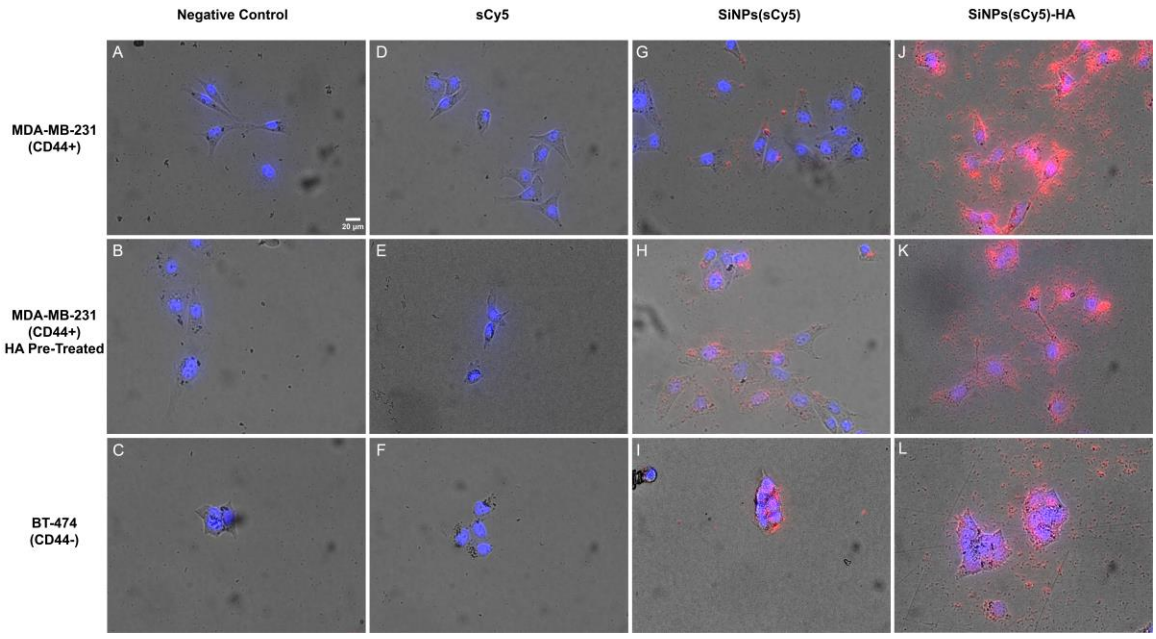

Figure 20. Representative fluorescence micrographs of MDA-MB-231 and BT-474 cell lines with HA-coated and uncoated SiNPs(sCy5) and controls. (**A-C**) Negative control; (**D-F**) sCy5 only; (**G-I**) SiNPs(sCy5); and (**J-L**) SiNPs(sCy5)-HA. Scale bars represent 20 µm.

Examining the fluorescence intensity from the fluorescent micrographs, the binding interaction of the HA-coated nanoparticles to CD44 can be assessed. There was no sCy5 emission detected in the fields with cells that were incubated with sCy5 only (**Figure 20 D-F**). The same lack of signal was observed in the negative control group, where cells were not incubated with sCy5 or the fluorescent nanoparticles (**Figure 20 A-C**). This observation suggests that the free dye does not show any preferential binding to the cells used in the experiment. At the same time, the fluorescent signal appeared visually stronger from the SiNPs(sCy5)-HA nanoparticles incubated with the MDA-MB-231 cells (**Figure 20 J**). Comparison with the images in **Figure 20 J-L** suggests higher accumulation of the HA-coated nanoparticles was achieved in the CD44+ cells compared to the CD44- cells. sCy5 fluorescence, was also observed in cells that were incubated with uncoated fluorescent nanoparticles (**Figure 20 G-I**), which is likely due to non-specific internalization mechanisms[38].

Calculating the average cell fluorescence intensity provides a quantitative measure of the interaction between HA-coated nanoparticles and CD44+ cells. The CTCF equation can be used to calculate the average fluorescence intensity of the cells of the regions of interest (ROIs) that are manually defined on the fluorescence micrographs[27, 28] (**Figure 21**). The calculated average fluorescence intensities suggest that the SiNPs(sCy5)-HA shows greater interaction to CD44+ ($2.43 \times 10^5 \pm 0.98 \times 10^5$) and CD44+ pre-treated ($2.96 \times 10^5 \pm 1.27 \times 10^5$) cells and a lower interaction with the CD44- cells ($0.36 \times 10^5 \pm 0.58 \times 10^5$). This trend was confirmed to be statistically significant in both CD44+ ($4.90(2,33) = 31.07$, $p < 0.0001$) and CD44+ pre-treated ($4.90(2,33) = 31.07$, $p < 0.0001$) cells when compared to CD44- cells. However, no statistically significant difference was observed between the CD44+ and CD44+ pre-treated cells ($4.90(2,33) = 31.07$, $p = 0.36$). These results suggest that the HA coating increases the ability of these nanoparticles to target CD44+ cells.

However, when examining the uncoated nanoparticles, the calculated cell fluorescent intensities suggest similar interactions on the CD44+ ($2.04 \times 10^5 \pm 1.56 \times 10^5$), CD44+ pre-treated ($1.68 \times 10^5 \pm 1.25 \times 10^5$) and CD44- ($2.45 \times 10^5 \pm 0.54 \times 10^5$) cell lines. This suggestion is supported by a statistical analysis of the values, which indicated that there was no significant difference in the interactions of the uncoated nanoparticles with any of the cell lines. Specifically comparing the interactions with CD44+ cells and CD44- cells ($2.1(2,32) = 0.81$, $p = 0.75$) yielded no significant difference. Comparing the interactions with CD44+ pre-treated cells and CD44- cells ($2.1(2,32) = 0.81$, $p = 0.80$) also yielded no significant difference. Finally, comparing the interactions with CD44+ cells and CD44+ pre-treated cells ($2.1(2,32) = 0.80$, $p = 0.44$) indicated no significant difference. This observation suggests that the uncoated silica nanoparticles do not have any increased ability to target CD44+ over CD44- cells. Further analysis can be utilized to compare the interactions that coated and non-coated nanoparticle groups across the same cell lines. A statistically significant difference was not observed between the CD44+ cells incubated

with either group of nanoparticles (6.33(3,43) = 12.27, p = 0.73). However, a statistically significant difference was observed between the CD44- cells incubated with each group of nanoparticles (6.33(3,43) = 12.27, p = 0.007). These results suggest that different internalization mechanisms may play a role between the nanoparticles. Biomolecules with a stronger interaction with a cell surface receptor can have higher internalization rates through receptor-mediated endocytosis. The fluorescent signal presence in SiNPs(sCy5)-HA incubated with the CD44- cells, and SiNPs(sCy5) with all three cell groups, could be explained by uptake by nonspecific endocytosis mechanisms, such as phagocytosis or pinocytosis. These mechanisms allow for "bystander" molecules to be internalized into cells[39].

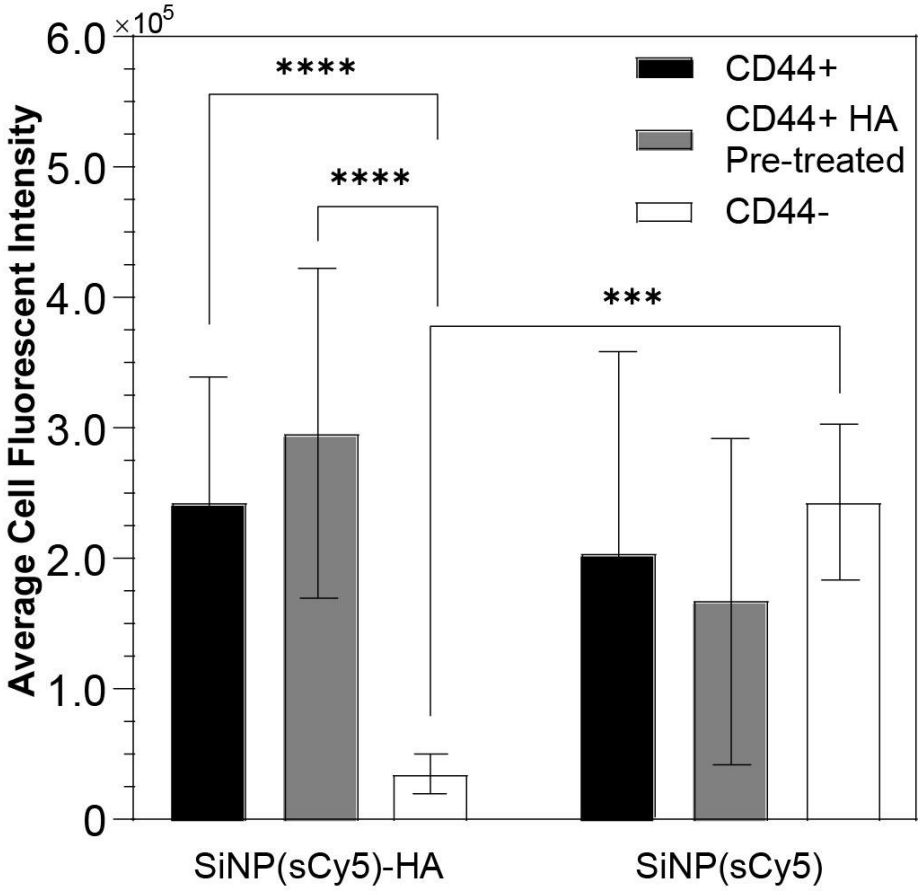

Figure 21. CTCF imaging data of SiNP(sCy5)-HA and SiNPs(sCy5) in CD44+, CD44+ cells pre-treated with HA, and CD44- cells. **** $p < 0.0001$, *** $p < 0.001$.

Conclusions

The sCy5 dye-incorporated fluorescent silica nanoparticles synthesized by a modified Stöber method produced small uniform nanoparticles. Their ability for further surface modifications to target specific receptors was illustrated by coating the fluorescent nanoparticles with a well-known CD44-targeting moiety – hyaluronic acid. The results suggest that HA-coated fluorescent silica nanoparticles demonstrate an increased interaction with the CD44 protein and show stronger internalization into cells with overexpressed CD44 receptors in comparison with the cells where CD44 is not expressed. Non-coated nanoparticles demonstrated interaction, without much notable difference between the cell groups.

Bibliography

1. Aithal, P., Nanotechnology Innovations & Business Opportunities: A Review. *Int. J. Manag., IT Eng.* **2016**, *6* (1), 182-204.

2. Miernicki, M.; Hofmann, T.; Eisenberger, I., et al., Legal and Practical Challenges in Classifying Nanomaterials According to Regulatory Definitions. *Nat. Nanotechnol.* **2019**, *14* (3), 208-216.

3. Oliveira, L. F. d.; Bouchmella, K.; Picco, A. S., et al., Tailored Silica Nanoparticles Surface to Increase Drug Load and Enhance Bactericidal Response. *J. Braz. Chem. Soc.* **2017**, *28*, 1715-1724.

4. Lee, J. E.; Lee, N.; Kim, H., et al., Uniform Mesoporous Dye-Doped Silica Nanoparticles Decorated with Multiple Magnetite Nanocrystals for Simultaneous Enhanced Magnetic Resonance Imaging, Fluorescence Imaging, and Drug Delivery. *J. Am. Chem. Soc.* **2010**, *132* (2), 552-557.

5. Tu, H. L.; Lin, Y. S.; Lin, H. Y., et al., In Vitro Studies of Functionalized Mesoporous Silica Nanoparticles for Photodynamic Therapy. *Adv. Mater.* **2009**, *21* (2), 172-177.

6. Kim, J.; Lee, J. E.; Lee, J., et al., Generalized Fabrication of Multifunctional Nanoparticle Assemblies on Silica Spheres. *Angew. Chem. Int. Ed. Engl.* **2006**, *45* (29), 4789-4793.

7. Lin, Y. S.; Hung, Y.; Lin, H. Y., et al., Photonic Crystals from Monodisperse Lanthanide-Hydroxide-at-Silica Core/Shell Colloidal Spheres. *Adv. Mater.* **2007**, *19* (4), 577-580.

8. Mader, H.; Li, X.; Saleh, S., et al., Fluorescent Silica Nanoparticles. *Ann. N. Y. Acad. Sci.* **2008**, *1130* (1), 218-223.

9. Santiago, A. M.; Ribeiro, T.; Rodrigues, A. S., et al., Multifunctional Hybrid Silica Nanoparticles with a Fluorescent Core and Active Targeting Shell for Fluorescence Imaging Biodiagnostic Applications. *Eur. J. Inorg. Chem.* **2015**, *2015* (27), 4579-4587.

10. Yang, H.; Lou, C.; Xu, M., et al., Investigation of Folate-Conjugated Fluorescent Silica Nanoparticles for Targeting Delivery to Folate Receptor-Positive Tumors and Their Internalization Mechanism. *Int. J. Nanomedicine.* **2011**, *6*, 2023.

11. Ow, H.; Larson, D. R.; Srivastava, M., et al., Bright and Stable Core-Shell Fluorescent Silica Nanoparticles. *Nano Lett.* **2005**, *5* (1), 113-117.

12. Pardo, R.; Zayat, M.; Levy, D., Photochromic Organic–Inorganic Hybrid Materials. *Chem. Soc. Rev.* **2011**, *40* (2), 672-687.

13. Tapec, R.; Zhao, X. J.; Tan, W., Development of Organic Dye-Doped Silica Nanoparticles for Bioanalysis and Biosensors. *J. Nanosci. Nanotechnol.* **2002**, *2* (3-4), 405-409.

14. Gubala, V.; Giovannini, G.; Kunc, F., et al., Dye-Doped Silica Nanoparticles: Synthesis, Surface Chemistry and Bioapplications. *Cancer Nanotechnol.* **2020**, *11* (1), 1-43.

15. Song, X.; Li, F.; Ma, J., et al., Synthesis of Fluorescent Silica Nanoparticles and Their Applications as Fluorescence Probes. *J. Fluoresc.* **2011**, *21* (3), 1205-1212.

16. Miletto, I.; Gilardino, A.; Zamburlin, P., et al., Highly Bright and Photostable Cyanine Dye-Doped Silica Nanoparticles for Optical Imaging: Photophysical Characterization and Cell Tests. *Dyes and Pigments.* **2010**, *84* (1), 121-127.

17. Wang, L.; Zhao, W.; Tan, W., Bioconjugated Silica Nanoparticles: Development and Applications. *Nano Res.* **2008**, *1* (2), 99-115.

18. Svechkarev, D.; Mohs, A. M., Organic Fluorescent Dye-Based Nanomaterials: Advances in the Rational Design for Imaging and Sensing Applications. *Curr. Med. Chem.* **2019**, *26* (21), 4042-4064.

19. Stöber, W.; Fink, A.; Bohn, E., Controlled Growth of Monodisperse Silica Spheres in the Micron Size Range. *J. Colloid Interface Sci.* **1968**, *26* (1), 62-69.

20. Bonacchi, S.; Genovese, D.; Juris, R., et al., Luminescent Silica Nanoparticles: Extending the Frontiers of Brightness. *Angew. Chem. Int. Ed. Engl.* **2011**, *50* (18), 4056-4066.

21. Liu, K.; Wang, Z.-q.; Wang, S.-j., et al., Hyaluronic Acid-Tagged Silica Nanoparticles in Colon Cancer Therapy: Therapeutic Efficacy Evaluation. *Int. J. Nanomed.* **2015**, *10*, 6445.

22. Ohulchanskyy, T. Y.; Roy, I.; Goswami, L. N., et al., Organically Modified Silica Nanoparticles with Covalently Incorporated Photosensitizer for Photodynamic Therapy of Cancer. *Nano Lett.* **2007**, *7* (9), 2835-2842.

23. Karbownik, M. S.; Nowak, J. Z., Hyaluronan: Towards Novel Anti-Cancer Therapeutics. *Pharmacol. Rep.* **2013**, *65* (5), 1056-1074.

24. Cui, X.; Xu, H.; Zhou, S., et al., Evaluation of Angiogenic Activities of Hyaluronan Oligosaccharides of Defined Minimum Size. *Life Sci.* **2009**, *85* (15-16), 573-577.

25. Ibrahim, I. A.; Zikry, A.; Sharaf, M. A., Preparation of Spherical Silica Nanoparticles: Stober Silica. *J. Am. Sci.* **2010**, *6* (11), 985-989.

26. Ganesh, S.; Iyer, A. K.; Morrissey, D. V., et al., Hyaluronic Acid Based Self-Assembling Nanosystems for Cd44 Target Mediated Sirna Delivery to Solid Tumors. *Biomaterials.* **2013**, *34* (13), 3489-3502.

27. McCloy, R. A.; Rogers, S.; Caldon, C. E., et al., Partial Inhibition of Cdk1 in G2 Phase Overrides the Sac and Decouples Mitotic Events. *Cell Cycle.* **2014**, *13* (9), 1400-1412.

28. Burgess, A.; Vigneron, S.; Brioudes, E., et al., Loss of Human Greatwall Results in G2 Arrest and Multiple Mitotic Defects Due to Deregulation of the Cyclin B-Cdc2/Pp2a Balance. *Proc. Natl. Acad. Sci.* **2010**, *107* (28), 12564-12569.

29. Shnoudeh, A. J.; Hamad, I.; Abdo, R. W., et al., Synthesis, Characterization, and Applications of Metal Nanoparticles. *J. Biomaterial. Bionanotechnol.,* Elsevier: **2019**; pp 527-612.

30. Sapsford, K. E.; Tyner, K. M.; Dair, B. J., et al., Analyzing Nanomaterial Bioconjugates: A Review of Current and Emerging Purification and Characterization Techniques. *Anal. Chem.* **2011**, *83* (12), 4453-4488.

31. Horie, M.; Fujita, K., Toxicity of Metal Oxides Nanoparticles. *Adv. Mol. Toxicol.,* Elsevier: **2011**; Vol. 5, pp 145-178.

32. Shirai, S.; Kido, J., Fabrication of Multi Color Polymer El Devices Using the Photo-Bleaching Method. *J. Photopolym. Sci. Tech.* **2001**, *14* (2), 317-322.

33. Claesson, E. M.; Philipse, A. P., Thiol-Functionalized Silica Colloids, Grains, and Membranes for Irreversible Adsorption of Metal (Oxide) Nanoparticles. *Colloids Surf. A Physicochem. Eng. Asp.* **2007**, *297* (1-3), 46-54.

34. Zhang, Q.; Huang, R.; Guo, L.-H., One-Step and High-Density Protein Immobilization on Epoxysilane-Modified Silica Nanoparticles. *Sci. Bull.* **2009**, *54* (15), 2620-2626.

35. Bagwe, R. P.; Hilliard, L. R.; Tan, W., Surface Modification of Silica Nanoparticles to Reduce Aggregation and Nonspecific Binding. *Langmuir.* **2006**, *22* (9), 4357-4362.

36. Rossi, L. M.; Shi, L.; Quina, F. H., et al., Stöber Synthesis of Monodispersed Luminescent Silica Nanoparticles for Bioanalytical Assays. *Langmuir.* **2005**, *21* (10), 4277-4280.

37. Danaei, M.; Dehghankhold, M.; Ataei, S., et al., Impact of Particle Size and Polydispersity Index on the Clinical Applications of Lipidic Nanocarrier Systems. *Pharmaceutics.* **2018**, *10* (2), 57.

38. Behzadi, S.; Serpooshan, V.; Tao, W., et al., Cellular Uptake of Nanoparticles: Journey Inside the Cell. *Chem. Soc. Rev.* **2017**, *46* (14), 4218-4244.

39. Li, Y.-X.; Pang, H.-B., Macropinocytosis as a Cell Entry Route for Peptide-Functionalized and Bystander Nanoparticles. *J. Controlled Release.* **2021**, *329*, 1222-1230.

CHAPTER 6: CONCLUSIONS AND FUTURE DIRECTIONS

Intraoperative Nerve Imaging

In summary, fluorescent imaging tools can provide surgeons with a way to supplement their skills and expertise in the intraoperative setting and help them precisely maneuver surgical instruments. Many diseases, especially cancer, conceal the location of nerves and other vital small anatomical structures which causes difficulties for surgeons during surgical procedures. Therefore, there is a large unmet need for intraoperative guidance that improves the visualization of these vital anatomical structures. Lacking the ability to visualize nerve structures may lead to unintentional and consequential nerve damage resulting in chronic pain and the loss of nerve function. These consequences can be severe even if just one nerve is damaged. For instance, the facial nerve is responsible for the function of the multitude of facial expressions and movements. Intraoperative visualization of this single nerve structure would reduce the risk of nerve damage and paralysis, which could otherwise severely impact a patient's quality of life.

The ability of Nervelight™ to target nerve tissue would enable visualization of hidden at-risk nerve sites during surgical interventions. The utilization of a nerve protein, NGF, enables targeting to nerves, since NGF is highly expressed in neuronal growth and survival. Nervelight™ was observed to fluorescently label the facial nerve, providing the ability to visualize this nerve site intraoperatively. The Nervelight™ fluorescent signal was observed to co-occur at the TrkA receptors on excised nerve sections. In contrast, the unmodified control dye signal was not present, providing further evidence of nerve targeting of Nervelight™. The Nervelight™ complex was also observed to have a strong interaction to the facial nerve branches, providing convincing data to further explore Nervelight™ as a potential imaging guidance tool to aid surgeons in reducing the risk of nerve damage.

The Nervelight™ capacity to target facial nerves provided evidence that this contrast agent can fluorescently label facial nerves. The functionality of this contrast agent can determine

the targeting at high-risk nerve sites in the presence of a cancer disease model. A cancer model can be used to test clinical procedures that would require the careful maneuvering of surgical tools around nerve structures. Parotidectomies are common procedures that involve cancer within the parotid gland, where the facial nerve divides the gland into two parts. This division of the parotid gland puts the facial nerve at high risk of unintentional damage during parotidectomies. Evaluating the ability of Nervelight™ to target and label the facial nerve hidden within the cancerous tissue would enable further evidence of the Nervelight™ contrast agent to target these at-risk nerve sites.

Using a contrast agent to label a nerve in order to avoid damage to that nerve while simultaneously targeting a cancerous tumor with a separate contrast agent can be challenging. Designing contrast agents to target specific tissue with different NIR wavelength fluorescent dyes can be advantageous to achieve both of these goals during oncological procedures. A key feature of the Curadel Lab FLARE™ imaging system is that it houses a dual NIR channel system that could enable future development of multiple tissue-specific contrast agents to be utilized in the same surgical procedure[1]. In the case of parotidectomies, it would be feasible to use image-guided surgery instruments like the Lab FLARE™ to develop a dual NIR contrast agent to label nerve sites such as the facial nerve while labeling tumor tissue at a different fluorescence. The development of nerve-specific agents is critical to identify nerves during surgical intervention and becomes even more applicable with the potential for those agents to be used in conjunction with a tumor-specific fluorescent agent.

Surface Modified Silica Nanoparticles

In summary, silica nanoparticles are promising candidates for use as nanotechnology-based platforms in bioimaging applications. The Stöber method is a well-known synthesis technique to form silica nanoparticles. Modifications to the method allow for the integration of dye molecules or other biomolecules into the silica platform for specific targeting. Using the

Stober method, relatively small nanoparticles (25 nm to 45 nm) were formed with a cyanine dye (Sulfo-Cyannine5 Amine) incorporated into the silica matrix. These fluorescent nanoparticles were modified at the surface with the addition of unmodified APTES molecules producing positively charged NH_2 groups on the surface. These positively charged amino groups enabled a hyaluronic acid coating to be added to the nanoparticles via electrostatic interaction. This additional surface modification of a hyaluronic acid coating allows for targeting CD44 receptors, which have been found to be upregulated on cancer cells. Evaluating the zeta potential of the modified nanoparticles provided evidence of successful modification as the zeta potential was observed to be highly positive with the addition of the amino groups and subsequently slightly negative with the addition of the hyaluronic acid coating. Fluorescent microscopy suggested higher interaction of the HA-coated nanoparticles on CD44+ cells. Furthermore, when CD44+ were pre-treated with excess hyaluronic acid, a lower fluorescent signal was observed with the HA-coated nanoparticles. The non-coated nanoparticles incubation was observed to have no significant difference between the CD44+ and CD44- cell lines, suggesting low interaction with CD44 receptors.

To confirm the suggested higher affinity of the HA-coated nanoparticles on CD44+ cells, further experimental studies would need to be conducted. Fluorescent Activated Cell Sorting (FACS) flow cytometry can be utilized as a cell sorting technique, enabling cell populations to be separated[2, 3]. By separating the cell populations, it would be possible to determine the percent of cells with internalized nanoparticle. Results would be characterized by fluorescent microscopy data showing that the HA-coated nanoparticles present in significantly higher quantities in the CD44+ cell population and lower quantities in the pre-treated CD44+ and CD44- cell populations. To determine the internalization mechanism of the HA-coated and non-coated nanoparticle systems entering cells, inhibition experiments can be conducted to block the different endocytosis pathways. First, the anti-CD44 antibody can inhibit nanoparticle binding to

cell CD44 receptors, confirming whether the HA-coated nanoparticles are being internalized by other means[4]. Our results of pre-treating CD44+ cells with excess hyaluronic acid observed a decrease in the interaction of the HA-coated nanoparticles suggesting CD44 interaction is necessary for internalization. By incubating with anti-CD44 antibodies and conducting flow cytometry, the fluorescent microscopy results of receptor-mediated endocytosis would supplement the results already established. Further inhibition studies can evaluate the role other endocytosis mechanisms play in the internalization of these HA-coated and non-coated silica nanoparticles. The CD44+ and CD44- cells can be incubated with various inhibitors to block clathrin-mediated endocytosis (chloropromazine, chloroquine, dynasore, hypertonic sucrose)[5-8], caveolae-mediated endocytosis (nystatin, filipin, and genistein)[5, 8, 9], phagocytosis (phenothiazines, Cytochalasin D, amiloride)[6, 8], and micropinocytosis (Cytochalasin D, amiloride)[5, 6, 8]. Similarly, this series of studies would also be followed by flow cytometry to determine the internalization quantities of the silica nanoparticle systems. The data would provide necessary evidence of the cellular entry of the HA coated nanoparticles on CD44- cells and evidence of the non-coated nanoparticle entry into both CD44+ and CD44- cell lines.

Designing an in vivo experiment to study the efficacy of HA-coated nanoparticles on CD44+ and CD44- cancer tumor models could further indicate targeting capabilities of these nanoparticles. The in vitro cell labeling study suggested that a higher fluorescent signal was observed on the CD44+ cells in comparison with the CD44- cells. The in vivo data could confirm this ability to fluorescently label CD44+ cells and visualize these tumors during surgery. Additional studies could be evaluated for imaging parameters to determine the optimal signal intensity difference between the tumor and the background. At the same time, biodistribution kinetics would provide critical data on the clearance mechanism and identify other tissue the nanoparticle system may impact. Various nanoparticle systems are utilized as delivery systems for therapeutic drugs targeting cancer tumors[10, 11]. The entrapment of therapeutic drugs in the

nanoparticle system can significantly benefit by targeting specific cell types and providing protection in cases of the drug leaking from the nanoparticle. Although the design of nanoparticle systems with entrapped therapeutic drugs requires careful design to ensure healthy tissue is not affected. These additional studies would be instrumental in developing how these nanoparticles would behave in a biological environment.

Carbon-based nanodots for use as a nanomaterial platform

Carbon-based nanodots have emerged with a wide range of uses in the fields of chemistry, physics, and biomedical science[12]. Nanodot surfaces can be chemically modified to enhance cell site targeting and improve the effectiveness of the nanodot platform. Carbon nanodots have extraordinary high levels of solubility, chemical inertness, and biocompatibility while also exhibiting low toxicity and resistance to photobleaching[13]. These properties are advantageous for potential novel imaging and biological applications the levels of biocompatibility and toxicity needed to interact with cells and the body often limit other materials. Carbon-based nanodots are seen to exhibit the elements of carbon (sp^2 hybridized cores) and oxygen components in the forms of carboxyl, hydroxyl, and aldehyde groups. Carbon and quantum dots possess unique qualities that exploited for imaging platforms by attaching various molecules to the surface. However, a significant limitation of quantum dots is that the components in the core, which include heavy metals such as cadmium and selenium, are chronically toxic to cells and organisms[14]. The toxicity of quantum dots makes them less desirable for use with targeting agents. There are different methods to form synthetic nanodots through chemical or physical techniques to produce nanodots[13]. Some methods provide ways to create a nanodot platform with a higher order of carbon bonding that are convenient and straightforward while avoiding the use of toxic materials or highly specialized equipment. The hydrothermal synthesis technique was utilized to create citric and malic acid-based nanodots with

activatable carboxylic groups on the surface. This chemical method of carbon nanodots synthesis has been explored for carboxylic group surface activation to achieve moiety attachment[15-17]. This synthesis method is a series of condensation reactions resulting in different carbon interactions in the nanodot core. As used by Loo et al.[17], this method can create a nanodot platform for carboxylic group activation.

Evaluating surface modified-based nanodot system can give rise to higher targeting affinity to cancer cells due to upregulated receptors[18]. Creating a nanodot platform encompassing surface ligands increases the receptor-mediated uptake due to the presence of specific receptors at the cell surface. Nanodot platforms anchored with fluorescent probes have become increasingly popular for imaging applications as they allow specific cells/areas to be visualized. Anchoring targeting probes to the surface eliminates the need for encapsulation. Encapsulation of fluorescent dyes can result in leaching out of the delivery vehicle and may cause harm to the cell surroundings[19]. Linking fluorescent probes to the surface allows the probe to function once it reaches the target site while also eliminating the risk of it leaking preemptively. These anchored fluorescent probes can potentially label cancer cells more effectively and more efficiently than existing probes used in bioimaging applications.

Because they enhance the internalization of nanomaterials, surface receptors are ideal targets for cancer imaging. Many receptors are upregulated on cancer cell surfaces, including the human epidermal growth factor receptor 2 (HER2), folate receptor, transferrin receptor, and translocator protein receptor[20]. Utilizing one or more of these target receptors will increase the internalization of the nanodot platform. This surface ligand nanodot platform allows the specific target receptors to be used. The nanodot platform will enhance cancer cells' targeting and uptake by exploiting the upregulated cell receptors. Targeting over-expressed receptors on cancer tumor cells can provide improved uptake of bioimaging or therapeutic agents to enhance the visualization of tumors or improve treatment regimens. The surface of the citric and malic acid-

based nanodots can be modified by attaching a NIR fluorescent dye and a protective coating of polyethylene glycol (PEG) for further evaluation for use in cancer bioimaging applications.

This work developed an unlabeled, bare carbon nanodot platform for potential use in bioimaging applications. Bare carbon nanodots were produced from the hydrothermal synthesis method utilizing citric and malic acid precursors, which provided a steppingstone for the silica nanoparticle platform. The citric and malic acid nanodots (**Figure 22**) were found to be around 23.3 ± 8.1 nm (citric) and 18.0 ± 2.6 nm (malic) via Atomic Force Microscopy (AFM). This nanodot platform can be used to attach near-infrared NIR dye molecules through NHS/EDC chemistry and surface modifications with biomolecules to target cancer cells. AFM (**Figure 22**) and X-ray Photoelectron Spectroscopy (XPS) (**Figure 23**) characterization methods were evaluated on bare carbon nanodots. XPS characterization is utilized to examine the elemental composition of the nanomaterials' surface, which can provide crucial information on the surface of our newly made nanodots. Through XPS, we can discover the elemental composition of nanotechnologies. The characterization techniques help determine the necessary size, spectroscopy, and elemental composition parameters of the newly synthesized nanodots. Although only bare nanodots were produced and characterized, there is the potential for this carbon nanodot platform to be explored deeper. However, the silica nanoparticle platform provided a more rigid structure for dye and biomolecule attachment.

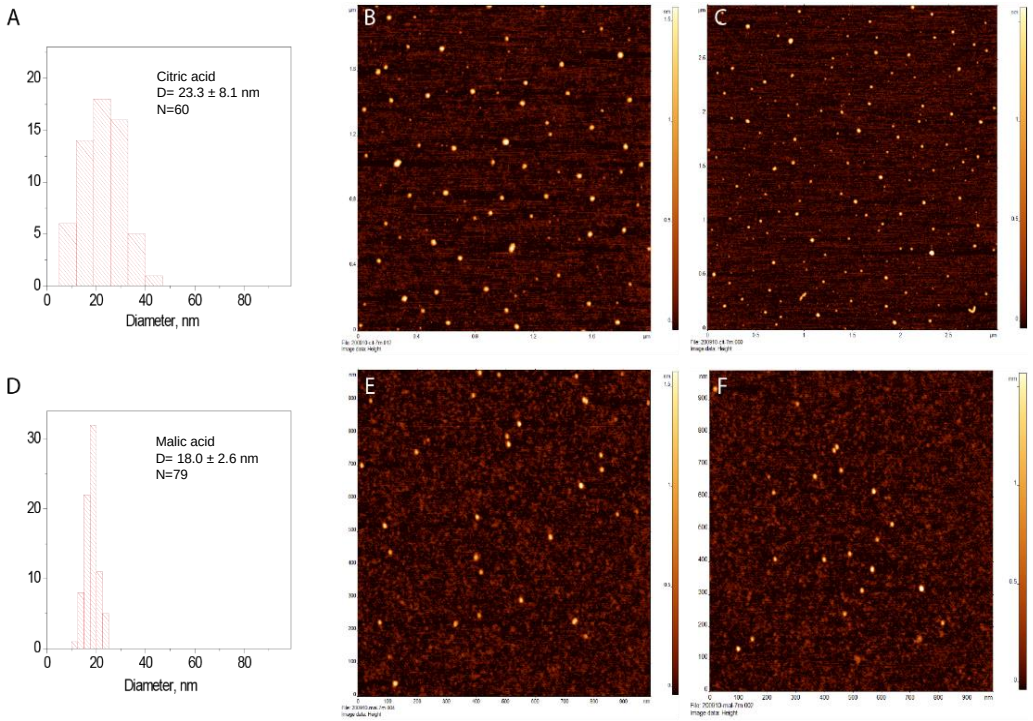

Figure 22. Atomic Force Microscopy (AFM) size determination of bare citric and malic acid-based nanodot system. (A-C) represent size determination of the citric acid-based nanodots and were around 23.3 ± 8.1 nm. (D-F) represent size determination of the malic-based nanodots and were found to be 18.0 ± 2.6 nm.

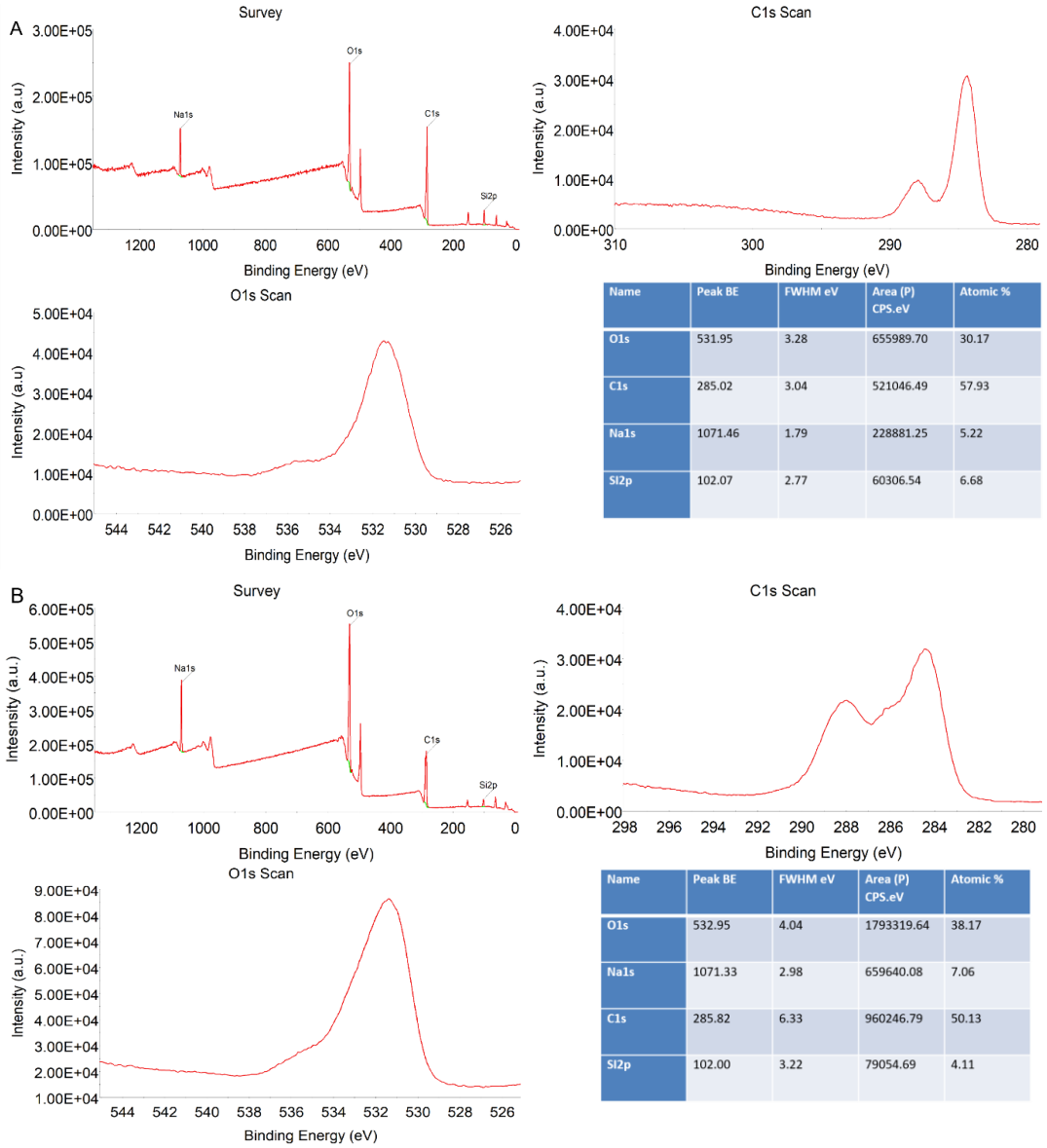

Name	Peak BE	FWHM eV	Area (P) CPS.eV	Atomic %
O1s	531.95	3.28	655989.70	30.17
C1s	285.02	3.04	521046.49	57.93
Na1s	1071.46	1.79	228881.25	5.22
Si2p	102.07	2.77	60306.54	6.68

Name	Peak BE	FWHM eV	Area (P) CPS.eV	Atomic %
O1s	532.95	4.04	1793319.64	38.17
Na1s	1071.33	2.98	659640.08	7.06
C1s	285.82	6.33	960246.79	50.13
Si2p	102.00	3.22	79054.69	4.11

Figure 23. X-ray Photoelectron Spectroscopy surface elemental composition determined of the citric and malic acid nanodots. (A) Citric Acid and (B) Malic Acid-based nanodots.

Lymphatic targeting

Aside from affinity to CD44 receptors, hyaluronic acid is observed to have strong interaction and relationship with LYVE1 cell receptors found in lymphatic endothelial tissue. LYVE1 is a close relative to the CD44 receptor and is widely used as a marker to delineate blood and lymphatic vessels[21]. The

interaction between hyaluronic acid and LYVE1 can be evaluated in similar parameters as the hyaluronic acid-CD44 interaction. The lymphatic system includes any tissue types that encompass the lymph nodes. An active role of the lymphatic system is the function it plays in cancer metastasis[22]. Cancer tumors that have metastasized can be targeted, tracked, found, and removed by fluorescently labeling the lymphatic tissue. With the knowledge of HA affinity to the lymphatic system through the LYVE1 receptors, a hyaluronic acid-based system can be designed to evaluate the affinity with the LYVE1 receptors. In previous work, another NIR dye (a BIODIPY derivative, BDP TMR) was conjugated with hyaluronic acid to assess the natural targeting potential of HA to the LYVE1 receptors for the imaging of lymphatic endothelial tissue. Collaborators from South Dakota State University (Dr. Darci Fink laboratory) helped evaluate the preliminary result of the HA targeting on various lymphatic endothelial cell lines (SVLEC and hLEC cells). This initial work was observed to show the preferential binding of the HA-dye conjugate to the surface of the cells in an imaging application. This work provides evidence that hyaluronic acid can target lymphatic endothelial cells, providing an avenue to target the lymphatic system with a hyaluronic acid-based platform. There is potential for modifying the architecture of the nanotechnology system by utilizing hyaluronic acid to modify the surface of carbon nanodots or silica nanoparticles for the potential of fluorescently labeling the lymphatic tissue for cancer imaging applications.

Bibliography

1. Troyan, S. L.; Kianzad, V.; Gibbs-Strauss, S. L., et al., The Flare™ Intraoperative near-Infrared Fluorescence Imaging System: A First-in-Human Clinical Trial in Breast Cancer Sentinel Lymph Node Mapping. *Ann. Surg. Oncol.* **2009**, *16* (10), 2943-2952.

2. Bonner, W.; Hulett, H.; Sweet, R., et al., Fluorescence Activated Cell Sorting. *Rev. Sci. Instrum.* **1972**, *43* (3), 404-409.

3. Yu, M.; Jambhrunkar, S.; Thorn, P., et al., Hyaluronic Acid Modified Mesoporous Silica Nanoparticles for Targeted Drug Delivery to Cd44-Overexpressing Cancer Cells. *Nanoscale.* **2013**, *5* (1), 178-183.

4. De la Fuente, M.; Seijo, B.; Alonso, M. J., Novel Hyaluronic Acid-Chitosan Nanoparticles for Ocular Gene Therapy. *Invest. Ophthalmol. Vis. Sci.* **2008**, *49* (5), 2016-2024.

5. Yang, H.; Lou, C.; Xu, M., et al., Investigation of Folate-Conjugated Fluorescent Silica Nanoparticles for Targeting Delivery to Folate Receptor-Positive Tumors and Their Internalization Mechanism. *Int. J. Nanomedicine.* **2011**, *6*, 2023.

6. Dutta, D.; Donaldson, J. G., Search for Inhibitors of Endocytosis: Intended Specificity and Unintended Consequences. *Cellular Logistics.* **2012**, *2* (4), 203-208.

7. Chen, C.-L.; Hou, W.-H.; Liu, I.-H., et al., Inhibitors of Clathrin-Dependent Endocytosis Enhance Tgfβ Signaling and Responses. *J. Cell Sci.* **2009**, *122* (11), 1863-1871.

8. Ivanov, A. I., Pharmacological Inhibition of Endocytic Pathways: Is It Specific Enough to Be Useful? *Exocytosis and Endocytosis.* **2008**, 15-33.

9. Rejman, J.; Bragonzi, A.; Conese, M., Role of Clathrin-and Caveolae-Mediated Endocytosis in Gene Transfer Mediated by Lipo-and Polyplexes. *Mol. Ther.* **2005**, *12* (3), 468-474.

10. Cho, K.; Wang, X.; Nie, S., et al., Therapeutic Nanoparticles for Drug Delivery in Cancer. *Clin. Cancer Res.* **2008**, *14* (5), 1310-1316.

11. Wilczewska, A. Z.; Niemirowicz, K.; Markiewicz, K. H., et al., Nanoparticles as Drug Delivery Systems. *Pharmacol. Rep.* **2012**, *64* (5), 1020-1037.

12. Liu, H.; Li, Z.; Sun, Y., et al., Synthesis of Luminescent Carbon Dots with Ultrahigh Quantum Yield and Inherent Folate Receptor-Positive Cancer Cell Targetability. *Sci. Rep.* **2018**, *8* (1), 1-8.

13. Li, H.; Kang, Z.; Liu, Y., et al., Carbon Nanodots: Synthesis, Properties and Applications. *J. Mater. Chem.* **2012**, *22* (46), 24230-24253.

14. Bottrill, M.; Green, M., Some Aspects of Quantum Dot Toxicity. *Chem. Commun.* **2011**, *47* (25), 7039-7050.

15. Qian, Z.; Chai, L.; Zhou, Q., et al., Reversible Fluorescent Nanoswitch Based on Carbon Quantum Dots Nanoassembly for Real-Time Acid Phosphatase Activity Monitoring. *Anal. Chem.* **2015**, *87* (14), 7332-7339.

16. Qian, Z.; Chai, L.; Tang, C., et al., Carbon Quantum Dots-Based Recyclable Real-Time Fluorescence Assay for Alkaline Phosphatase with Adenosine Triphosphate as Substrate. *Anal. Chem.* **2015**, *87* (5), 2966-2973.

17. Loo, A. H.; Sofer, Z.; Bouša, D., et al., Carboxylic Carbon Quantum Dots as a Fluorescent Sensing Platform for DNA Detection. *ACS Appl. Mater.* **2016**, *8* (3), 1951-1957.

18. Liu, Y.; Sun, J.; Cao, W., et al., Dual Targeting Folate-Conjugated Hyaluronic Acid Polymeric Micelles for Paclitaxel Delivery. *Int. J. Pharm.* **2011**, *421* (1), 160-169.

19. Chen, Y.; Wu, Y.; Sun, B., et al., Two-Dimensional Nanomaterials for Cancer Nanotheranostics. *Small.* **2017**, *13* (10), 1603446.

20. Yi, X.; Wang, F.; Qin, W., et al., Near-Infrared Fluorescent Probes in Cancer Imaging and Therapy: An Emerging Field. *Int. J. Nanomedicine.* **2014**, *9*, 1347.

21. Jackson, D. G., Hyaluronan in the Lymphatics: The Key Role of the Hyaluronan Receptor Lyve-1 in Leucocyte Trafficking. *Matrix Biol.* **2019**, *78*, 219-235.

22. Singh, I.; Swami, R.; Khan, W., et al., Delivery Systems for Lymphatic Targeting. In *Focal Controlled Drug Delivery*, Springer: **2014**; pp 429-458.